Nonlinear dynamics of wake vortices

Holly Johnson

NNT : 2016SACLX101

Thèse de doctorat
de l'Université Paris-Saclay
préparée à l'Ecole Polytechnique

Ecole doctorale n°579
Sciences Mécaniques et Energétiques, Matériaux et Géosciences
Spécialité de doctorat : Mécanique des Fluides

par

Mme Holly Johnson

Nonlinear dynamics of wake vortices

Thèse présentée et soutenue à Meudon, le 7 décembre 2016.

Composition du Jury :

M.	Jean-Christophe Robinet	Professeur, ENSAM	(Président du jury)
M.	Peter Schmid	Professeur, Imperial College London	(Rapporteur)
M.	Pierre Brancher	Professeur, Université Toulouse III	(Rapporteur)
Mme	Sabine Ortiz	Professeur, ENSTA	(Examinatrice)
M.	Frank Holzäpfel	Ingénieur de recherche, DLR	(Examinateur)
M.	Ivan Delbende	Maître de conférences, UPMC	(Examinateur)
M.	Vincent Brion	Ingénieur de recherche, ONERA	(Encadrant de thèse)
M.	Laurent Jacquin	Professeur, Ecole Polytechnique	(Directeur de thèse)

ÉCOLE DOCTORALE
Sciences mécaniques et énergétiques, matériaux et géosciences (SMEMAG)

Titre : La dynamique non-linéaire des tourbillons de sillage

Mots clés : Tourbillon de sillage, Instabilité de Crow, Dynamique non-linéaire, Perturbation optimale

Résumé : Les tourbillons de sillage d'avion posent des problèmes économiques, environnementaux et de sécurité. Le sillage est composé d'une paire de tourbillons contrarotatifs qui perdurent longtemps après le passage de l'avion. Dans cette thèse la dynamique non-linéaire de ces tourbillons est examinée par Simulation Numérique Directe (DNS). L'objectif est d'étudier les comportements non-linéaires des tourbillons de sillage et d'évaluer le potentiel de destruction anticipée des tourbillons par la perturbation optimale. Dans un premier temps, la capacité destructrice de la perturbation optimale linéaire d'une paire de tourbillons est estimée en appliquant la perturbation aux tourbillons avec une amplitude initiale croissante et en observant la réponse non-linéaire de l'écoulement. Une amplitude raisonnable suffit pour que la perturbation optimale linéaire réduise de moitié la durée de vie des tourbillons en accélérant le développement de l'instabilité de Crow et en engendrant une perte de cohérence des structures après la reconnexion. Par la suite, un outil d'optimisation non-linéaire est développé et validé par la reproduction de résultats existants. Il est montré que la perturbation optimale non-linéaire d'un tourbillon isolé 2D peut générer une croissance transitoire bien plus élevée que la perturbation optimale linéaire. Dans certains cas la perturbation optimale non-linéaire provoque une transition vers un état non-axisymétrique quasi-stationnaire, évitant ainsi le processus d'axisymétrisation. Il est montré que la distribution de vorticité dans le cœur du tourbillon peut influencer de manière significative les perturbations optimales. Enfin, l'analyse d'optimisation non-linéaire est étendue aux perturbations 3D. Bien que les perturbations optimales non-linéaires 3D produisent moins d'amplification que les perturbations optimales linéaires, des transitions vers des états énergétiques et persistants sont observées.

Title: Nonlinear dynamics of wake vortices

Keywords: Wake vortices, Crow instability, Nonlinear dynamics, Optimal perturbation

Abstract: Aircraft wakes have been the subject of extensive research for several decades as it poses economic, safety and environmental issues. The wake is composed of powerful counter-rotating vortices that persist long after the aircraft has passed. In this thesis, the nonlinear dynamics of aircraft wake vortices is investigated through Direct Numerical Simulation. The aim is to explore the nonlinear effects on wake vortex behaviour and evaluate the potential for the anticipated destruction of the vortices through optimal perturbation. First the disruptive potential of the linear optimal perturbation of the flow is evaluated by applying it with increasing initial amplitude and observing the nonlinear response of the flow. With sufficient yet reasonable initial amplitude, the linear optimal perturbation halves the life-span of the vortex pair by accelerating the loss of coherence of the vortices after the linking phase. Next the nonlinear gradient-based optimisation tool that was developed during the thesis is validated by reproducing existing results concerning a simple vortical flow: an isolated two-dimensional vortex. In doing so new nonlinear optimisation results are obtained and analysed. In particular, it is shown that the 2D nonlinear optimal perturbation of an isolated vortex can induce considerably greater transient growth than the linear optimal. In some cases, the nonlinear optimal causes a transition to a quasi-steady asymmetric state, bypassing the natural axisymmetrisation process. The effect of the vortex vorticity profile on the optimal perturbations is also studied. Vortices with sharper profiles experience far greater linear perturbation growth, however the nonlinear growth is significantly inferior. Finally, the nonlinear optimal perturbation analysis of the isolated vortex is extended to three dimensions. Although the 3D nonlinear optimals produce less growth than their linear counterparts, they can lead to quasi-permanent high energy states.

Université Paris-Saclay
Espace Technologique / Immeuble Discovery
Route de l'Orme aux Merisiers RD 128 / 91190 Saint-Aubin, France

Contents

Introduction

Vortices constitute an elementary building block of all fluid flows and can be found on all scales of natural fluid motion. Küchemann [54] pertinently described these structures as 'the sinews and muscles of fluid motion'. A classic example of a vortex on the astrophysical scale is the Great Red Spot visible on the surface of the planet Jupiter. This persistent storm is large enough to contain two or three planets the size of earth. The next scale down is the geophysical scale which corresponds to meteorological occurrences such as tornadoes and hurricanes. In fully developed turbulence, vortex scales range from macroscopic to microscopic, composing the Kolmogorov cascade of energy which is transferred from large structures to smaller ones until dissipated by viscosity at the microscopic scale. Turbulent flow is one of the most complex concepts to confront man yet some fortunate beings appear to have had flashes of insight into the phenomenon. In the 19th century, the Dutch artist Van Gogh captured the essence of turbulence in many of his paintings, such as 'The Starry Night' shown in figure 1. In a recent scientific study of impressionist art, by digitising the artwork it has been proved that the patterns in some of Van Gogh's work are astoundingly close to Kolmogorov's equations. This resemblance has not been in found in any other impressionist's work. Interestingly the accurate depiction of turbulence only appears in the work Van Gogh accomplished during psychotic episodes of his life. Although many models interpreting turbulence exist, the complete comprehension of turbulent flows remains an open question.

Figure 1: 'The Starry Night' by Van Gogh, June 1889.

Vortices are also omnipresent in man-made flows. The tip-leakage vortex in turbomachines is created at the tip of each rotating blade and can cause significant losses in the turbomachine efficiency. The low pressure region within the vortex core also promotes cavitation for machines running in water streams which causes damage to the blades. For these reasons the tip-leakage vortex is seen as an inconvenience and work is being pursued to minimise the effect of its presence. Conversely the efficiency of combustion engines relies on effective mixing of the fuel with the oxidiser (usually air). Vorticity in the combustion chamber promotes mixing and is therefore desirable.

The man-made vortex flow targeted predominantly in this thesis is the aircraft wake.

The aircraft vortex wake

Aeroplanes remain airborne as a result of lift. This force is generated by a pressure difference between the upper and lower surfaces of the aerofoil. The pressure difference pulls the fluid up from under the wing and around the wing tip, creating a rotating motion (see figure 2 for a visualisation of this effect). Further downstream of the aircraft, the wake rolls up completely to form two powerful counter-rotating vortices. A schematic and a real life image of the wake are given in figures 3(a) and (b) respectively. In figure 3(b) the circulation of the air is visible thanks to clouds.

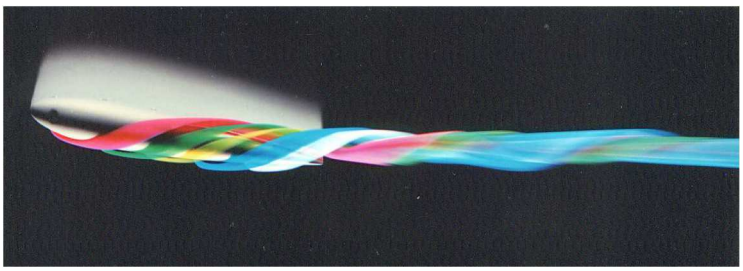

Figure 2: Formation of the wake vortices: side view of a wing-tip vortex visualised using dye, from Werlé [96].

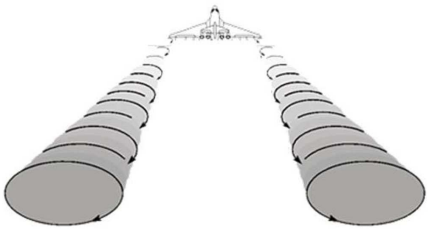

(a) Schematic of the vortex wake

(b) Real vortex wake

Figure 3: Illustrations of the aircraft vortex wake

The safety problem

The strength or circulation Γ of the vortices is directly related to the lift and therefore to the weight of the aircraft. The larger the aircraft, the more powerful the wake. Moreover, experimental evidence suggests that wake vortices are usually very persistant [92], and that although the vorticity is eventually rearranged, it will continue to exist in another form [91].

Spalart [92] concluded that most aircraft would be unable to counter the roll generated by the wake left by a preceding aircraft. For example, were a light aircraft to encounter the wake of a heavy aircraft, the rotational force induced by the vortices would cause extreme turbulence and could cause loss of control. This poses a particular problem in airports, where planes take-off and land frequently on a limited number of runways. In 1970 with the apparition of the B747, the world's first 'Jumbo Jet', the Federal Aviation Administration and the International Civil Aviation Organisation established guidelines classifying aircraft into three categories (light, medium and heavy), see figure 4 for further details. Two further categories are defined for the largest aeroplanes in use: the A380 and the B747. Within these guidelines, separation distances were imposed between the take-off and landing of aircraft of each category

in order to ensure that the vortices of the previous craft were sufficiently dispersed and no longer posed a danger. For example, were a 'Large' aircraft to land after an A380, the standard separation distance according to the FAA would be 8 nmi (nautical miles), that is approximately 14.8 km. Assuming an average landing speed of 70 m/s, the time between the first and second planes approaching the runway would have to be approximately 3.5 minutes to comply with regulations.

Generating aircraft	**Separation distance for trailing aircraft, nmi**		
	Small	Large	Heavy
Small	2.5	2.5	2.5
Large	4	2.5	2.5
Heavy	6	5	4
B747	5	4	4
A380	10	8	6

Figure 4: Current FAA standards for aircraft separation under Instrument Flight Rules (IFR) conditions (in nautical miles).

In recent years, with the ever-increasing demand for civil air transport, airports such as London Heathrow and Paris Charles De Gaulle have experienced increased congestion problems at peak hours. These airports no longer have the capacity to provide the required number of flights whilst complying with the safety interval guidelines. One answer to the problem would be to build more runways, but a less controversial solution would be to verify and amend the ICAO classification in order to reduce the intervals to more realistic values while maintaining safe flight conditions.

In order to refine the classification, several approaches are possible. The first would be to study the dynamics of vortices through experimental and numerical methods for better understanding and prediction of the wake's behaviour. The second approach would be to take this further by developing control methods based on the knowledge gleaned from observation and analysis. This could allow acceleration of the vortex breakdown thus reducing the necessary time intervals.

The environmental problem

Beside the safety issue, another motivation for the study of aircraft wakes has arisen: their effect on the environment. In certain temperature and humidity conditions, chemicals from the exhaust of aircraft engines can become trapped within the vortex core and form ice crystals which compose the white contrails often visible behind aeroplanes. If the conditions are right, the longevity of the vortices can lead to the eventual formation of artificial clouds. Figure 5(a) shows an example of contrail formation behind an aircraft and figure 5(b) an image of artificial cirrus clouds due to aircraft contrails. The presence of these additional clouds in the atmosphere modify the Earth's radiative balance contributing to global warming.

Objectives and organisation of the thesis

An efficient solution to the vortex wake problem would be to determine the 'optimal' perturbation, that is the perturbation that would destroy the vortices most effectively. Farrell [36] first defined the term optimal perturbation in his study of the Poiseuille flow as the disturbance that would induce the greatest perturbation growth over a given period of time. Several studies [2, 3, 80] describe the optimal perturbations of an isolated vortex whilst considering the linearised Navier-Stokes equations (assuming

(a) Formation of aircraft contrails

(b) Artificial cirrus clouds

Figure 5: Illustration of the environmental problem posed by wake vortices

very small perturbation amplitudes). Subsequently Brion et al. [15] addressed the counter-rotating vortex pair configuration, determining the linear optimal perturbation of the Crow instability, the dominant instability affecting vortex pairs in atmospheric conditions.

Optimal perturbation studies using the complete nonlinear Navier-Stokes equations have also been performed, mainly on shear flows, and show promising results [81, 19, 35]. Nonlinear optimal perturbations can generate significantly higher perturbation growth and tend to be more spatially localised. This leads to the belief that the nonlinear optimals are more relevant to the flow. Bisanti [13] recently studied the nonlinear optimal perturbation of a two-dimensional isolated vortex and showed that nonlinear optimals also show potential in rotating flows. These results and others will be detailed and commented on in a review of existing work in Chapter 1.

The objective of this thesis is to determine the nonlinear optimal perturbation of the aircraft vortex wake. Although this final goal is yet to be achieved in its entirety, several successful steps are taken towards accomplishing this aim. Firstly the effect of the linear optimal perturbation of a vortex pair, previously determined by Brion et al. [15], and its potential to accelerate vortex decay is evaluated (Chap. 3). In the course of this analysis the amplitude of the disturbance needed to effectively accelerate the vortex decay is estimated. Secondly, a gradient-based nonlinear optimisation tool is developed and validated by comparing results with existing work. Finally this tool is applied to vortical flows, starting with simplified flows such as isolated vortices, and the resulting optimal perturbations will be compared with the linear optimals described in other work [2, 3, 80] (Chap. 4).

The thesis is organised as follows. First, a review of previous work on the stability of isolated vortices and vortex pairs is established, followed by existing results of optimal perturbation studies (Chap. 1). Secondly, the numerical methods used throughout the thesis are detailed, justified and validated (Chap. 2). Then a study of the nonlinear dynamics of a pair of counter-rotating vortices subjected to the Crow instability is carried out in Chapter 3. The nonlinear optimisation method is applied to a simple flow: a two-dimensional isolated vortex in Chapter 4. The study is subsequently extended to a three-dimensional vortex (Chap. 5). An analysis of the effect of the vortex structure is given in Chapter 6. Finally, in the conclusion, the main results of the thesis are outlined with an outlook for the future of this project.

Chapter 1

Review of vortex stability

This chapter presents a review of recent work concerning vortex dynamics and stability. Despite having been studied for many decades, several aspects of vortex dynamics remain partially or completely unexplained. An example of this is the meandering phenomenon. The chapter is organised as follows. First the most common vortex models used in analytical and numerical studies to replicate real flows are described (§ 1.1). Then the main instabilities affecting vortices, whether isolated or in pairs, are reviewed (§ 1.2). Three important topics concerning vortices are detailed: the axisymmetrisation process (§ 1.3), vortex meandering (§ 1.4) and the interaction of vortices with external turbulence (§ 1.5). The merits of non-normal stability analysis are briefly presented in § 1.6. Finally recent developments in other methods such as optimal perturbation are discussed in § 1.7.

1.1 Vortex models

Models are designed to reproduce real flows observed in experiments for use in theoretical and numerical studies. The most typical vortex models are described briefly in the following paragraphs.

1.1.1 Rankine vortex

The most basic representation of a vortex is a cylinder of solid-body rotation also known as a Rankine vortex. The core is surrounded by an inviscid potential flow. The azimuthal velocity of a Rankine vortex is expressed:

$$V = \begin{cases} \Gamma r / \left(2\pi a^2\right) & r \leq a \\ \Gamma / \left(2\pi r\right) & r > a \end{cases} \tag{1.1}$$

with Γ the vortex circulation and a the dispersion radius.

1.1.2 Lamb-Oseen vortex

The Lamb-Oseen (LO) vortex has a Gaussian vorticity distribution and is representative of most vortices in real flows. In particular, two-dimensional turbulence and three-dimensional experimental vortices have successfully been compared with the LO vortex [28, 59]. The azimuthal velocity of the LO vortex is given as:

$$V = \frac{\Gamma}{2\pi r}\left(1 - e^{-r^2/a^2}\right) \tag{1.2}$$

The Lamb-Oseen model is used throughout this thesis unless clearly stated otherwise.

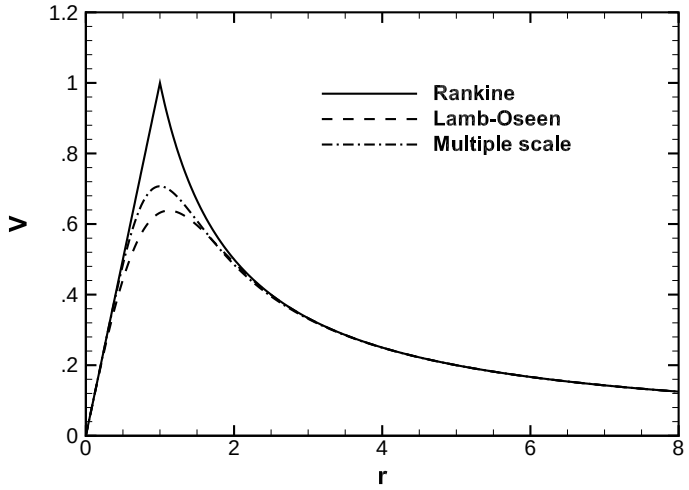

Figure 1.1: Azimuthal velocity profiles of the Rankine, Lamb-Oseen and multiple-scale vortices, with $a = 1$, $\Gamma = 2\pi$, $a_1 = 1$, $a_2 = 10$, and $\alpha = 1$.

1.1.3 Batchelor vortex

The Batchelor vortex [10] is a three-dimensional flow composed of a Gaussian vortex and an axial flow. This model was designed to replicate wake vortices in the far-field which often display an axial velocity component generated during the roll-up phase. The velocity of the Batchelor vortex is:

$$V = \frac{\Gamma}{2\pi r}\left(1 - e^{-r^2/a^2}\right) \tag{1.3}$$

$$W = W_\infty + \Delta W e^{-r^2/a^2} \tag{1.4}$$

W_∞ is the flow velocity in the far-field and $\Delta W = W(r = 0) - W_\infty$. The model is also known as the 'q-vortex' after the swirl parameter $q = \Gamma/(2\pi a \Delta W)$ which denotes the ratio between the azimuthal and axial velocity components. A LO vortex is retrieved in the $q \longrightarrow \infty$ limit.

1.1.4 Multiple-scale models

Fabre & Jacquin [32] show that far-field aircraft wake vortices are in fact closer fitted to multiple-scale vortices. Their experimental data lead to the definition of a multiple-scale model:

$$V = \begin{cases} \frac{\Gamma r}{2\pi a_1^{1+\alpha} a_2^{1-\alpha}} & r \leq a_1 \\ \frac{\Gamma}{2\pi a_2^{1-\alpha} r^\alpha} & a_1 < r < a_2 \\ \frac{\Gamma}{2\pi r} & r \geq a_2 \end{cases} \tag{1.5}$$

The vortex is characterised by two radii a_1 and a_2 and a parameter α defining the intermediate region.

1.2 Vortex stability

A flow is termed stable if, when disturbed by a small perturbation, it eventually returns to its original undisturbed state. When this is not the case the flow is unstable. Assuming the perturbations to a flow are small (of amplitude $\epsilon << 1$ compared to the base flow), the flow equations can be linearised around the base flow. In this context, the equations governing the flow are the incompressible Navier-Stokes

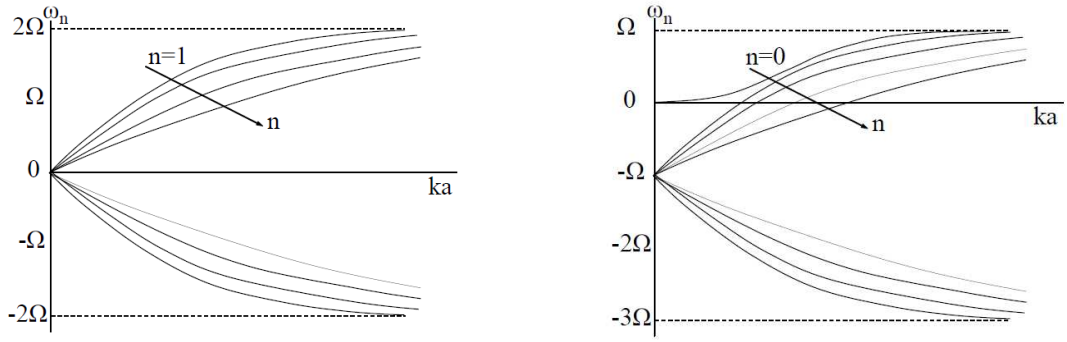

Figure 1.2: Oscillation frequencies of the $m = 0$ and $m = 1$ Kelvin waves of a Rankine vortex as a function of the axial wavenumber ka, from Saffman [85].

equations.

From the linearised Navier-Stokes equations, the linear stability properties of the flow can be determined (see Drazin & Reid [27]). The small perturbations applied to the base flow are decomposed into a set of normal modes with exponential time dependence. Linearising the Navier-Stokes equations around the base flow then produces an eigenvalue problem. The solutions to the problem are of the form $u'(x,t) = \hat{u}\exp(i\sigma t)$ with $\sigma = \sigma_R + i\sigma_I$ the complex frequency. The real part σ_R is the mode frequency and $-\sigma_I$ gives its growth rate. If $\sigma_I < 0$ then the flow is unstable, that is the perturbation will amplify exponentially, otherwise the flow is stable and the perturbations are damped. In the following paragraphs we describe some of the most common instabilities affecting vortices.

1.2.1 Kelvin waves

In 1880 Lord Kelvin [52] demonstrated the existence of waves propagating along a vortex core when the vortex is disturbed by a small perturbation. The disturbance unsettles the natural equilibrium between the pressure and the azimuthal velocity creating an axial pressure gradient within the core and ensuring the propagation of the perturbation. The waves can be categorised by their azimuthal wavenumber m. The modes are classed as 'cograde', that is rotating in the same direction and faster than the vortex, 'retrograde', that is rotating in the same direction but slower than the vortex or 'countergrade', rotating in the opposite direction. Kelvin waves are stable or neutrally stable so the vortex eventually returns to its original unperturbed state. Saffman [85] determined the complete spectrum of Kelvin waves of a Rankine vortex. The oscillation frequencies of the $m = 0$ 'sausaging' modes and $m = 1$ 'bending' modes of a Rankine vortex of radius a and rotation frequency Ω are given in figure 1.2.

Kelvin waves have been observed experimentally by Hopfinger et al. [44] and Maxworthy et al. [69] in a rotating water tank, and numerically by Arendt et al. [5] by solving the initial value problem of a Rankine vortex. Fabre et al. [34] determined the complete set of normal modes of a LO vortex using normal mode analysis. In addition to Kelvin waves, the LO vortex presents highly-damped singular viscous modes which also are all stable. The LO vortex is therefore linearly stable to small perturbations.

1.2.2 Shear instability

A shear flow becomes unstable when an inflexion point develops in the velocity profile (see Rayleigh's inflexion point theorem [61]) and generates a series of vortices. In the case of parallel shear flows the instability that appears is known as the Kelvin-Helmholtz instability. Examples of flows in which this

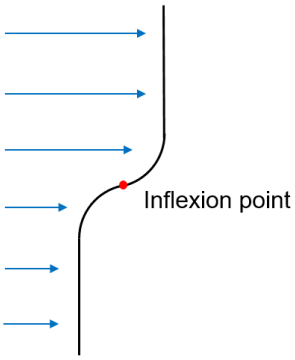

(a) Schematic of an inflexion point in a parallel velocity profile.

(b) Kelvin-Helmholtz instability in an axisymmetric jet.

Figure 1.3: Illustration of the shear instability.

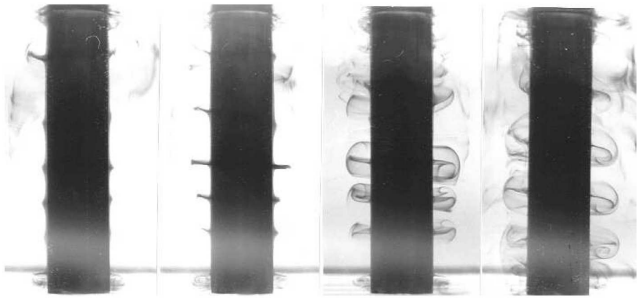

Figure 1.4: Dye visualisation of the Taylor-Couette instability affecting the flow between two coaxial cylinders.

instability occurs include jets and mixing layers, where flows of differing but parallel velocity meet. Illustrations of an inflexion point in the velocity profile and a Kelvin-Helmholtz instability developed in an axisymmetric jet are provided in figure 1.3. Gallaire & Chomaz [41] demonstrated that the necessary condition for an azimuthal shear instability to develop in a 2D axisymmetric flow is $d\omega/dr = 0$, that is a local radial extremum of axial vorticity.

1.2.3 Centrifugal instability

The centrifugal instability corresponds to a loss of balance between the centrifugal forces due to the rotation of the fluid in the vortex and the radial pressure gradient, which otherwise prevails in a steady axisymmetric flow with no radial component.

$$\frac{V^2}{r} = -\frac{dp}{dr} \tag{1.6}$$

This instability occurs if the angular momentum does not increase monotonically with increasing r, and was first described by Rayleigh [61]. Regions of high angular momentum are propelled away from the core whereas regions of low momentum move closer to the core. This results in the creation of rolls of azimuthal vorticity. An example is given in figure 1.4: the Taylor-Couette instability that occurs in the flow between two coaxial cylinders, the internal cylinder rotating while the external one is stationary. Jacquin & Pantano [48] showed that this instability occurs in trailing vortices where axial velocity carries angular momentum and creates a circulation overshoot.

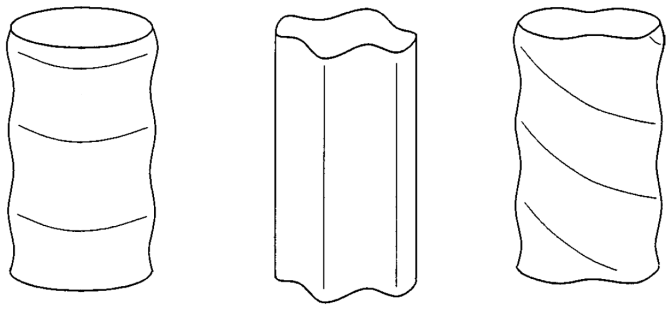

Figure 1.5: Illustration of instabilities affecting vortices, from left to right: centrifugal, shear and helical. From Gallaire & Chomaz [41].

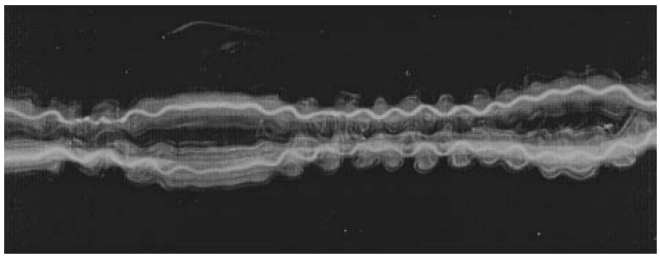

Figure 1.6: Visualisation of a counter-rotating vortex pair affected simultaneously by the Crow and Widnall instabilities using dye, from Leweke & Williamson [59].

Both the centrifugal and shear instabilities can affect a vortex at the same time giving rise to a helical instability as described by Gallaire & Chomaz [41] (see figure 4(a) of their paper which combines shear and centrifugal instability mechanisms). An illustration of the centrifugal, shear and helical instabilities affecting a vortex is given in figure 1.5.

1.2.4 Stability of vortex pairs

So far all the instabilities described concern isolated vortices. However in many configurations such as an aircraft wake, more than one vortex is present and their interaction can induce 'cooperative instabilities'. Jimenez [49] demonstrated that a pair of co-rotating vortices is stable. On the contrary the counter-rotating pair is susceptible to cooperative instabilities. The affected vortices undergo sinusoidal deformations at two different wavelengths, as can be observed in the experiments of Leweke & Williamson [59] in figure 1.6: one scaled on the vortex core radius a, and one scaled on the distance separating the vortices b. The deformation induced by cooperative instabilities is a product of the superposition of two effects: a rotating displacement mode within the vortex core and the strain field induced by the other vortex. The displacement mode induces a deformation of the vortex which is amplified (resp. diminished) in the stretching (resp. compression) directions of the strain field. This mechanism is illustrated in figure 1.7.

The long wavelength instability was first characterised by Crow [21] using classic stability theory on a pair of vortex filaments. The so-called Crow instability has an axial wavelength of around $8b$, with b the distance separating the vortex centroids, and induces a symmetric sinusoidal deformation of the vortices in a 45^o plane with respect to the plane containing the undeformed cores (see figure 1.8(a)). This instability can be observed in aircraft wake vortices as shown in figure 1.8(b). When the vortices are deformed sufficiently for the closest parts to touch, the vortices undergo a transformation called linking in which the vortices break off to form rings. This phenomenon is described well by Melander

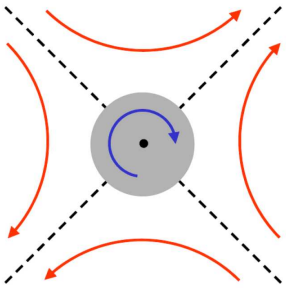

Figure 1.7: Illustration of the combined effects of a rotating displacement mode (shown in blue) and the strain induced by one vortex on the other (shown in red). The grey patch represents the core of one of the two vortices.

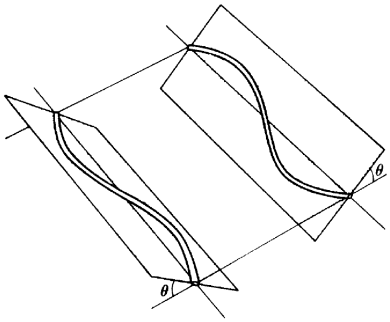

(a) Schematic of the Crow instability, from Crow [21].

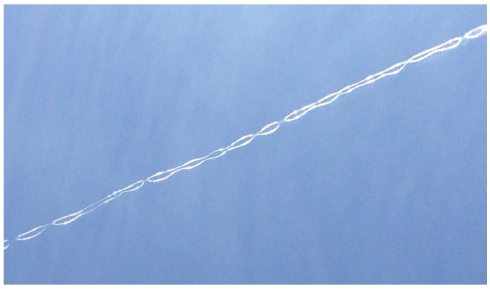

(b) Crow instability observed in a real aircraft wake. The vortices are visible due to the presence of condensed water from the exhaust within the core.

Figure 1.8: Illustrations of the Crow instability.

& Hussain [70], Saffman [84], Leweke & Williamson [60] and Marshall et al. [68] among many others. Spalart estimated the start time of linking at around 6τ with $\tau = 2\pi b^2/\Gamma$ the time it takes for the vortex pair to descend a distance b through mutual induction. Further information on the linking phenomenon is given in the introduction of Chapter 3.

The short wavelength or Widnall instability is an elliptic instability first described by Tsai & Widnall [94] on a Rankine vortex. Its characteristic wavelength is scaled on the vortex core radius a. The Widnall instability was analysed for a LO vortex by Eloy & Le Dizès [31] and Sipp & Jacquin [90]. Often both the Widnall and the Crow instabilities affect a vortex at the same time. In fact Laporte & Corjon [56] (numerically) and Leweke & Williamson [59] (experimentally) showed that the development of the Crow instability encourages that of the Widnall instability in the regions where the vortices get closer. This is observed clearly in figure 1.6 in which the vortex pair is affected by both the Crow and Widnall instabilities.

1.3 Vortex axisymmetrisation

In this paragraph we describe the vortex axisymmetrisation process. Modal stability theory predicts that an isolated vortex is asymptotically stable and therefore any disturbed vortex will eventually return to its original axisymmetric state. The axisymmetrisation mechanism, also known as the 'shear-diffusion' mechanism, relies on differential rotation by the base flow to wrap perturbations into spirals around the vortex core until the structures are sufficiently thin to be diffused by viscosity. The process takes place on a timescale of the order of $Re^{1/3}$. Descriptions of this mechanism are given by Melander et al. [72] and

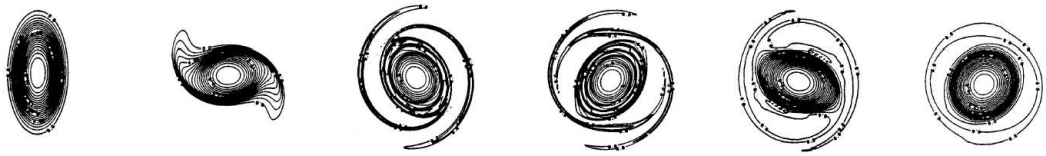

Figure 1.9: Axisymmetrisation of an elliptically deformed vortex, from Melander et al. [72].

Bernoff & Lingevitch [12]. An illustration of the axisymmetrisation of a disturbed vortex is provided in figure 1.9. The vortex is originally deformed by an elliptic perturbation. Differential advection stretches the outer extremities into filaments which wrap around the core and are eventually diffused. In the inviscid limit, the finely-wrapped structures cannot be diffused by viscosity. In this case the vorticity 'tends towards axisymmetry in a weak or coarse-grained sense' as defined by Bassom & Gilbert [9], that is on average the non-axisymmetric vorticity distribution tends to zero.

In some cases however, the natural axisymmetrisation process is bypassed and the flow transitions towards an entirely different quasi-steady flow configuration. Rossi et al. [82] demonstrated that when a quadrupolar perturbation of amplitude over a critical threshold is applied to a vortex, a quasi-steady tripolar state appears and decays on the viscous timescale. The same tripolar state can also be attained by imposing an external strain on the vortex. Similarly there exists a threshold over which the tripolar state persists even after the external strain has been removed (see Balmforth et al. [8], Macaskill et al. [63] and Turner & Gilbert [95]).

Dritschel [29] and Koumoutsakos [53] demonstrated that the capacity of a vortex to relax towards an axisymmetric state in the inviscid two-dimensional limit depends on the vorticity profile. Vortices presenting profiles with sufficently sharp edges can remain nonaxisymmetric, apparently indefinitely. Le Dizès [57] extended this study to finite Reynolds numbers. He showed that the potential for an isolated vortex to maintain an asymmetric state depends on the Habermann parameter $h = 1/(Re\epsilon^{3/2})$ with ϵ the amplitude of the asymmetric perturbation. If $h << 1$, then asymmetric perturbations persist due to the presence of a nonlinear critical layer in the velocity profile.

1.4 Vortex meandering

To date, vortex meandering is an unexplained behaviour of wing-tip vortices. Affected vortices undergo erratic displacement in the far-field as illustrated in figure 1.10. Experimental reproductions of trailing vortex flows also present the same behaviour [7, 22]. The origin of meandering is as yet unknown and has been attributed in turn to wind-tunnel effects, interaction with turbulence and cooperative instabilities. Jacquin et al. [47] explored all of these possibilities and came to the conclusion that none of them can be favoured above any other. Another hypothesis suggested by Antkowiak & Brancher [2] based on their study of the linear $m = 1$ optimal perturbation of a single vortex is that meandering is a result of transient growth (see § 1.6). More recently Edstrand et al. [30] obtained new results supporting the theory that meandering is caused by an instability. They extracted the coherent wandering motion from experimental PIV data and found an energetic $|m| = 1$ helical mode which could displace the vortex in the transverse plane. So far however, there is no conclusive proof of any of these theories.

Figure 1.10: Meandering of trailing vortices, from Brion [14].

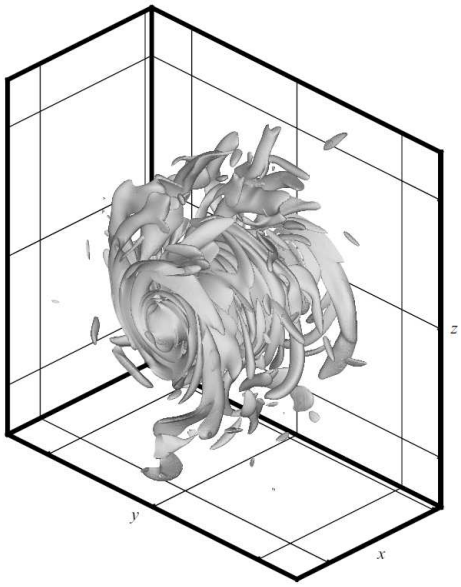

Figure 1.11: External turbulence structures wrapping around the vortex core, from Marshall & Beninati [67].

1.5 Interaction of vortices with external turbulence

It has been observed that when a steady vortex is submitted to a continual external excitation such as atmospheric turbulence, the external fluctuations are rearranged into ring-like shapes surrounding the vortex core and amplified. Melander & Hussain [71] and Marshall & Beninati [67] demonstrated numerically how small-scale structures are realigned in the azimuthal direction when interacting with a large-scale vortex. An illustration of the wrapping of the external turbulence around the vortex is provided in figure 1.11. The same phenomenon was observed experimentally by Beninati & Marshall [11]. Using Rapid Distortion Theory, Miyazaki & Hunt [74] showed that the perturbation growth generated during this phenomenon is algebraic which suggests it is a product of transient growth effects rather than an instability. An interesting similarity can be observed with the linear axisymmetric optimal perturbation described by Pradeep & Hussain [80] and Antkowiak & Brancher [3] which produces a stack of counter-rotating vortex rings. This implies that external turbulence naturally excites the optimal perturbations (see § 1.7) of the flow.

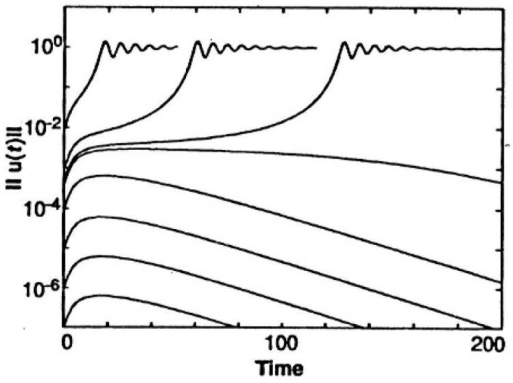

Figure 1.12: Nonlinear evolution of the perturbation amplitude for different initial values, from Trefethen et al. [93].

1.6 Non-normal stability analysis

Although modal stability analysis has correctly predicted the behaviour of several known instabilities, such as those presented in § 1.2, this method only provides information concerning the long-term behaviour of the flow and all short-term dynamics are omitted. It has been shown that some flows, although asymptotically stable, exhibit considerable perturbation amplification in the short term. This property has been characterised for many flows by Schmid & Henningson [87].

Transient growth occurs in flows for which the governing operator is non-normal. The eigenvectors of such an operator form a non-orthogonal set, so the superimposition of these modes in a flow can lead to algebraic perturbation growth. If the perturbation gains sufficient amplitude, the nonlinear terms of the flow become too strong to be neglected and can play a key role in disrupting the flow, or on the contrary, in saturating the instability and letting the flow go back to its original state. In some cases the flow is modified to an extent that a return to its original stable state is no longer possible; this is called the nonlinear bypass transition. Trefethen et al. [93] give a simple illustration of the bypass transition using a reduced model of a non-normal system (see figure 1.12). For small amplitudes the perturbations are amplified through transient growth and then decrease exponentially. However, above a critical amplitude a new nonlinear state is reached and the return to the original state is no longer achieved. Non-normal amplification has allowed the explanation of previously misunderstood experimental observations such as the appearance of turbulence in otherwise stable plane shear flows [87].

1.7 Optimal perturbations

The term optimal perturbation was first used by Farrell [36]. He defined the optimal perturbation as the initial condition that induces the largest perturbation growth over a given period of time T. The introduction of the time constraint T allows the study of flows at a more relevant timescale than modal stability theory which by definition describes the flow as $t \to \infty$. The general idea is that unstable modes with a weak growth rate could be supplemented by the transient growth of stable modes and therefore instability would be triggered early. In asymptotically stable flows, the aim would be to achieve sufficient amplification through transient growth to reach a bypass transition. Farrell determined a full description of the optimal perturbations of shear flows such as the Poiseuille flow and the plane Couette flow [17, 37].

The long-term linear optimal perturbation was shown by Farrell to correspond to the adjoint of the

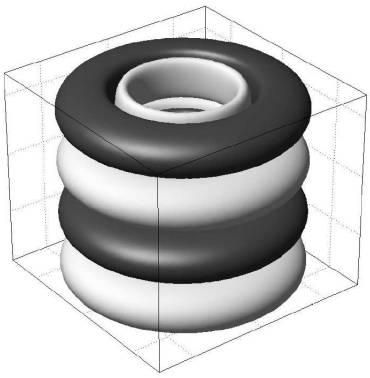

Figure 1.13: Counter-rotating vortex rings resulting from the evolution of the axisymmetric linear optimal perturbation of a Lamb-Oseen vortex with $Re = 1000$ and axial wavenumber $k = 0.9$, from Antkowiak [1].

most unstable mode of the flow. The adjoint $\mathcal{A}^+$ of an operator $\mathcal{A}$ is defined as follows:

$$(u, \mathcal{A}v) = \left(\mathcal{A}^+ u, v\right) \tag{1.7}$$

with $(\cdot, \cdot)$ the scalar product.

1.7.1 Linear optimal perturbations of a LO vortex

The Lamb-Oseen vortex is asymptotically stable according to modal stability analysis; it is stable with respect to both the Rayleigh centrifugal stability criterion and the inflexion point theorem. The eigenmodes of the Lamb-Oseen vortex were determined by Fabre et al. [34] and are composed of damped singular modes and Kelvin waves. However the Navier-Stokes operator is non-normal due to the differential rotation of the base flow. Strong transient perturbation growth is therefore possible in a LO vortex. A considerable amount of work has been undertaken to determine the optimal perturbations of vortex flows. The linear optimal perturbations of a LO vortex were described by Antkowiak & Brancher [2, 3] and Pradeep & Hussain [80].

The axisymmetric $m = 0$ optimal perturbation takes the form of a stack of alternating positive and negative azimuthal velocity streaks surrounding the vortex core [3]. These streaks evolve into a stack of counter-rotating rings of azimuthal vorticity through a mechanism described by Antkowiak & Brancher as the 'anti-lift-up' effect as it appears to be the reverse process of the lift-up effect commonly observed in shear flows (see Landahl [55]). An illustration of the resulting vortex rings is given in figure 1.13.

The nonaxisymmetric optimal perturbations of the LO vortex were described by Antkowiak & Brancher [2] for $m = 1$ and Pradeep & Hussain [80] for azimuthal wavenumbers up to $m = 4$. In these cases perturbation amplification is achieved through two inviscid mechanisms: an Orr-type shear mechanism and resonance. The shear mechanism is readily understood by observing the energy equation, as noted by Pradeep & Hussain:

$$\frac{dE}{dt} = P - D \qquad \text{with} \quad P = -\int_V u'v'r\frac{\partial}{\partial r}\left(\frac{V}{r}\right) dV \tag{1.8}$$

D is the dissipation term. The strain $S = r\partial_r(V/r)$ of a LO vortex is uniformly negative so energy production requires positive Reynolds stress $u'v'$. This ensures the shape of the optimal perturbation: a set of 'positive-tilt' vorticity spirals which correspond to streamlines of positive $u'v'$. The transient growth is stopped naturally as the differential rotation by the base flow transforms the positive-tilt spirals into negative-tilt spirals. A schematic defining positive and negative tilt spirals is shown in figure 1.14.

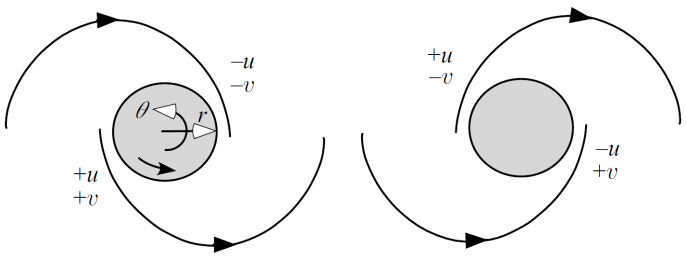

Figure 1.14: Positive-tilt (left) and negative-tilt (right) spirals, from Pradeep & Hussain [80].

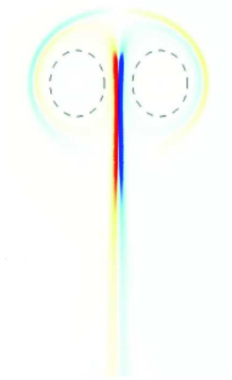

Figure 1.15: Axial vorticity contours of the linear optimal perturbation of the Crow instability. The vortex cores are located by dashed lines.

The second mechanism consists of a resonance phenomenon between the perturbation outside the vortex and core modes. Both Antkowiak & Brancher [2] and Pradeep & Hussain [80] showed that optimal perturbations tend to select a radial location for the initial perturbation that rotates at the frequency of the least stable mode of the vortex. Radial velocity u' is generated within the core through the advection of perturbation axial vorticity ω' by the base flow. This can be observed using the linearised Helmholtz equation:

$$\frac{\partial \omega'}{\partial t} + \frac{V}{r}\frac{\partial \omega'}{\partial \theta} + u'\frac{d\Omega}{dr} = \nu \Delta \omega' \tag{1.9}$$

where Ω is the base flow axial vorticity.

1.7.2 Linear optimal perturbation of a vortex pair

Returning to the aircraft wake problem, the linear optimal perturbation of a pair of counter-rotating vortices was determined numerically by Brion et al. [15] using a pair of LO vortices. The perturbation takes the form of a pair of opposite-signed vorticity sheets situated close to the plane separating the vortices (see figure 1.15). The perturbation is advected downwards by the base flow before being stretched at the leading hyperbolic point of the flow generating maximum amplification. The resulting perturbation corresponds to the Crow instability. The linear optimal perturbation or adjoint Crow mode leads to an acceleration of the perturbation growth and therefore of the vortex deformation by approximately 2.5τ with $\tau = 2\pi b^2/\Gamma$ the characteristic timescale of the vortex pair, b the distance separating the vortex cores and Γ the circulation.

1.7.3 Nonlinear optimal perturbations

All of the optimal perturbations described so far are linear: the contribution of the nonlinear terms was neglected throughout the optimisation process. However recent optimisation results for plane shear flows have shown that taking the nonlinear terms into account can produce significantly greater perturbation growth. Pringle & Kerswell [81] showed that the nonlinear optimal perturbation of a pipe flow can trigger transition to turbulence more effectively than the linear optimal. The same conclusion was reached by Cherubini & De Palma [19] for the plane Couette flow, Cherubini et al. [20] for the boundary layer transition and Farano et al. [35] for the plane Poiseuille flow. Nonlinear optimal perturbations tend to be more spatially localised and therefore appear to be more relevant for optimal excitation. Bisanti [13] carried out nonlinear optimal perturbation on an isolated LO vortex within the two-dimensional limit. He found that the nonlinear $m = 2$ optimal with sufficient initial energy leads to a transition of the flow to the tripolar quasi-steady state described in § 1.3, thus bypassing the axisymmetrisation process. Bisanti's results are used as a reference for the nonlinear optimisation work of this thesis and are reproduced in Chapter 4.

Chapter 2

Numerical methods

The work described in this thesis is entirely numerical. In this chapter the methods used are described and validated.

2.1 Direct Numerical simulations

Direct Numerical Simulations (DNS) are carried out using the incompressible Navier-Stokes solver Nek5000 [38], an open-source code based on the Spectral Element Method. Nek5000 was chosen for this study because of its renowned parallel performance, the direct availability of the adjoint solver and the potential to modify the source code. The flow is governed by the incompressible Navier-Stokes equations:

$$\nabla \cdot \boldsymbol{u} = 0 \tag{2.1}$$

$$\partial_t \boldsymbol{u} + (\boldsymbol{u} \cdot \nabla)\, \boldsymbol{u} = -\nabla p + \frac{1}{Re} \nabla^2 \boldsymbol{u} \tag{2.2}$$

with ∂_t the time derivative and Re the Reynolds number. The flow is decomposed into the base flow (upper case notation) and the perturbation field (prime notation). The amplitude of the perturbation is considered to be small in comparison with that of the base flow:

$$\boldsymbol{u} = \boldsymbol{U} + \epsilon \boldsymbol{u'} \tag{2.3}$$

$$p = P + \epsilon p' \qquad \text{with} \quad \epsilon << 1 \tag{2.4}$$

Introducing this decomposition into the Navier-Stokes equations, we obtain:

$$\nabla \cdot (\boldsymbol{U} + \epsilon \boldsymbol{u'}) = 0 \tag{2.5}$$

$$\partial_t (\boldsymbol{U} + \epsilon \boldsymbol{u'}) + \epsilon (\boldsymbol{U} \cdot \nabla)\, \boldsymbol{u'} + \epsilon (\boldsymbol{u'} \cdot \nabla)\, \boldsymbol{U} + \epsilon^2 (\boldsymbol{u'} \cdot \nabla)\, \boldsymbol{u'} = -\nabla (P + \epsilon p') + \frac{1}{Re} \nabla^2 (\boldsymbol{U} + \epsilon \boldsymbol{u'}) \tag{2.6}$$

At order 0 of ϵ we retrieve the Navier-Stokes equations applied to the base flow

$$\nabla \cdot \boldsymbol{U} = 0 \tag{2.7}$$

$$\partial_t \boldsymbol{U} + (\boldsymbol{U} \cdot \nabla)\, \boldsymbol{U} = -\nabla P + \frac{1}{Re} \nabla^2 \boldsymbol{U} \tag{2.8}$$

At first order of ϵ we obtain the linearised Navier-Stokes equations :

$$\nabla \cdot \boldsymbol{u'} = 0 \tag{2.9}$$

$$\partial_t \boldsymbol{u'} + (\boldsymbol{U} \cdot \nabla)\, \boldsymbol{u'} + (\boldsymbol{u'} \cdot \nabla)\, \boldsymbol{U} = -\nabla p' + \frac{1}{Re} \nabla^2 \boldsymbol{u'} \tag{2.10}$$

The nonlinear advection term $\epsilon^2 (u' \cdot \nabla) u'$ of equation 2.6 can be neglected when the perturbation is small. The linearised Navier-Stokes equations are implemented in Nek5000's perturbation mode which enables the resolution of the base and the perturbation flows separately.

2.1.1 Spatial discretisation

In Nek5000 the Navier-Stokes equations are solved using the Spectral Element Method (SEM). The SEM is an approximation scheme based on the Galerkin method and was introduced by Patera [78]. The SEM associates the geometrical flexibility of the Finite Element Method (FEM) with the rapid convergence and high accuracy of Spectral Methods. A concise description of the SEM is given in the following paragraph. Further details can be found in books by Deville et al. [23] and Karniadakis & Sherwin [51]. For clarity we will use the notations of [23].

As is the case with all Galerkin approximations, the discretised partial differential equations (PDE) need to be solved in their variational form. We consider the PDE defined as:

$$Lu = f \tag{2.11}$$

with L a differential operator. The variational form of this problem can be expressed :

$$A(u, v) = F(v) \qquad \forall v \in V \tag{2.12}$$

with A a bilinear form associated with the operator L by integration by parts and F a linear functional. An approximation u_N of the exact solution $\hat{u}$ is:

$$u_N(x) = \sum_{n=0}^{N} u_n \psi_n(x) \tag{2.13}$$

with $\{\psi_n\}$ a set of trial functions and $\{u_n\}$ coefficients to be determined, such that

$$A(u_N, v) = F(v) \qquad \forall v \in V_N \tag{2.14}$$

with $\{V_N\}$ a family of finite-dimensional subspaces of V. In all Galerkin methods the test functions $\{v\}$ are chosen to be the same as the trial functions $\{\psi_n\}$.

In Nek5000 the set of test and trial functions $\{\psi_n\}$ are based on the Legendre polynomials. This choice is the major difference between SEM and FEM. Besides orthogonality, the Legendre polynomials also give the best approximation in the H^1-norm. Considering a one-dimensional problem, as for the FEM (also a Galerkin approximation scheme) the integration domain (a, b) is divided into E elements:

$$a = x_0 < x_1 < ... < x_{E-1} < x_E = b \tag{2.15}$$

Ω^e denotes the element $\Omega^e = \{x | x_{e-1} < x < x_e\}, 1 \leq e \leq E$. For simplicity we define a reference element $\hat{\Omega} = \{\xi | -1 \leq \xi \leq 1\}$ onto which each Ω^e can be mapped. A linear space $P_p\left(\hat{\Omega}\right)$ of Legendre polynomials of degree p is defined on each element Ω^e. Pieced together over all the elements, the polynomials form the global basis $\{\psi_n\}_{n=0}^N$. $\Xi_{p+1} = \{\xi_0, \xi_1, .., \xi_p\}$ is the interpolation grid on the reference element $\hat{\Omega}$. To ensure C^0 continuity of the global functions, the borders $\hat{\Omega}$ must be nodes. To comply with this condition, Gauss-Lobatto-Legendre (GLL) quadrature points have been chosen. These points are the roots of the

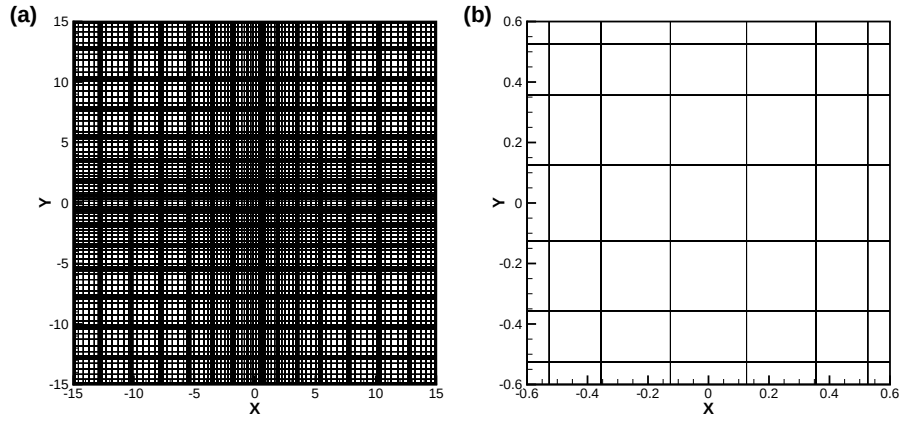

Figure 2.1: *(a)* Example of complete two-dimensional mesh with $E = 15 \times 15$ elements and $N = 8$ GLL points, refined in the centre of the domain, *(b)* distribution of $N = 8$ GLL points in a central element of the mesh.

following equation:

$$\left(1 - \xi_i^2\right) L'_N\left(\xi_i\right) = 0, \qquad \xi_i \in \hat{\Omega}, \quad i = 0, .., N \tag{2.16}$$

with L'_N the first derivative of the Legendre polynomial of degree N. The Lagrangian interpolation of any function $u\left(\xi\right)$ on the GLL points is:

$$I_N u\left(\xi\right) = \sum_{i=0}^{N} u\left(\xi_i\right) \pi_i\left(\xi\right), \qquad \xi \in \hat{\Omega} \tag{2.17}$$

with $\{\pi_i\}_{i=0}^N$ the associated interpolation basis of degree N. The function π_i is defined as:

$$\pi_i\left(\xi\right) = \frac{-1}{N(N+1)} \frac{\left(1 - \xi^2\right) L'_N\left(\xi\right)}{\left(\xi - \xi_i\right) L_N\left(\xi_i\right)} \qquad 0 \leq i \leq N, \quad \xi \in \hat{\Omega} \tag{2.18}$$

Therefore the spectral element approximation $u_N^e\left(x\right)$ of degree N in Ω^e mapped onto $\hat{\Omega}$ is given by:

$$u_N^e\left(\xi\right) = \sum_{i=0}^{N} u_i^e \pi_i\left(\xi\right), \qquad \xi \in \hat{\Omega} \tag{2.19}$$

To summarise, the spatial discretisation of the incompressible Navier-Stokes equations on the computational domain in Nek5000 is accomplished in two scales. First the domain is partitioned into E uniformly distributed elements, then a spectral polynomial approximation of order P is carried out on each individual element. Refining a mesh can therefore be achieved in two ways : one can either increase the number of spectral elements E or the polynomial order P. In practice, the second refinement method is favoured as the calculation converges exponentially with P. Examples of a complete spectral elements mesh and the distribution of GLL points on one element are given in figure 2.1. Here the mesh is refined in the centre of the domain where the vortices are situated.

2.1.2 Time scheme

Nek5000 uses a semi-implicit BDFk/EXTk time scheme to discretise the Navier-Stokes equations. The diffusion term is treated implicitly. The time derivative is approximated using the k-order Backward Differentiation formula. In order to avoid the complication of implicit discretisation of the nonsymmetric

convection term, a kth order extrapolation using values from $t^{n-q}, q = 1, .., k$ is implemented. The scheme is globally second-order accurate in time. The main cost of the calculation is in the implicit solve of the diffusion term.

As we intend to use the solver in perturbation mode (the perturbation velocity field is resolved separately) we choose the BDF2/EXT2 scheme as Nek5000 is not necessarily stable using perturbation mode with time order 3. The discretised Navier-Stokes equations yield:

$$\nabla \cdot \boldsymbol{u}^n = 0 \tag{2.20}$$

$$\frac{3\boldsymbol{u}^n - 4\boldsymbol{u}^{n-1} + \boldsymbol{u}^{n-2}}{2\Delta t} = -\nabla p^n + \frac{1}{Re}\nabla^2 \boldsymbol{u}^n - \left(2\left(\boldsymbol{u}\cdot\nabla\boldsymbol{u}\right)|_{t^{n-1}} - \left(\boldsymbol{u}\cdot\nabla\boldsymbol{u}\right)|_{t^{n-2}}\right) \tag{2.21}$$

The time step Δt is chosen to be constant for each calculation. Regarding stability, when using the BDF/EXT scheme Nek5000 imposes an upper boundary of 0.6 on the Courant-Friedrichs-Lewy number (CFL) defined as:

$$CFL = \frac{||u||\Delta t}{\Delta x} \tag{2.22}$$

with Δx the smallest spatial discretisation interval. Therefore considering an imposed minimum spatial interval Δx based on the characteristics of the simulated flow, the timestep Δt is chosen accordingly to adhere to the CFL constraint.

2.1.3 Boundary conditions

Depending on the nature of the flow that is simulated, the boundary conditions of the calculation vary. In the case of an isolated vortex, zero-stress conditions are imposed on the transverse boundaries and a periodic condition is applied in the axial direction. In the case of a counter-rotating vortex pair, the vortices propagate downwards through mutual induction. To keep the calculation domain in the referential moving with the vortex pair, a positive vertical velocity component is added to the flow. Dirichlet inflow and outflow conditions are imposed therefore on the vertical transverse boundaries, symmetric conditions on the horizontal transverse boundaries and periodic conditions in the axial direction. More detailed explanations are given in Chapter 3. In all simulations, the boundaries are placed sufficiently far from the main flow to ensure that their influence is negligible.

2.1.4 DNS validation

For all the results presented, the mesh refinement and the proximity of the domain boundaries were tested to ensure that the calculations are converged and the boundary conditions have no influence on the flow. An example of a validation process is as follows.

The simulations detailed in Chapter 3 were carried out on mesh 1 of table 2.1. The vortex axis is along the z-direction. In order to verify that the mesh is sufficiently refined, an identical simulation is carried out with half the number of elements ($E_x = E_y = E_z = 35$ instead of 70) in the mesh (mesh 2 of table 2.1). After 10 characteristic times of the flow, the relative difference between the values of the measured circulation is less than 0.1%. Similarly in order to check that the boundary conditions do not influence the flow, a simulation is carried out with a domain twice the size in the spanwise directions (mesh 3 of table 2.1). The relative difference in circulation is slightly higher (3%) but is considered to be sufficiently small to neglect the effects of the domain boundaries.

The next validation step is to compare results with existing studies. As discussed in Chapter 1 the Crow instability was first studied analytically by Crow [21] using a vortex filament method. In figure 2.2 the linear growth rates of the Crow instability for varying wavenumbers calculated using the present tool are compared with Crow's theoretical values. The classic bell shape with a growth maximum at

Mesh number	$[L_x, L_y, L_z]$	$[E_x, E_y, E_z]$	Relative difference of $\Gamma(t = 10)$ with mesh 1
1	$[8b, 8b, 7b]$	$[70, 70, 70]$	-
2	$[8b, 8b, 7b]$	$[35, 35, 35]$	$3.4E^{-4}$
3	$[16b, 16b, 7b]$	$[70, 70, 35]$	$2.9E^{-2}$

Table 2.1: Mesh validation: example of the counter-rotating vortex pair. Measure of the vortex circulation Γ at $t = 10$ with the time expressed in characteristic timescales. Effect of varying the mesh refinement and size.

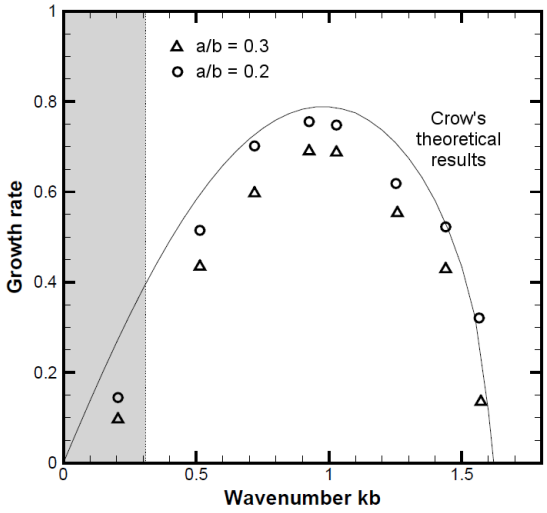

Figure 2.2: Simulated linear growth rates of the Crow instability for varying wavenumber compared with Crow's theoretical values (solid line).

approximately $kb = 0.9$ (with b the separation distance between the vortex cores) is obtained. In addition, as the aspect ratio a/b is reduced (a is the vortex core size) the growth rates move towards Crow's results which is consistent, as in his case, the vortex filaments have infinitesimal radii. An interesting observation is that as $kb \longrightarrow 0$ (see shaded area in figure 2.2) the Crow mode was found to be dominated by another mode closely resembling the two-dimensional mode of Brion et al. [16]. This superfluous mode had to be subtracted from the flow in order to obtain the Crow mode.

In an experimental study using a vortex generator in a water tank, Leweke & Williamson [60] measured the growth rate of the Crow instability as a function of the perturbation wavelength. The aspect ratio of the experimental vortex pair is $a/b = 0.22$ and the Reynolds number varies in $240 < Re < 400$. The growth rates calculated through DNS for the same aspect ratio and $Re = 320$ are compared with their experimental results in figure 2.3. The results compare well with an average error of less than 10%. The reason for the disparity is likely to be the difference in Reynolds number or differences in the exact vortex geometries due to the way they are formed in the experiment (by a flapping plate), while in the calculation the flow is started from purely Gaussian vortices. Other possible sources of discrepancy include the existence of parasite velocity created by the closing of the generator plates, limitations to the PIV measurements and dye visualisations from the experimental side and numerical dissipation for the DNS. Taking all of this into account, the similarity of the results is remarkably good.

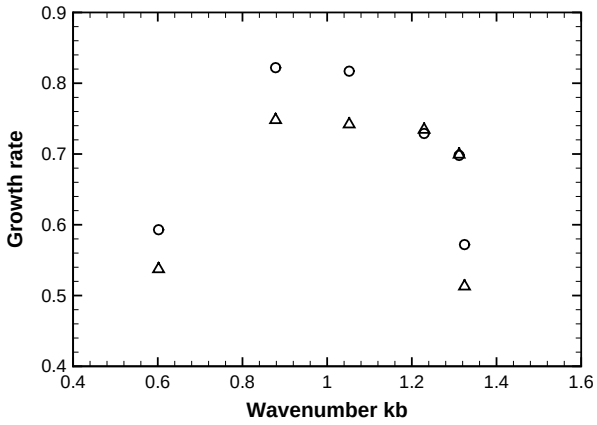

Figure 2.3: Crow instability growth rates as a function of the instability wavenumber kb obtained using DNS for a vortex pair of aspect ratio $a/b = 0.22$ and $Re = 320$ (circles) compared with the experimental results of Leweke and Williamson [60] (triangles).

2.2 Optimisation method

A large part of this thesis is dedicated to determining the nonlinear optimal perturbations of various vortical flows. The objective is to find the most dangerous disturbance to a flow, that is to say, the disturbance of given energy E_0 that generates the greatest perturbation growth over a horizon time T. Optimal disturbances at finite times rely on growth mechanisms permitted by the non-normal character of the Navier-Stokes operator (see Schmid & Henningson [87]). One quantitative measure of perturbation growth is the perturbation kinetic energy $E(t)$:

$$E(t) = \int_V \boldsymbol{u}'^2(t) dV \tag{2.23}$$

with $\boldsymbol{u}'$ the perturbation velocity and V the domain volume. Other measures, such as the enstrophy $\zeta = \int_V \boldsymbol{\omega}'^2 dV$ with $\boldsymbol{\omega}'$ the perturbation vorticity, could be used and have been shown to provide quite similar results [13].

To determine the optimal perturbation, the gain of perturbation kinetic energy $G(t) = E(t)/E_0$ is maximised using a Lagrangian multiplier technique [97] that enforces the constraints imposed by the flow dynamics and boundary conditions. For a given problem, the functional $\mathcal{L}$ is constructed:

$$\mathcal{L}\left(\boldsymbol{q}, \boldsymbol{q}^+, \boldsymbol{u}_0, \boldsymbol{u}_0^+\right) = \mathcal{J}\left(\boldsymbol{q}, \boldsymbol{u}_0\right) - \langle \boldsymbol{q}^+, \mathcal{F}\left(\boldsymbol{q}, \boldsymbol{u}_0, \boldsymbol{u}_0^+\right)\rangle \tag{2.24}$$

where $\boldsymbol{q}$ is the vector of problem variables, $\boldsymbol{u}_0$ is the initial condition, $\boldsymbol{q}^+$ and $\boldsymbol{u}_0^+$ are Lagrange multipliers, and $\langle \cdot, \cdot \rangle$ is the spatio-temporal scalar product. $\mathcal{J}$ is the cost functional to be optimised and here is the gain of kinetic energy at the given horizon time T, $G(T)$. $\mathcal{F}$ is a function grouping all the constraints applied to the problem. In the context of this work, the constraints are the Navier-Stokes equations and the initial and boundary conditions. The variables of the problem are the perturbation velocity, initial perturbation velocity and pressure such that $\boldsymbol{q} = (u, v, w, p)$. Note that for simplicity, we drop the prime notation for the remainder of this chapter: the base flow velocity is indicated by upper case letters and the perturbation velocity by lower case letters. The Lagrange variables or adjoint variables

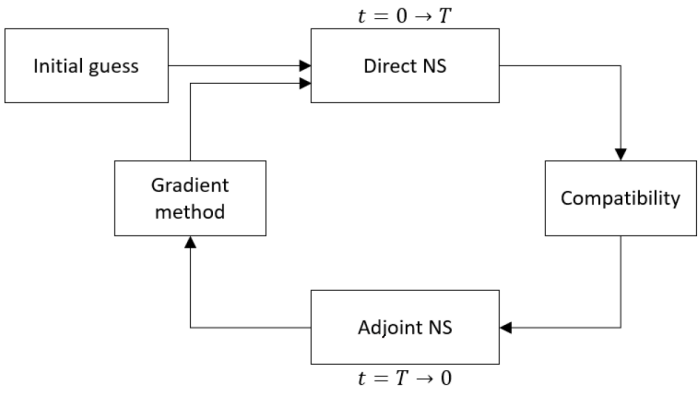

Figure 2.4: Sketch of optimisation cycle.

are $\boldsymbol{q}^+ = (u^+, v^+, w^+, p^+)$. A more explicit form of the Lagrangian functional is:

$$\mathcal{L}\left(\boldsymbol{q}, \boldsymbol{q}^+, \boldsymbol{u}_0, \boldsymbol{u}_0^+\right) = \frac{\int_V \boldsymbol{u}(T)^2 dV}{\int_V \boldsymbol{u}_0^2 dV} - \int_0^T \int_V \boldsymbol{u}^+ \cdot \left(\frac{D\boldsymbol{u}}{Dt} + \nabla p - \frac{1}{Re}\Delta \boldsymbol{u}\right) dV dt \tag{2.25}$$

$$- \int_0^T \int_V p^+ \nabla \cdot \boldsymbol{u} dV dt - \int_V \boldsymbol{u}_0^+ \cdot (\boldsymbol{u}(0) - \boldsymbol{u}_0)\, dV \tag{2.26}$$

with D/Dt the particular derivative. Note that the form of the advection term of Du/Dt will depend on whether the linearised or fully nonlinear Navier-Stokes equations are being resolved. Setting to zero the first derivatives of the Lagrangian functional $\mathcal{L}$ with respect to each of the variables yields the equations to resolve:

$$\partial_{\boldsymbol{q}^+}\mathcal{L} = 0 \implies \partial_{\boldsymbol{q}^+}\mathcal{J}^+ = \partial_{\boldsymbol{q}^+}\mathcal{F}^+\boldsymbol{q}^+ \quad \text{gives the Navier-Stokes equations,} \tag{2.27}$$

$$\partial_{\boldsymbol{q}}\mathcal{L} = 0 \implies \partial_{\boldsymbol{q}}\mathcal{J}^+ = \partial_{\boldsymbol{q}}\mathcal{F}^+\boldsymbol{q}^+ \quad \text{gives the adjoint Navier-Stokes equations,} \tag{2.28}$$

$$\partial_{\boldsymbol{u}_0}\mathcal{L} = 0 \implies \partial_{\boldsymbol{u}_0}\mathcal{J}^+ = \partial_{\boldsymbol{u}_0}\mathcal{F}^+\boldsymbol{q}^+ \quad \text{gives the steepest ascent direction,} \tag{2.29}$$

$$\partial_{\boldsymbol{u}_0^+}\mathcal{L} = 0 \implies \partial_{\boldsymbol{u}_0^+}\mathcal{J}^+ = \partial_{\boldsymbol{u}_0^+}\mathcal{F}^+\boldsymbol{q}^+ \quad \text{gives the compatibility equations.} \tag{2.30}$$

The first derivatives of the Lagrangian functional are defined, for example, as:

$$\partial_{\boldsymbol{q}^+}\mathcal{L} \quad \boldsymbol{\delta q}^+ = lim_{\epsilon \rightarrow 0} \frac{\mathcal{L}\left(\boldsymbol{q}, \boldsymbol{q}^+ + \epsilon \boldsymbol{\delta q}^+, \boldsymbol{u}_0, \boldsymbol{u}_0^+\right) - \mathcal{L}\left(\boldsymbol{q}, \boldsymbol{q}^+, \boldsymbol{u}_0, \boldsymbol{u}_0^+\right)}{\epsilon} \tag{2.31}$$

At $t = T$, the variables $\boldsymbol{q}$ and $\boldsymbol{q}^+$ are linked through the compatibility equations. The optimisation is carried out using an iteration method:

(i) An initial guess for $\boldsymbol{u}\,(t = 0)$ is made and the Navier-Stokes equations are integrated to time $t = T$.

(ii) The compatibility equations provide the final adjoint field $\boldsymbol{u}^+\,(t = T)$.

(iii) The adjoint variables evolve backwards in time through the adjoint Navier-Stokes equations.

(iv) The new initial field $\boldsymbol{u}\,(t = 0)$ is calculated using the steepest ascent direction or gradient.

This procedure is repeated until there is convergence to a solution. Figure 2.4 shows a sketch of the iteration method. Rapid convergence is achieved by using a gradient-based update method such as those described in § 2.2.3. Having outlined the method, the equations used in the linear and nonlinear

optimisation calculations are provided in the following paragraphs. First the linear optimisation algorithm is detailed, followed by the nonlinear version, in order to best highlight the complications introduced by including the nonlinear terms in the optimisation process.

2.2.1 Linear optimisation

The linearised Navier-Stokes equations are recalled:

$$\nabla \cdot \boldsymbol{u} = 0 \tag{2.32}$$

$$\partial_t \boldsymbol{u} + (\boldsymbol{U} \cdot \nabla)\, \boldsymbol{u} + (\boldsymbol{u} \cdot \nabla)\, \boldsymbol{U} = -\nabla p + \frac{1}{Re} \nabla^2 \boldsymbol{u} \tag{2.33}$$

The functional $\mathcal{L}$ expressed in detail gives:

$$\begin{aligned}
\mathcal{L}\left(u, v, w, p, u_0, v_0, w_0, u^+, v^+, w^+, p^+, u_0^+, v_0^+, w_0^+\right) = & \frac{\int_V \left(u^2(T) + v^2(T) + w^2(T)\right) dV}{\int_V \left(u_0^2 + v_0^2 + w_0^2\right) dV} \\
& - \int_T \int_V p^+ \left(\partial_x u + \partial_y v + \partial_z w\right) dV dt \\
& - \int_T \int_V u^+ \left(\partial_t u + U\partial_x u + V\partial_y u + W\partial_z u + u\partial_x U + v\partial_y U + w\partial_z U + \partial_x p - \frac{1}{Re}\Delta u\right) dV dt \\
& - \int_T \int_V v^+ \left(\partial_t v + U\partial_x v + V\partial_y v + W\partial_z v + u\partial_x V + v\partial_y V + w\partial_z V + \partial_y p - \frac{1}{Re}\Delta v\right) dV dt \\
& - \int_T \int_V w^+ \left(\partial_t w + U\partial_x w + V\partial_y w + W\partial_z w + u\partial_x W + v\partial_y W + w\partial_z W + \partial_z p - \frac{1}{Re}\Delta w\right) dV dt \\
& - \int_V u_0^+ \left(u(0) - u_0\right) dV - \int_V v_0^+ \left(v(0) - v_0\right) dV - \int_V w_0^+ \left(w(0) - w_0\right) dV
\end{aligned} \tag{2.34}$$

The aim is to search for the extrema of $\mathcal{L}$, therefore $\mathcal{L}$ is derived with respect to each of the independant variables. By deriving $\mathcal{L}$ with respect to u, v, w and p and applying successive integration by parts, we determine the adjoint equations of the problem:

$$\partial_x u^+ + \partial_y v^+ + \partial_z w^+ = 0 \tag{2.35}$$

$$\partial_t u^+ - U\partial_x u^+ - V\partial_y u^+ - W\partial_z u^+ = -u^+\partial_x U - v^+\partial_x V - w^+\partial_x W + \partial_x p^+ + \frac{1}{Re}\Delta u^+ \tag{2.36}$$

$$\partial_t v^+ - U\partial_x v^+ - V\partial_y v^+ - W\partial_z v^+ = -u^+\partial_y U - v^+\partial_y V - w^+\partial_y W + \partial_y p^+ + \frac{1}{Re}\Delta v^+ \tag{2.37}$$

$$\partial_t w^+ - U\partial_x w^+ - V\partial_y w^+ - W\partial_z w^+ = -u^+\partial_z U - v^+\partial_z V - w^+\partial_z W + \partial_z p^+ + \frac{1}{Re}\Delta w^+ \tag{2.38}$$

or in a more compact form:

$$\nabla \cdot \boldsymbol{u}^+ = 0 \tag{2.39}$$

$$\partial_t \boldsymbol{u}^+ - (\boldsymbol{U} \cdot \nabla)\boldsymbol{u}^+ = -\boldsymbol{u}^+ \cdot (\nabla \boldsymbol{U})^T + \nabla p^+ + \frac{1}{Re}\Delta \boldsymbol{u}^+ \tag{2.40}$$

and the compatibility equations:

$$\boldsymbol{u}^+(T) = 2\frac{\boldsymbol{u}(T)}{E_0} \tag{2.41}$$

Derivation with respect to the initial condition u_0, v_0, w_0 yields the steepest ascent direction or gradient:

$$\partial_{\boldsymbol{u}_0} \mathcal{L} = -2\frac{E_T}{E_0^2}\boldsymbol{u}(0) + \boldsymbol{u}^+(0) \tag{2.42}$$

with $E_T = E(t = T)$. Note that derivation of the functional $\mathcal{L}$ with respect to the adjoint variables gives

the Navier-Stokes equations. Optimality conditions are obtained by setting the gradient with respect to the initial condition $\boldsymbol{\partial_{u_0}\mathcal{L}}$ to zero. Either one can apply the optimality conditions to determine the new initial perturbation $\boldsymbol{u}\,(t=0)$ or, for faster convergence, adopt a gradient-based update method such as that used by Marquet et al. [66] (see § 2.2.3).

2.2.2 Nonlinear optimisation

Including the nonlinear terms in the Navier-Stokes equations in the optimisation process introduces several complications. The full expression of the Navier-Stokes equations when distinguishing the base flow and perturbation fields is:

$$\nabla \cdot \boldsymbol{u} = 0 \tag{2.43}$$

$$\partial_t \boldsymbol{u} + (\boldsymbol{U}\cdot\nabla)\,\boldsymbol{u} + (\boldsymbol{u}\cdot\nabla)\,\boldsymbol{U} + (\boldsymbol{u}\cdot\nabla)\,\boldsymbol{u} = -\nabla p + \frac{1}{Re}\nabla^2\boldsymbol{u} \tag{2.44}$$

Applying the same method to these equations as for the linear optimisation, a slightly different set of adjoint equations is obtained:

$$\partial_x u^+ + \partial_y v^+ + \partial_z w^+ = 0 \tag{2.45}$$

$$\begin{aligned}\partial_t u^+ - U\partial_x u^+ - V\partial_y u^+ - W\partial_z u^+ = -u^+\partial_x U - v^+\partial_x V - w^+\partial_x W + \partial_x p^+ + \frac{1}{Re}\Delta u^+ \\ + 2u\partial_x u^+ + v\partial_y u^+ + w\partial_z u^+ + v\partial_x v^+ + w\partial_x w^+\end{aligned} \tag{2.46}$$

$$\begin{aligned}\partial_t v^+ - U\partial_x v^+ - V\partial_y v^+ - W\partial_z v^+ = -u^+\partial_y U - v^+\partial_y V - w^+\partial_y W + \partial_y p^+ + \frac{1}{Re}\Delta v^+ \\ + u\partial_x v^+ + 2v\partial_y v^+ + w\partial_z v^+ + u\partial_y u^+ + w\partial_y w^+\end{aligned} \tag{2.47}$$

$$\begin{aligned}\partial_t w^+ - U\partial_x w^+ - V\partial_y w^+ - W\partial_z w^+ = -u^+\partial_z U - v^+\partial_z V - w^+\partial_z W + \partial_z p^+ + \frac{1}{Re}\Delta w^+ \\ + u\partial_x w^+ + v\partial_y w^+ + 2w\partial_z w^+ + u\partial_z u^+ + v\partial_z v^+\end{aligned} \tag{2.48}$$

or in a more compact form:

$$\nabla \cdot \boldsymbol{u}^+ = 0 \tag{2.49}$$

$$\partial_t \boldsymbol{u}^+ - (\boldsymbol{U}\cdot\nabla)\boldsymbol{u}^+ - (\boldsymbol{u}\cdot\nabla)\boldsymbol{u}^+ = -\boldsymbol{u}^+\cdot(\nabla\boldsymbol{U})^T + \boldsymbol{u}\cdot(\nabla\boldsymbol{u}^+)^T + \nabla p^+ + \frac{1}{Re}\Delta\boldsymbol{u}^+ \tag{2.50}$$

The most important change lies in the adjoint momentum conservation equations (2.46) - (2.48): the adjoint solution $\boldsymbol{u}^+$ is directly dependant on $\boldsymbol{u}$. In practice, this involves saving the velocity field at every time step during the Navier-Stokes integration and reloading it for each time step of the adjoint integration. As a consequence the computation time and memory costs are significantly larger than in the linear framework.

The nonlinear analysis also introduces a new parameter E_0, the initial perturbation energy with respect to that of the base flow. For small values $E_0 \ll 1$ the optimal perturbation will be very close to the linear solution. As E_0 grows, the nonlinear terms gain in importance and can eventually dominate the flow. Unlike other authors of nonlinear optimisations such as Cherubini et al. [20] and Pringle & Kerswell [81], it was decided not to include this condition in the constraints on the Lagrangian functional but in the update step. Various commonly used update techniques, including the rotation method

employed in this work, are detailed in the next paragraph.

2.2.3 Gradient-based update methods

The update of the solution $\boldsymbol{u}(t=0)$ can be achieved using a variety of gradient-based methods, three of which are described below.

- **Steepest ascent method**

  The update at iteration $j+1$ of the optimal solution using the steepest ascent method has the following form:

  $$\boldsymbol{u}(0)^{j+1} = \boldsymbol{u}(0)^{j} + \alpha \boldsymbol{\partial}_{\boldsymbol{u_0}} \boldsymbol{\mathcal{L}}^{j} \tag{2.51}$$

  with α the advance step size. Within this method, at each iteration $j+1$, a step is taken in the direction of greatest ascent based on the previous iteration j. Imposing the value of the initial perturbation energy $E(t=0) = E_0$ after updating the solution leads to a second degree equation in α:

  $$\int_V \boldsymbol{u}^{j+1}(0)^2 \, dV = E_0 \qquad \Longleftrightarrow \tag{2.52}$$

  $$\int_V \boldsymbol{u}^{j}(0)^2 \, dV + 2\alpha \int_V \boldsymbol{u}^{j}(0) \, \boldsymbol{\partial}_{\boldsymbol{u_0}} \boldsymbol{\mathcal{L}}^{j} dV + \alpha^2 \int_V \left(\boldsymbol{\partial}_{\boldsymbol{u_0}} \boldsymbol{\mathcal{L}}^{j}\right)^2 dV = E_0 \tag{2.53}$$

  Only one of the two roots is physically acceptable and the step length α takes this value.

- **Rotation method**

  The rotation method [26] is based on the same principle as the steepest ascent method but uses geometrical arguments to satisfy the initial energy constraint. From the gradient $\boldsymbol{\partial}_{\boldsymbol{u_0}} \boldsymbol{\mathcal{L}}^{j}$ only the component $\boldsymbol{\partial}_{\boldsymbol{u_0}} \boldsymbol{\mathcal{L}}^{j}_{\perp}$ that is orthogonal to the initial state $\boldsymbol{u}(0)^{j}$ is retained:

  $$\boldsymbol{\partial}_{\boldsymbol{u_0}} \boldsymbol{\mathcal{L}}^{j}_{\perp} = \boldsymbol{\partial}_{\boldsymbol{u_0}} \boldsymbol{\mathcal{L}}^{j} - \frac{\boldsymbol{u}(0)^{j\top} \boldsymbol{\partial}_{\boldsymbol{u_0}} \boldsymbol{\mathcal{L}}^{j}}{\boldsymbol{u}(0)^{j\top} \boldsymbol{u}(0)^{j}} \boldsymbol{u}(0)^{j} \tag{2.54}$$

  This vector is then scaled to the initial energy constraint:

  $$\boldsymbol{N}^{j} = E_0^{1/2} \frac{\boldsymbol{\partial}_{\boldsymbol{u_0}} \boldsymbol{\mathcal{L}}^{\boldsymbol{j}}{}_{\perp}}{||\boldsymbol{\partial}_{\boldsymbol{u_0}} \boldsymbol{\mathcal{L}}^{j}_{\perp}||} \tag{2.55}$$

  The update of the initial field is then achieved by:

  $$\boldsymbol{u}(0)^{j+1} = \boldsymbol{u}(0)^{j} \, cos(\alpha) + \boldsymbol{N}^{j} \, sin(\alpha) \tag{2.56}$$

  with α the optimal step length determined using a line search algorithm. An illustration of the rotation method is given in figure 2.5 for a two-dimensional example. The initial energy constraint E_0 is represented by a circle.

- **Conjugate gradient method**

  The conjugate gradient technique aims to provide a more accurate gradient for iteration $j+1$ by taking into account the previous gradient direction obtained at iteration j. The new step direction $\boldsymbol{r}^{j+1}$ is therefore calculated using:

  $$\boldsymbol{r}^{j+1} = -\boldsymbol{\partial}_{\boldsymbol{u_0}} \boldsymbol{\mathcal{L}}^{j+1} + \beta^{j+1} \boldsymbol{r}^{j} \tag{2.57}$$

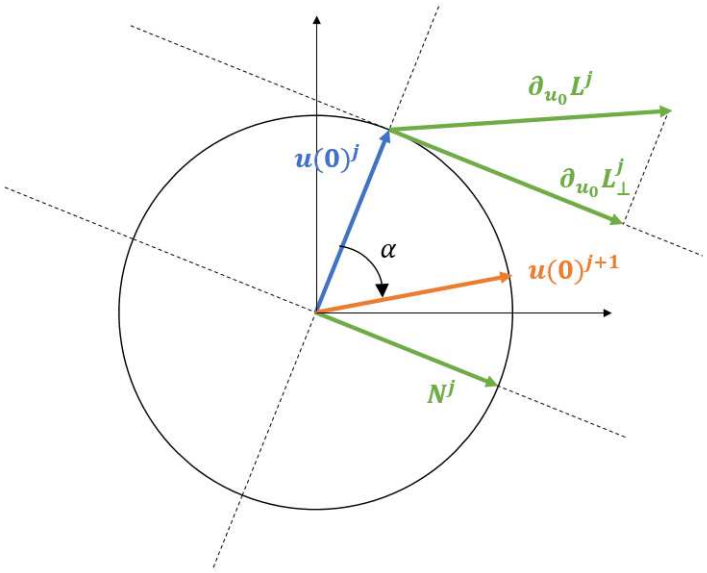

Figure 2.5: Illustration of the rotation method update procedure for a two-dimensional problem.

with $\boldsymbol{r}^1 = -\boldsymbol{\partial}_{\boldsymbol{u}_0}\boldsymbol{\mathcal{L}}^1$ and

$$\beta^{j+1} = \frac{\boldsymbol{r}^{j+1\top}\boldsymbol{r}^{j+1}}{\boldsymbol{r}^{j\top}\boldsymbol{r}^{j}} \tag{2.58}$$

The initial field update is then:

$$\boldsymbol{u}\,(0)^{j+1} = \boldsymbol{u}\,(0)^{j} + \alpha \boldsymbol{r}^{j+1} \tag{2.59}$$

As for the rotation method, a line search method is used to determine the optimal step length α. This method can be combined effectively with the rotation method as described by Foures et al. [40].

Further details on all of these methods can be found in works such as [76] and [26]. Having experimented with the various possible gradient-based update methods presented here, it was found that the most consistent and rapidly converging results were obtained by using the rotation method. All the results presented in this thesis were obtained with this technique.

2.2.4 Validation of the optimisation tool

The mesh used during the optimisation calculations is a disc of radius $R = 15a$ with a the vortex dispersion radius. The refinement of the mesh is tested by modifying the polynomial order P of the spectral approximation. The results of these convergence tests are presented in table 2.2. Varying the mesh refinement clearly has very little effect on the value of the optimal gain. Mesh 2 (see table 2.2) is used throughout the study.

The effect of the boundary conditions is also tested. As shown in table 2.2 the optimal gain for mesh 2 in the case ($Re = 5000, T = 4.8, E_0 = 10^{-2}$) is $G(T) = 140.78$. A mesh with the same refinement but with boundary conditions situated further from the vortex ($R = 27a$) gives an optimal gain of $G(T) = 141.98$, giving a relative difference of less than 0.9% between the two meshes.

In the case of perturbations with $m = 1$ symmetry, a problem arose at the beginning of the study. $m = 1$ modes are particularly receptive to distant perturbations. As such, spurious low intensity vorticity patches appeared at the domain boundaries, exciting non-physical modes in the vortex core. This problem is resolved by introducing a viscous buffer zone at the vortex boundaries. The viscosity is increased from

Mesh number	P	Optimal gain $G(T)$
1	7	140.21
2	10	140.78
3	13	140.77

Table 2.2: Optimal gain for the case $Re = 5000$, $T = 4.8$, $E_0 = 10^{-2}$ for different mesh refinements.

Reference work	Re	T	$G(T)$	Present results
Antkowiak & Brancher [2]	1000	40	770	764
Pradeep & Hussain [80]	796	9.88	62	63

Table 2.3: Gain reached with the $m = 1$ linear optimal perturbation at Reynolds number Re and horizon time T - comparison with other works.

$\nu = Re^{-1}$ at $r = 12$ to $\nu = 0.1$ at the external boundary $r = R$. This appears to alleviate the problem. It is interesting to note that this issue is encountered only for the linear optimisations, the nonlinear optimal perturbations are not affected.

Finally, to ensure the validity of the optimisation results, optimal gains for a 2D isolated vortex are compared with values provided in other studies. An example of this validation stage is shown in table 2.3 where linear optimal gains for modes of azimuthal wavenumber $m = 1$ obtained by Antkowiak & Brancher [2] and Pradeep & Hussain [80] are reproduced and closely matched. As to our knowledge no published nonlinear optimisation work exists (other than the PhD work of Bisanti [13]), no comparisons of nonlinear results are possible as yet. However, applying the nonlinear optimisation tool with small initial amplitude $E_0 << 1$ gives the same results as the linear tool. In addition, in Chapter 4 the nonlinear results of Bisanti are retrieved thus giving confidence in the nonlinear code's validity.

2.3 Finite Element linear optimisation tool

In the interests of speeding up the determination of linear optimal perturbations for immediate validation of the optimisation results, a one-dimensional linear optimisation tool is developed using the Finite Element solver FreeFem++ [43]. Results obtained from this tool are presented in Chapters 4 and 6. The linearised Navier-Stokes equations are solved to obtain a normal mode solution. The base flow, composed of an isolated Lamb-Oseen vortex, is considered to be frozen. The velocity profile of the Lamb-Oseen vortex is $\boldsymbol{U} = (0, V, 0)^T$ (in cylindrical coordinates) with the azimuthal velocity:

$$V(r) = \frac{\Gamma}{2\pi r}\left(1 - exp\left(-r^2/a^2\right)\right) \tag{2.60}$$

a is the vortex dispersion radius and Γ is the circulation.

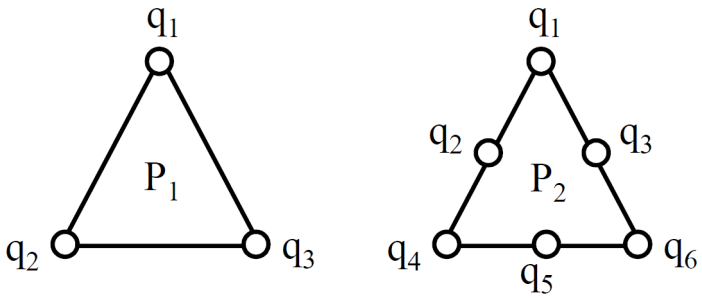

Figure 2.6: Finite element P_1 and P_2 discretisation. Degrees of freedom are denoted q_i.

2.3.1 Spatial discretisation

As explained in § 2.1.1 the Finite Element Method is based on a variational formulation of the equations. We use Taylor Hood finite elements of second order P_2 for the velocity components and of the first order P_1 for the pressure. These elements and their degrees of freedom are represented in figure 2.6.

2.3.2 Time scheme

We resolve the linearised Navier-Stokes equations in cylindrical coordinates:

$$\frac{1}{r}\partial_r\left(ru\right)+\frac{1}{r}\partial_\theta v+\partial_z w=0 \tag{2.61}$$

$$\partial_t u+\frac{V}{r}\partial_\theta u-\frac{2V}{r}v=-\partial_r p+\frac{1}{Re}\left[\frac{1}{r}\partial_r\left(r\partial_r u\right)+\frac{1}{r^2}\partial_\theta^2 u+\partial_z^2 u-\frac{u}{r^2}-\frac{2}{r^2}\partial_\theta v\right] \tag{2.62}$$

$$\partial_t v+\partial_r V u+\frac{V}{r}\partial_\theta v+\frac{V}{r}u=-\frac{1}{r}\partial_\theta p+\frac{1}{Re}\left[\frac{1}{r}\partial_r\left(r\partial_r v\right)+\frac{1}{r^2}\partial_\theta^2 v+\partial_z^2 v+\frac{2}{r^2}\partial_\theta u-\frac{v}{r^2}\right] \tag{2.63}$$

$$\partial_t w+\frac{V}{r}\partial_\theta w=-\partial_z p+\frac{1}{Re}\left[\frac{1}{r}\partial_r\left(r\partial_r w\right)+\frac{1}{r^2}\partial_\theta^2 w+\partial_z^2 w\right] \tag{2.64}$$

Note that the prime notation has again been omitted: upper case letters refer to the base flow and lower case letters to the perturbation. Upon introducing $\boldsymbol{q}=\hat{\boldsymbol{q}}e^{im\theta+ikz}$ the equations read:

$$\partial_r\left(r\hat{u}\right)+im\hat{v}+ikr\hat{w}=0 \tag{2.65}$$

$$r^2\partial_t\hat{u}+imrV\hat{u}-2rV\hat{v}=-r^2\partial_r\hat{p}+\frac{1}{Re}\left[r\partial_r\left(r\partial_r\hat{u}\right)-(m^2+k^2r^2+1)\hat{u}-2im\hat{v}\right] \tag{2.66}$$

$$r^2\partial_t\hat{v}+imrV\hat{v}+\left(r^2\partial_r V+rV\right)\hat{u}=-imr\hat{p}+\frac{1}{Re}\left[r\partial_r\left(r\partial_r\hat{v}\right)-\left(m^2+k^2r^2+1\right)\hat{v}+2im\hat{u}\right] \tag{2.67}$$

$$r^2\partial_t\hat{w}+imrV\hat{w}=-ikr^2\hat{p}+\frac{1}{Re}\left[r\partial_r\left(r\partial_r\hat{w}\right)-(m^2+k^2r^2)\hat{w}\right] \tag{2.68}$$

The solution $\hat{\boldsymbol{q}}_{n+1}=(\hat{u},\hat{v},\hat{w},\hat{p})^T_{n+1}$ at time t_{n+1} is calculated as a function of the previous solutions $\hat{\boldsymbol{q}}_n$ and $\hat{\boldsymbol{q}}_{n-1}$. The linear terms of the Navier-Stokes equations above are handled semi-implicitly with the Backward Differentiation Formula scheme of order 2 (BDF2). The discretised time derivative is expressed, at order 1:

$$\partial_t\boldsymbol{u}=\frac{\boldsymbol{u}^{n+1}-\boldsymbol{u}^n}{\Delta t} \tag{2.69}$$

and at order 2:

$$\partial_t\boldsymbol{u}=\frac{3\boldsymbol{u}^{n+1}-4\boldsymbol{u}^n+\boldsymbol{u}^{n-1}}{2\Delta t} \tag{2.70}$$

with Δt the time step. The integration is started at order 1 and changes to order 2 after two iterations. If we group the $n+1$ terms on the left-hand side and the explicit terms on the right:

$$\frac{3}{2}\boldsymbol{u}^{n+1} - \Delta t \Lambda\left(\boldsymbol{q}^{n+1}\right) = 2\boldsymbol{u}^{n} - \frac{1}{2}\boldsymbol{u}^{n-1} \tag{2.71}$$

with $\Lambda\left(\boldsymbol{q}^{n+1}\right)$ the linear terms of the Navier-Stokes equations.

2.3.3 Normal modes

Normal modes are solutions of the linearised Navier-Stokes equations of the form $\hat{\boldsymbol{q}} = \tilde{\boldsymbol{q}}e^{\sigma t}$, with $\tilde{\boldsymbol{q}}$ the normal mode and σ a complex frequency $\sigma = \sigma_R + i\sigma_I$ with σ_R the growth rate and σ_I the frequency. After introduction into the linearised Navier-Stokes equations, we obtain:

$$\partial_r\left(r\tilde{u}\right) + im\tilde{v} + ikr\tilde{w} = 0 \tag{2.72}$$

$$\left(r^2\sigma + imrV\right)\tilde{u} - 2rV\tilde{v} = -r^2\partial_r\tilde{p} + \frac{1}{Re}\left[r\partial_r\left(r\partial_r\tilde{u}\right) - (m^2 + k^2r^2 + 1)\tilde{u} - 2im\tilde{v}\right] \tag{2.73}$$

$$\left(r^2\sigma + imrV\right)\tilde{v} + \left(r^2\partial_r V + rV\right)\tilde{u} = -imr\tilde{p} + \frac{1}{Re}\left[r\partial_r\left(r\partial_r\tilde{v}\right) - \left(m^2 + k^2r^2 + 1\right)\tilde{v} + 2im\tilde{u}\right] \tag{2.74}$$

$$\left(r^2\sigma + imrV\right)\tilde{w} = -ikr^2\tilde{p} + \frac{1}{Re}\left[r\partial_r\left(r\partial_r\tilde{w}\right) - (m^2 + k^2r^2)\tilde{w}\right] \tag{2.75}$$

These equations can be expressed in matrix format $\mathcal{A}\tilde{\boldsymbol{u}} = \sigma\mathcal{B}\tilde{\boldsymbol{u}}$ with:

$$\mathcal{A} = \begin{pmatrix} -imrV + D - \nu & 2rV - 2i\nu m & 0 & -r^2\partial_r \\ -r^2\partial_r V - rV + 2i\nu m & -imrV + D - \nu & 0 & -imr \\ 0 & 0 & -imrV + D & -ikr^2 \\ r\partial_r + 1 & im & ikr & 0 \end{pmatrix} \tag{2.76}$$

D is the viscous diffusion: $D = \nu\left[r\left(\partial_r + r\partial_r^2\right) - \left(m^2 + k^2r^2\right)\right]$

$$\mathcal{B} = \begin{pmatrix} r^2 & 0 & 0 & 0 \\ 0 & r^2 & 0 & 0 \\ 0 & 0 & r^2 & 0 \\ 0 & 0 & 0 & 0 \end{pmatrix} \tag{2.77}$$

$\mathcal{B}$ is the mass matrix. Adjoint modes can be similarly defined using the adjoint Navier-Stokes equations: $\mathcal{A}^+\tilde{\boldsymbol{u}}^+ = \sigma^+\mathcal{B}\tilde{\boldsymbol{u}}^+$ with

$$\mathcal{A}^+ = \begin{pmatrix} imrV + D - \nu & -r^2\partial_r V - rV - 2i\nu m & 0 & -r^2\partial_r \\ 2rV + 2i\nu m & imrV + D - \nu & 0 & -imr \\ 0 & 0 & imrV + D & -ikr^2 \\ r\partial_r + 1 & im & ikr & 0 \end{pmatrix} \tag{2.78}$$

σ^+ is the adjoint complex frequency such that $\sigma^+ = \sigma^*$. The adjoint is defined with the scalar product $(\boldsymbol{w}, \boldsymbol{u}) = \int \boldsymbol{w}^H\boldsymbol{u}rdr = \boldsymbol{w}^H\mathcal{N}\boldsymbol{u}$ where ^{H} denotes the Hermitian conjugate, with

$$\mathcal{N} = \begin{pmatrix} r & 0 & 0 & 0 \\ 0 & r & 0 & 0 \\ 0 & 0 & r & 0 \\ 0 & 0 & 0 & 0 \end{pmatrix} \tag{2.79}$$

The direct and adjoint modes are normalised as follows:

$$\begin{cases} (\boldsymbol{w}_i, \boldsymbol{u}_j) = \delta_{ij} \\ (\boldsymbol{u}_i, \boldsymbol{u}_i) = 1 \end{cases} \tag{2.80}$$

The result of the adjoint simulation based on $\mathcal{B}$ needs to be mapped to the scalar product based on $\mathcal{N}$ rather than $\mathcal{B}$. Formally this is obtained by writing $\boldsymbol{w}_i^H \mathcal{N} \mathcal{B}^{-1} \mathcal{B} \boldsymbol{u}_i = 1 = (\mathcal{B}^{-1} \mathcal{N} \boldsymbol{w}_i)^H \mathcal{B} \boldsymbol{u}_i$. Upon identifying the $\mathcal{B}$-based adjoint $\bar{\boldsymbol{w}}_i = \mathcal{B}^{-1} \mathcal{N} \boldsymbol{w}_i$, the $\mathcal{N}$-based adjoint is obtained from the $\mathcal{B}$-based adjoint by applying $\boldsymbol{w}_i = \mathcal{N}^{-1} \mathcal{B} \bar{\boldsymbol{w}}_i$.

2.3.4 Problem resolution

The problem to resolve is: $\mathcal{B} \partial_t \tilde{\boldsymbol{u}} = \mathcal{A} \tilde{\boldsymbol{u}}$. Using the time discretisation the equation becomes:

$$\mathcal{B} \frac{3\tilde{\boldsymbol{u}}_{n+1} - 4\tilde{\boldsymbol{u}}_n + \tilde{\boldsymbol{u}}_{n-1}}{2\Delta t} = \mathcal{A} \tilde{\boldsymbol{u}}_{n+1} \tag{2.81}$$

The solution at time t_{n+1} is therefore:

$$\tilde{\boldsymbol{u}}_{n+1} = \left(3\mathcal{B} - 2\Delta t \mathcal{A}\right)^{-1} \mathcal{B} \left(4\tilde{\boldsymbol{u}}_n - \tilde{\boldsymbol{u}}_{n-1}\right) \tag{2.82}$$

The same reasoning can be used for the adjoint equations. Finally, as for the optimisation tool described in 2.2 an iterative direct-adjoint process is put in place. The update of the initial perturbation is achieved using the optimality equations: the steepest ascent direction is set to zero. The initial perturbation guess is white noise.

2.3.5 Validation of the Finite Element optimisation tool

The Finite Element (FE) optimisation tool was validated by comparing results with linear optimal work such as Antkowiak & Brancher [2, 3] and Pradeep & Hussain [80]. These results are provided in Chapter 6. In addition all linear optimisation results obtained with the Nek5000 tool were corroborated with results from the FE tool.

Chapter 3

Nonlinear response to the linear optimal perturbation

This chapter is dedicated to the study of the nonlinear dynamics that ensue from the linear optimal perturbation of a vortex pair at finite initial amplitude. The contents form a self-contained article published in the *Journal of Fluid Mechanics* [50]. The linear optimal perturbation or adjoint mode of the Crow instability is superimposed with varying initial amplitude on a base flow composed of a counter-rotating pair of vortices. The work presented in this chapter was performed using HPC resources from GENCI-IDRIS (grant 2014-i20142a7323).

Abstract

The potential for anticipated destruction of a counter-rotating vortex pair using the linear optimal perturbation of the Crow instability is assessed. Direct Numerical Simulation is used to study the development of the Crow instability and the subsequent evolution of the flow up to 30 characteristic times at a circulation-based Reynolds number of 1000. The conventional development of the instability leads to multiple contortions of the vortices including the linear growth of sinusoidal deformation, vortex linking and the formation of vortex rings. A new evolution stage is identified, succeeding this well-established sequence: the vortex rings undergo periodic oscillation. Two complete periods are simulated during which the vortical system is hardly altered, thereby demonstrating the extraordinary resilience of the vortices. The possibility of preventing these dynamics using the linear optimal perturbation of the Crow instability, the adjoint mode, is analysed. By appropriately setting the forcing amplitude, the lifetime of the vortices until their loss of coherence is reduced to approximately 13 characteristic times, which is less than half that of the natural Crow behaviour observed with infinitesimal forcing. The dynamics of the flow induced by the linear optimal perturbation that enable this result are connected to processes already known to efficiently alter vortical flows, in particular transient growth and four-vortex dynamics.

3.1 Introduction

The increasing demand for air transport across the world has led to saturation in many major airports. Take-off and landing rhythms are limited by a safety interval imposed to avoid the danger of encountering an aircraft wake. Taking the form of a counter-rotating vortex pair, this powerful wake generates a rotating force that could tip a following aircraft. This danger is also encountered at cruising level and

represents a major concern for air traffic control. Understanding and controlling these coherent structures is therefore of paramount importance and has been the subject of many studies for several decades.

The optimal perturbation is the perturbation that generates maximum growth of perturbation energy over a certain period of time and therefore constitutes the ideal perturbation for disrupting a flow. Many optimal perturbation studies have been carried out on various flow configurations. In the case of an isolated vortex, Antkowiak & Brancher [2] and more recently Pradeep & Hussain [80] determined the linear optimal perturbations for azimuthal wavenumbers $m = 1$ and $m = 1...4$ respectively. In particular the $m = 1$ mode with wavenumber $ka = 1.4$ leads to significant transient growth in this otherwise linearly stable flow. Farrell [36] established that the linear optimal perturbation of a particular flow corresponds to the adjoint of the most unstable mode of the flow. Brion et al. [15] applied this principle to a counter-rotating vortex pair. The dominant instability of this configuration is the Crow instability [21] which induces symmetrical sinusoidal displacement of the vortex cores. The linear optimal perturbation corresponding to the Crow instability established by Brion et al. [15] takes the form of vorticity sheets concentrated close to the plane separating the two vortices and produces considerable transient growth before reaching the classic linear Crow instability behaviour.

It has been shown that when an isolated vortex is subjected to external perturbation, secondary helical structures form, wrapping around the core in a manner that is very similar to that of the linear optimal. Melander & Hussain [71], Miyazaki & Hunt [74] and Marshall & Beninati [67] studied the reaction of a vortex to fine-scale turbulence using DNS, and Fontane et al. [39] continuously stimulated a vortex using stochastic forcing. In all of these studies the emergence of the linear optimal was observed. Whatever the form of the perturbation, the modes corresponding to the linear optimal are preferentially excited through the interaction with the vortex. Although the initial perturbation development is linear, once secondary structures are formed it is possible they will interact and the subsequent evolution will be nonlinear. It is therefore legitimate to pose the question, what happens to linear optimal perturbations when the nonlinearities become non-negligible. Another point of importance is that of the effect of a finite initial amplitude of the optimal perturbation and how it would influence the evolution of the flow. Such questions cannot be answered in a linear framework and become important when the practicality of the approach is questioned. It should be noted that the feasability of the linear optimal perturbation of the Crow instability occurring or being generated in a real vortex system is not addressed in this study which remains at the theoretical level, but this should be approached at a later stage.

The method used in this paper, initialising a nonlinear DNS with the linear optimal mode, has been applied in previous works. Hussain et al. [46] studied the nonlinear evolution of the linear optimal mode of an isolated vortex and observed that moderate initial perturbation amplitudes at a high enough Reynolds number could trigger core transition. Schaeffer & Le Dizès [86] studied the nonlinear evolution of the elliptic instability on a single strained vortex and a pair of counter-rotating vortices. Schmid & Henningson [87] showed that the linear optimal perturbation with finite initial amplitudes can generate laminar-turbulent transition in normal-mode stable shear flows.

The aim of this paper is to study the nonlinear response to the linear optimal perturbation of a counter-rotating vortex pair determined by Brion et al. [15] using Direct Numerical Simulation. The paper is organised in the following manner. The methods used to carry out the DNS and to obtain the linear perturbation mode are outlined (§ 3.2). A preliminary study of the long-term behaviour of the Crow instability with infinitesimal initial amplitude is carried out to provide a reference for the following analysis (§ 3.3). The nonlinear response to the linear optimal perturbation introduced with growing initial amplitudes is then studied and compared with the reference case (§ 3.4). Finally the physical mechanisms involved in the accelerated decay of the vortex pair are described (§ 3.5).

3.2 Governing equations

The flow is governed by the incompressible Navier-Stokes equations, shown below.

$$\boldsymbol{\nabla}\cdot\boldsymbol{u} = 0 \tag{3.1}$$

$$\partial_t \boldsymbol{u} + (\boldsymbol{u}\cdot\boldsymbol{\nabla})\,\boldsymbol{u} = -\boldsymbol{\nabla}p + \nu\boldsymbol{\nabla}^2\boldsymbol{u} \tag{3.2}$$

Decomposing the velocity and pressure of the flow into components corresponding to the base flow and to a small perturbation, $\boldsymbol{u} = \boldsymbol{U} + \epsilon\boldsymbol{u'}$, $p = P + \epsilon p'$ with $\epsilon \ll 1$ and linearising the equations around the base flow yields the linearised Navier-Stokes equations given here at first order of ϵ.

$$\boldsymbol{\nabla}\cdot\boldsymbol{u'} = 0 \tag{3.3}$$

$$\partial_t \boldsymbol{u'} + (\boldsymbol{u'}\cdot\boldsymbol{\nabla})\,\boldsymbol{U} + (\boldsymbol{U}\cdot\boldsymbol{\nabla})\,\boldsymbol{u'} = -\boldsymbol{\nabla}p' + \nu\boldsymbol{\nabla}^2\boldsymbol{u'} \tag{3.4}$$

The base flow of the simulation is composed of a pair of counter-rotating Lamb-Oseen vortices, with initial azimuthal velocity U_θ defined as:

$$U_\theta(r) = \frac{\Gamma}{2\pi r}\left(1 - e^{-\frac{r^2}{a^2}}\right) \tag{3.5}$$

with Γ the circulation of the vortex.

All results are rendered non-dimensional by the initial distance separating the vortices b and the drift velocity of the vortex pair through mutual induction $U_{drift} = \Gamma/2\pi b$. The characteristic evolution time of the dipole is the time it takes to descend a distance equal to b through mutual induction, $\tau = b/U_{drift} = 2\pi b^2/\Gamma$. The resulting Reynolds number is $Re = \Gamma/2\pi\nu$ with ν the kinematic viscosity of the fluid. In this case, the Reynolds number is taken to be $Re = 1000$ and the initial aspect ratio of the vortex pair is $a/b = 0.18$. In order to avoid the transient phase due to the adaptation of the Lamb-Oseen vortex pair to the Navier-Stokes equations, the base flow is time-stepped forward by several reference times ($t \approx 8$) before embarking on the perturbation analysis. The details of this method are described by [88]. During the linear simulations to obtain the linear optimal perturbation the base flow is "frozen". This is valid as long as the viscous timescale is large compared with the timescale of the perturbation dynamics. The timescale of the viscous diffusion of a vortex being $t_\nu = 2\pi a^2/\nu$, the ratio of these two timescales $t_\nu/\tau = (a/b)^2\, Re$ is indeed large.

As the wavelength of the most unstable Crow mode is around $\lambda_z = 7b$, the simulations are carried out on a mesh of extent $[-L_x/2, L_x/2] \times [-L_y/2, L_y/2] \times [-L_z/2, L_z/2]$ with $L_x = 9.6b$, $L_y = 10.8b$, $L_z = 7b$ in order to calculate one complete wavelength of the instability. Cartesian coordinates (x, y, z) are used throughout the study. The largest divisions in each direction are $\Delta x_{max}/b \approx 0.025$, $\Delta y_{max}/b \approx 0.03$, $\Delta z_{max}/b \approx 0.02$. The Direct Numerical Simulation is carried out using the incompressible Navier-Stokes solver Nek5000 [38], which is based on a spectral elements method. The computational domain is split into N_e^3 uniformly distributed elements with $N_e = 70$, containing $N_{GLL} = 8$ Gauss-Lobatto-Legendre (GLL) points in each direction. The largest mesh interval is given by $\Delta d_{max} = \pi L_d/2\,(N_{GLL} - 1)\,N_e$ with $d \in x, y, z$.

Although the flow studied in this paper is initially laminar, the nature of the resulting dynamics is unknown and potentially turbulent. Therefore it is judicious to create a mesh that can handle a turbulent flow calculation were it to materialise. The mesh must be fine enough to capture the Kolmogorov dissipation scale $\lambda_{Kolm} = Re^{-3/4}b \approx 6.10^{-3}$ and the shear layer scale at the leading hyperbolic point $\delta = \left(2\pi b^2\nu/3^{1/2}\Gamma\right)^{1/2} \approx 2.5.10^{-2}$ determined here for a point vortex model. The contribution of eddies of scale $l \leq 5\lambda_{Kolm}$ is negligible [79], and therefore the current mesh, designed on this threshold, is sufficient. As confirmation a test was carried out using half the number of elements for the same domain size, which

gave close to identical results, with less than 3% difference between the values of the circulation at $t = 10$. Similarly the adequacy of the domain size was validated using a mesh twice as large, keeping the same number of elements and GLL points. Boundary conditions in the axial direction (z) are periodic. In order to compensate for the descent of the vortex pair through mutual induction a vertical velocity is imposed in the domain. Therefore the boundary conditions on the negative and positive y-borders are inflow and outflow respectively. Finally in the spanwise direction symmetrical conditions are imposed.

Farrell [36] demonstrated that the linear optimal perturbation of a flow is the adjoint of the most unstable mode of the flow. The adjoint of the most unstable Crow mode is determined by solving the adjoint linearised Navier-Stokes equations. The adjoint $\tilde{A}$ of an operator A is defined as $(x, Ay) = (\tilde{A}x, y) + b.c.$ with x and y vectors, $(\cdot, \cdot)$ the scalar product and $b.c.$ meaning boundary conditions. Applying this definition to the operator corresponding to the linearised Navier-Stokes equations gives the adjoint equations:

$$\boldsymbol{\nabla \cdot \tilde{u}'} = 0 \tag{3.6}$$

$$\partial_t \boldsymbol{\tilde{u}'} + (\boldsymbol{\tilde{u}' \cdot \nabla})\, \boldsymbol{U} - (\boldsymbol{U \cdot \nabla})\, \boldsymbol{\tilde{u}'} = -\boldsymbol{\nabla} \tilde{p}' + \nu \boldsymbol{\nabla}^2 \boldsymbol{\tilde{u}'} \tag{3.7}$$

The initial velocity field for each DNS simulation described in this paper is expressed as $\boldsymbol{u}_\epsilon(0) = \boldsymbol{U} + \epsilon ||\boldsymbol{U}|| \boldsymbol{u'_0}$ with $\boldsymbol{u'_0}$ the normalised perturbation velocity field (the adjoint Crow mode is taken here). Once started the simulation yields the flow field $\boldsymbol{u_\epsilon}(t)$. In contrast to the linear simulations throughout which the base flow was frozen, the nonlinear simulation implicates an evolving base flow. In the linear stage of the evolution the pertubation $\boldsymbol{u'}(t)$ can be retrieved by the following approximation $\boldsymbol{u_\epsilon}(t) \simeq \boldsymbol{u_{\epsilon=0}}(t) + \epsilon ||\boldsymbol{U}|| \boldsymbol{u'}(t)$. Therefore an unperturbed flow ($\epsilon = 0$) is required in order to follow the evolution of the perturbation $\boldsymbol{u'}(t)$ and the perturbation kinetic energy $E'(t) = ||\boldsymbol{u'}(t)||^2$ can then be computed as:

$$E'(t) = \epsilon^{-2} ||\boldsymbol{U}||^{-2} ||\boldsymbol{u_\epsilon}(t) - \boldsymbol{u_{\epsilon=0}}(t)||^2 \tag{3.8}$$

3.3 Reference case: Response to infinitesimal forcing of the linear optimal perturbation

The reference case for the nonlinear dynamics of the Crow instability is established for an infinitesimal initial perturbation amplitude to get as close to the linear limit as possible ($\epsilon \to 0$). This case can be assimilated to the far-field wake of an aircraft in very calm and homogeneous atmospheric conditions. The linear optimal perturbation is superimposed on the base flow with an initial amplitude $\epsilon = 10^{-3}$. It is important to note that at such a small initial amplitude, the overall dynamics will be the same as if the flow was initialised with the most unstable Crow mode. The use of the linear optimal perturbation here has only one objective: accelerating the development of the instability to limit simulation time costs.

The dynamics of the vortex pair is concurrent with that described by Crow [21]. Iso-vorticity contours illustrate the dynamics in figure 3.1. As the simulations are carried out over one wavelength of the Crow instability, only one wavelength is shown. The vortices undergo a gradual symmetrical sinusoidal deformation with the cores remaining in a plane of angle equal to approximately 45^o with respect to the span-wise direction (x). Eventually at time $t = 9$ the closest parts of the vortices meet and are pressed together. The descent of the dipole and the continued deformation of the vortices creates a distinctive head-tail dipole shape in the connection z-planes. Vorticity cancellation between the opposite signed vortices becomes very strong in these areas, and the linking phenomenon is observed. This well-known occurrence is described in more detail in the following paragraph. Once linking is complete, the vortices form a chain of vortex rings connected by thin vorticity threads. Due to the original symmetrical

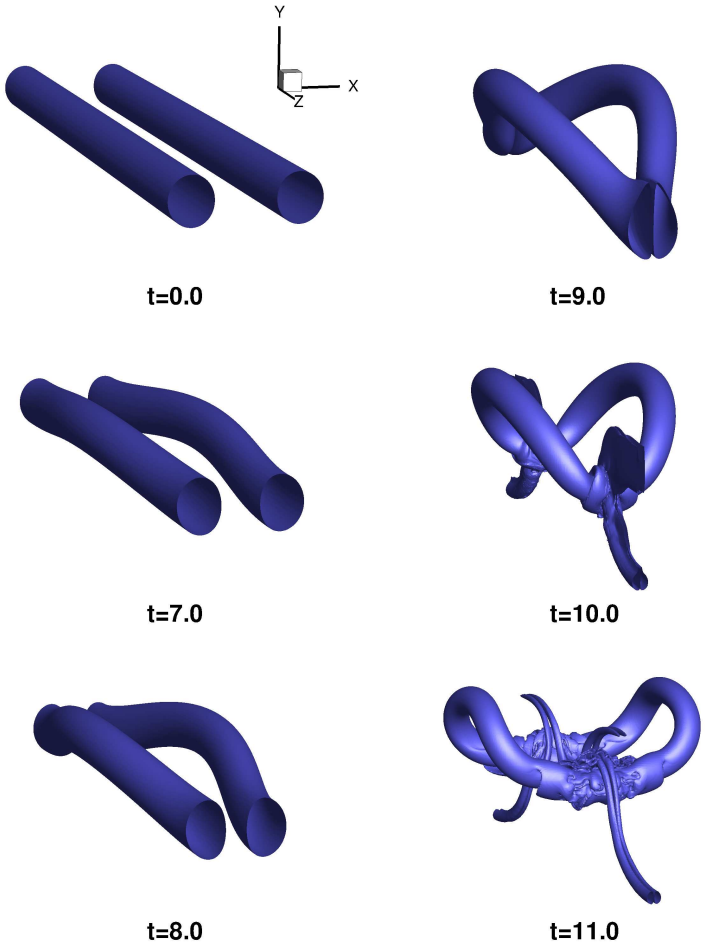

Figure 3.1: Iso-vorticity contours at 20% of the initial maximum of vorticity $\omega = 0.2|\omega_{max}(t=0)|$ showing the initial development of the Crow instability and the linking of the vortices.

deformation of the vortices, the sides of the rings remain curved upwards, as can be observed at $t = 11$.

Over recent years much attention has been paid to vortex linking because of its supposed involvement in turbulence cascade and turbulent noise generation. In spite of a great number of analytical, numerical and experimental studies, some aspects of this complicated process are still unclear. Saffman [84] developed a model describing the linking of two counter-rotating vortices and Moriconi [75] extended the model into high Reynolds numbers. Detailed decriptions of the physical mechanisms at play are given by many authors [45, 68, 70]. To summarise quickly, when the vortices touch, viscous diffusion causes the touching parts to cancel each other out. The remaining strands on the outer sides of the vortex cores then pair up to form bridges connecting the two vortices. These bridges become strong and move away from each other through self-induction, leaving behind the remnants of the original vortices in threads. The linking of the vortex pair into vortex rings can be observed particularly well when studying the evolution of the axial circulation γ_z in the connection z-plane ($z = \pm L_z/2$) and the span-wise circulation γ_x in the symmetry plane ($x = 0$) , as can be seen in figure 3.2. These circulations are defined by the following expressions:

$$\gamma_z = \int_0^{L_x/2} \int_{-L_y/2}^{L_y/2} \omega_z\left(x, y, L_z/2\right) dxdy \tag{3.9}$$

$$\gamma_x = \int_{-L_y/2}^{L_y/2} \int_0^{L_z/2} \omega_x\left(0, y, z\right) dydz \tag{3.10}$$

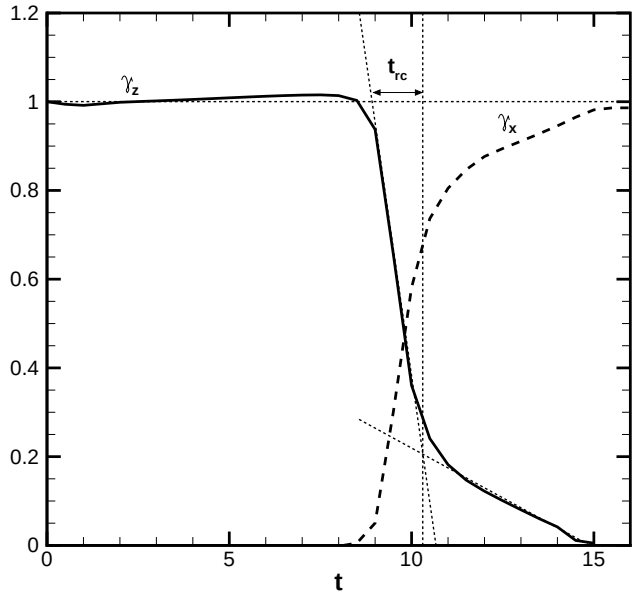

Figure 3.2: Evolutions of the circulation γ_z in the connection plane ($z = L_z/2$) and the circulation γ_x in the dividing plane ($x = 0$) . Evidence of the transfer of axial vorticity to spanwise vorticity throughout the linking process.

with ω_x and ω_z the x- and z-components of the vorticity vector respectively. Vorticity cancellation between the colliding counter-rotating vortices leads to a dramatic drop of the axial circulation γ_z from $t = 8$ to $t = 10$. At this point the threads linking the vortex rings are still present and so the decrease of the axial circulation slows before finally reaching almost zero at around $t = 13.5$. From this point the axial circulation is nil, demonstrating that once the vortex rings are formed and the threads have disappeared, no axial vorticity exists in the ($z = L_z/2$)-plane. The span-wise circulation γ_x is negligible initially but from $t = 8$ increases rapidly, eventually attaining 98% of the initial value of γ_z. The evolution of these quantities demonstrates the transfer of vorticity from the axial direction to the span-wise direction. Of the numerous ways to characterise this phenomenon, one of the most striking is the connection time t_{rc}. This corresponds to the duration between the vortex cores touching and the bridges separating. From pure observation of the connection progress, it is virtually impossible to determine a definitive connection time value. However Melander & Hussain [70] and Leweke & Williamson [60] noted that it is possible to deduce a value by inspecting the evolution of the circulation in the connection plane. Using the same method, illustrated in figure 3.2, the linking time in this case is found to be equal to $t_{rc} = 1.5 \pm 0.2$ compared with $t_{rc} = 0.7 \pm 0.1$ for [70] at $Re = \Gamma/\nu = 1000$ and $t_{rc} = 0.9 \pm 0.2$ for [60] for $Re = \Gamma/\nu = 2340$. The error estimation of this type of method is around 15% to 20%. The disparity between the connection time found here and those established in other papers is most certainly due to the difference in Reynolds number and the difference in axial perturbation wavelength. Although the aspect ratios used are very similar ($a/b = 0.18$ for Leweke & Williamson and $a/b = 0.22$ for Melander & Hussain) the axial wavelengths chosen for the deformation of the vortex pair are quite different: $\lambda_z/b = 5.13$ for Leweke & Williamson and $\lambda_z/b = 3.85$ for Melander & Hussain (as opposed to $\lambda_z/b = 7$ in the present study).

The subsequent evolution of the flow is analysed in the light of several quantities, namely the length-averaged axial circulation $\Gamma_z(t)$ and spanwise circulation $\Gamma_x(t)$ which indicate the strength of the vortices, the enstrophy $\xi(t)$ and the total kinetic energy $E(t)$. These quantites are expressed as integrals over the

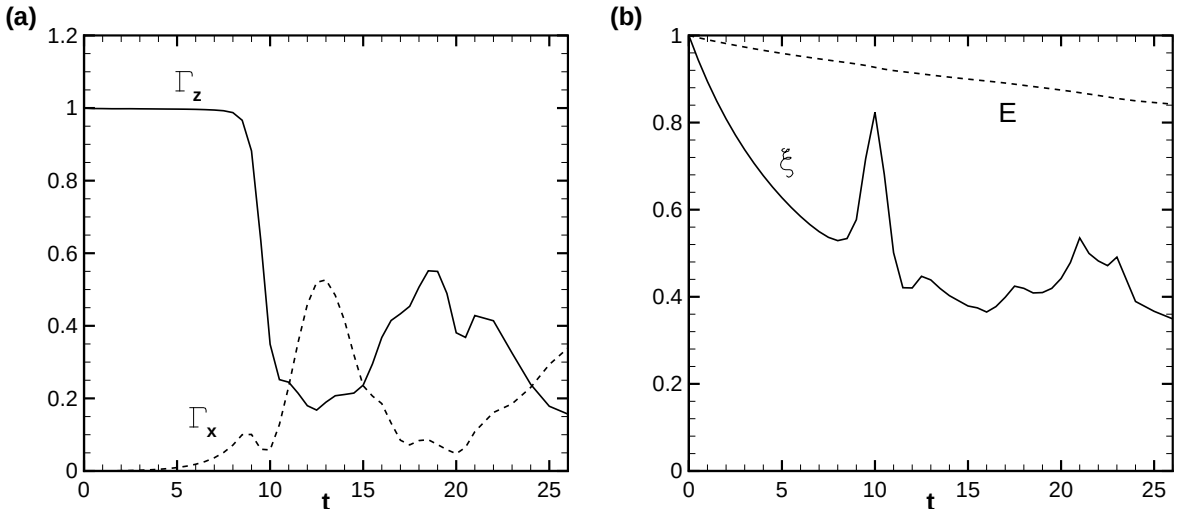

Figure 3.3: (a) Evolution of length-averaged axial and spanwise circulations Γ_z and Γ_x over time. (b) Total kinetic energy E and enstrophy ξ evolution over time. Note the kinetic energy and enstrophy were integrated over the whole domain whereas the circulations were integrated over half of the domain.

computational volume V:

$$\Gamma_z(t) = \frac{1}{L_z}\int_V \omega_z(t)\,dV \tag{3.11}$$

$$\Gamma_x(t) = \frac{1}{L_x}\int_V \omega_x(t)\,dV \tag{3.12}$$

$$\xi(t) = \frac{1}{2}\int_V \boldsymbol{\omega}(t)^2\,dV \tag{3.13}$$

$$E(t) = \frac{1}{2}\int_V \boldsymbol{u}(t)^2\,dV \tag{3.14}$$

Figures 3.3(a) and 3.3(b) show the evolution of these quantities in time. The evolution of the length-averaged circulations highlights the exchange of circulation between the axial and spanwise directions at the linking stage, and then again at $t = 15$ and $t = 24$. After linking, the maximum of length-averaged circulation $max(\Gamma_x, \Gamma_z)$ remains at around 60% of the initial value of Γ_z and is attained at $t \approx 13$ by Γ_x and $t \approx 19$ by Γ_z. This demonstrates the existence of a periodic behaviour that will be analysed further by observing the dynamics of the vortex rings in the following paragraphs. The nature of the flow can be examined by considering the evolution of the enstrophy ξ. The progression in time of the enstrophy is governed by the equation:

$$\frac{\partial \xi}{\partial t} + (\boldsymbol{u}\cdot\boldsymbol{\nabla})\,\xi - \nu\nabla^2\xi = S_{\omega\omega}\xi - \nu\boldsymbol{\nabla\omega} : \boldsymbol{\nabla\omega} \tag{3.15}$$

with $S_{\omega\omega} = 2[(\boldsymbol{n}_\omega \cdot \nabla)\,\boldsymbol{u}] \cdot \boldsymbol{n}_\omega$ the component of strain in the vorticity direction and $\boldsymbol{n}_\omega = \frac{\boldsymbol{\omega}}{\|\boldsymbol{\omega}\|}$. The left hand side of the equation constitutes the advection-diffusion term, the first term of the right hand side is the production term, and the last term ensures viscous dissipation. Production of enstrophy occurs through the stretching of vorticity. During the first stage of the evolution of the vortices, before the connection, the enstrophy decreases rapidly which can be anticipated in the case of a laminar flow. At $t = 10$ the linking process entails massive vorticity stretching which generates a large spike of enstrophy. The subsequent enstrophy peaks are due to the stretching of smaller structures formed around the vortex ring. Finally the kinetic energy of the flow decreases steadily over time as a consequence of viscous dissipation. This behaviour can be expected from a laminar viscous flow.

At the end of the linking process $t = 11$, the vortex rings produced are circular and the sides corresponding to the original straight vortices are curved upwards as a result of the Crow instability (see figure 3.1). Self-induced vorticity due to the curvature of the vortex draws these sides outwards (in the spanwise direction) until the ring is flat. The resulting rings are then elliptic with the major axis aligned in the spanwise direction. The dynamics of an elliptic vortex ring have been studied analytically by Arms & Hama [6]. Using the Biot-Savart law and adopting a localised-induction theory Arms & Hama established several principles that regulate the dynamics of elliptic vortex rings. They concluded that elliptic vortex rings experience periodic deformations, where the major and minor axes periodically exchange their orientations. The period T of this behaviour depends on the eccentricity $e = \sqrt{1 - l^2/L^2}$ of the original ellipse, where L is the length of the semi-major axis and l the length of the semi-minor axis. The greater the eccentricity, the more complex is the deformation. These results were validated numerically and experimentally by Dhanak & Bernardinis [25].

An estimation for the initial eccentricity in this case is $e \approx 0.97$ with an axis ratio $l/L \approx 0.26$. The different stages of evolution of the vortex rings, illustrated in figure 3.4 with vorticity norm isocontours, are very similar to those described by [6] and [25], in particular the "figure-of-eight" shape attained at the half-period $T/2$ (here at $t = 19$). The cores are very close in the centre of the domain at this time, but they do not touch enough for linking to occur and the deformation continues. Had the cores touched at this point, viscous diffusion would certainly have lead to the annihilation of vorticity between the parts of opposing sign and the vortices would have split once more into two smaller vortex rings. It is conceivable that another Crow wavelength, generating a different eccentricity, could lead to such a scenario. At time T the resulting ring is an ellipse of similar size and shape to the original ellipse.

By observing the movement of the vortex ring, the deformation period is estimated to be $T = 13$. Two complete periods are captured by the present simulation although only one is shown in figure 3.3. Using the expression of Arms & Hama [6] derived by linearised analysis of a circular vortex ring and adapted to account for the eccentricity of the elliptic ring, the theoretical period of oscillation is $T_{th} = 10.4$, providing reasonable agreement with the simulated value. Such discrepancies between theory and simulation were also observed by Arms & Hama: typically a 6% difference for $e = 0.94$ and larger for increased eccentricity.

This behaviour of vortex rings issued from the linking of a vortex pair was observed experimentally by Leweke & Williamson [60]. They observed the successive deformations characteristic of elliptic vortex rings over less than a period, and in some cases a second reconnection of the vortex rings into longer ellipses resembling the initial straight vortices. The simulated results of this paper confirm the initial development described by Leweke & Williamson (stages A to E in their figure 14) but the second reconnection of the vortices is not retrieved.

These results indicate that when subjected to infinitesimal forcing, a pair of counter-rotating vortices go through multiple evolutions without losing much coherence over more than twenty-five characteristic times. Loss of coherence could not be reached in the simulated time frame meaning that in calm atmospheric conditions aircraft wakes may be present for durations longer than those required for vortex linking.

3.4 Nonlinear response to the linear optimal perturbation

In this section the nonlinear response to the linear optimal perturbation is analysed by a parametric study based on the initial perturbation amplitude ϵ. Figure 3.5 shows the perturbation energy growth $G(t)$ over time for two example values of ϵ as well as the infinitesimal case $\epsilon = 10^{-3}$ and the equivalent growths for the Crow eigenmode and linear optimal perturbation as outlined by Brion et al. [15]. The

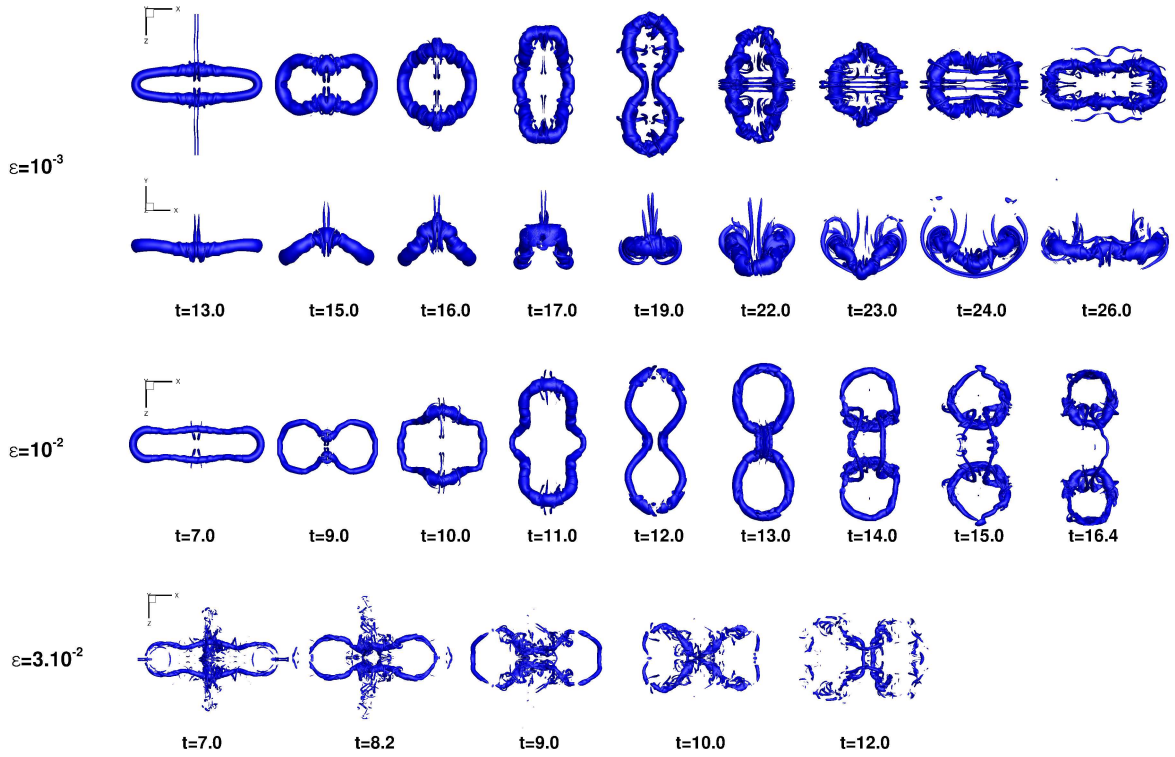

Figure 3.4: Vorticity isocontours at 14% of the initial vorticity norm maximum $\omega = 0.14|\omega_{max}(t=0)|$ for $\epsilon = 10^{-3}$ and 20% of the initial vorticity norm maximum $\omega = 0.14|\omega_{max}(t=0)|$ for $\epsilon = 10^{-2}$ and $\epsilon = 3.10^{-2}$, evolution of the vortex rings during the first period T. View from above and the front for each stage of the $\epsilon = 10^{-3}$ case, view from above only for $\epsilon = 10^{-2}$ and $\epsilon = 3.10^{-2}$.

perturbation energy growth is defined as follows:

$$G(t) = \frac{E'(t)}{E'(0)} \tag{3.16}$$

with E' the perturbation kinetic energy defined at (3.8). First note that all the perturbation energy growths initially follow the linear behaviour and then branch off, signalling at that moment the beginning of nonlinear behaviour. The recording of the perturbation energy growth is halted soon after the divergence from the linear behaviour as from that time the definition of the perturbation kinetic energy (3.8) is no longer valid. In the case of infinitesimal initial amplitude $\epsilon = 10^{-3}$ this occurs at $t \approx 8$ which coincides with the start of vortex linking, the first nonlinear event to occur. Increasing the initial amplitude simply shifts this scenario in time and generates the vortex linking sooner. However, for $\epsilon = 3.10^{-2}$ the deviation from the linear behaviour occurs before the exponential perturbation energy growth characteristic of the Crow instability is even established. Therefore a critical amplitude ϵ_c which distinguishes two behaviours can be defined such that $10^{-2} < \epsilon_c < 3.10^{-2}$. For $\epsilon < \epsilon_c$ the Crow instability is reached before nonlinear effects come into play, whereas for $\epsilon > \epsilon_c$ nonlinear dynamics start during the initial transient growth due to the linear optimal perturbation.

An efficient way to measure the impact of nonlinear phenomena in an initially purely harmonic flow is to look at its wavelength composition. In the case of an infinitesimal perturbation, only the wavelength corresponding to the perturbation will experience growth over time. This is demonstrated in figure 3.6(a) which gives the volume averaged energy spectrum of the $\epsilon = 10^{-3}$ and $\epsilon = 3.10^{-2}$ cases at $t = 3$. For $\epsilon = 10^{-3}$ the majority of the energy is concentrated at wavenumber $kb = 0.9$ (the first peak in the spectrum) which corresponds to the wavelength of the initial perturbation (and that of the

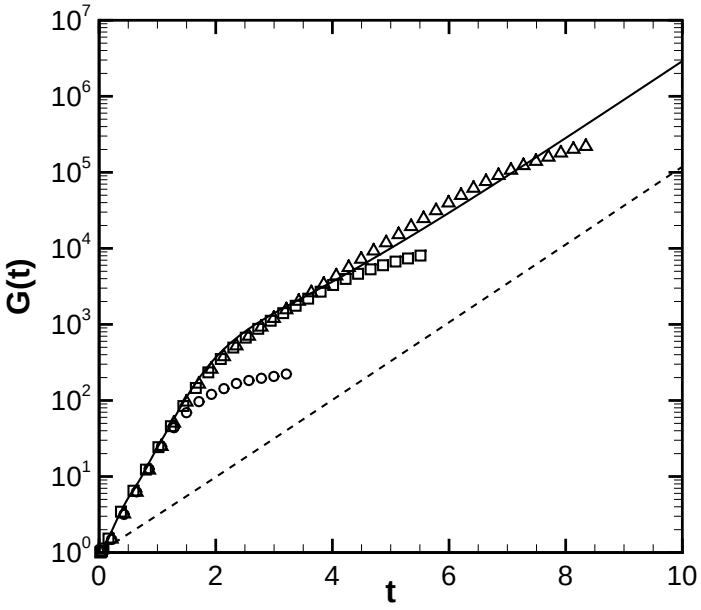

Figure 3.5: Perturbation energy growth rates for the linear evolution of the Crow instability eigenmode (dashed line) and the linear optimal perturbation (solid line), as well as those obtained for the evolution of the linear optimal perturbation initialised with $\epsilon = 10^{-3}$ (triangles), $\epsilon = 10^{-2}$ (squares) and $\epsilon = 3.10^{-2}$ (circles).

computational domain). However as soon as the perturbation reaches sufficient amplitude, interactions of the perturbation with itself produce smaller scales, thus widening the spectrum, as can be seen for $\epsilon = 3.10^{-2}$. Here the Crow wavenumber $kb = 0.9$ is less amplified compared with the infinitesimal case. A gain of around 100 is obtained for $\epsilon = 3.10^{-2}$ as opposed to about 2700 for $\epsilon = 10^{-3}$ as can also be seen in figure 3.5. Note that such important gains, which are much larger than those permitted by the Crow amplification, are made possible by the use of the adjoint mode as the initial perturbation.

The impact of the initial amplitude ϵ is analysed with the width of the energy spectrum Δk in the axial (z) direction, defined as:

$$\Delta k = \frac{\int kE\,(k)\,dk}{\int E\,(k)\,dk} \tag{3.17}$$

with $E\,(k)$ the total kinetic energy of the flow at the wavenumber k. Figure 3.6 (b) shows the resulting spectrum widths for varying ϵ for $t = 1$ to 3. Only a few values of ϵ have been tested but they are sufficient to draw the conclusion that over a certain limit the nonlinear behaviour induced by the linear optimal perturbation is drastically different and leads to a rapid development of smaller-scale structures. The time $t = 3$ is particularly interesting because at that time (see figure 3.5) either exponential Crow growth has been reached ($\epsilon < \epsilon_c$) or nonlinear behaviour has taken place ($\epsilon > \epsilon_c$).

Next, the effect of the initial amplitude on the length-averaged axial circulation, the enstrophy and kinetic energy is evaluated. Figure 3.7 gives the evolutions of these quantities through time for $\epsilon = 10^{-2}$ and $\epsilon = 3.10^{-2}$ as well as $\epsilon = 10^{-3}$ for comparison.

The evolution of the length-averaged axial circulation Γ_z of the two simulations - see figure 3.7 (a) - shows that raising the initial perturbation amplitude accelerates the displacement of the vortices and anticipates linking. For $\epsilon = 10^{-2}$ the same periodic evolution of the circulation as in the infinitesimal case can be observed after the drop due to connection. The vorticity iso-contours of figure 3.4 confirm this behaviour. The elliptic ring shape is attained at around $t = 7$ and the deformation of the ring is the same as in the infinitesimal case. However there is a major difference at later times: after the

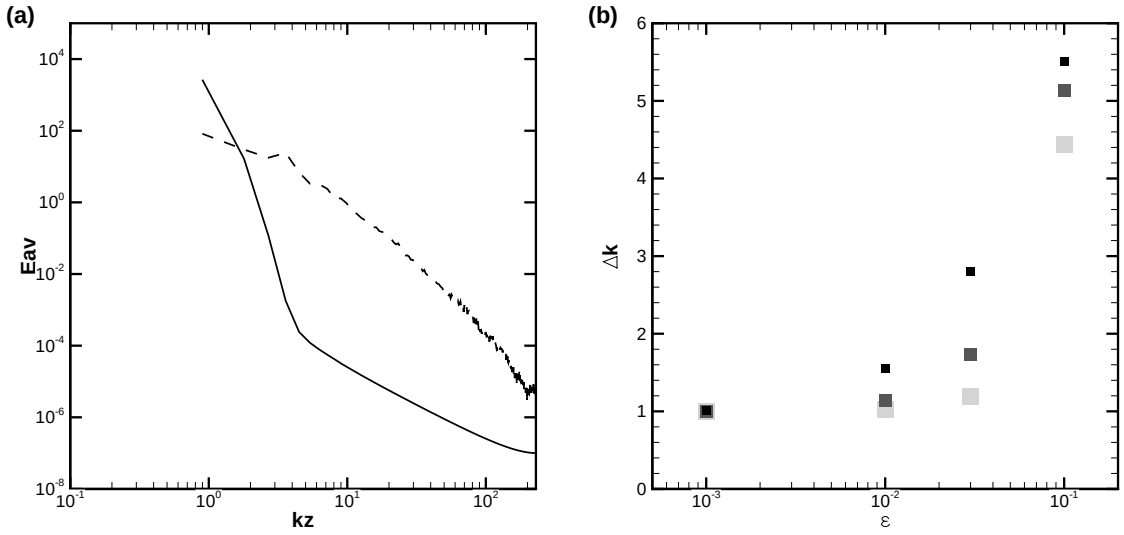

Figure 3.6: (a) Kinetic energy spectrum with $\epsilon = 10^{-3}$ (solid line) and $\epsilon = 3.10^{-2}$ (dashed line) at $t = 3$; (b) Spectrum width at $t = 1$ (light grey), $t = 2$ (grey) and $t = 3$ (black) for different initial amplitudes ϵ of the linear optimal perturbation.

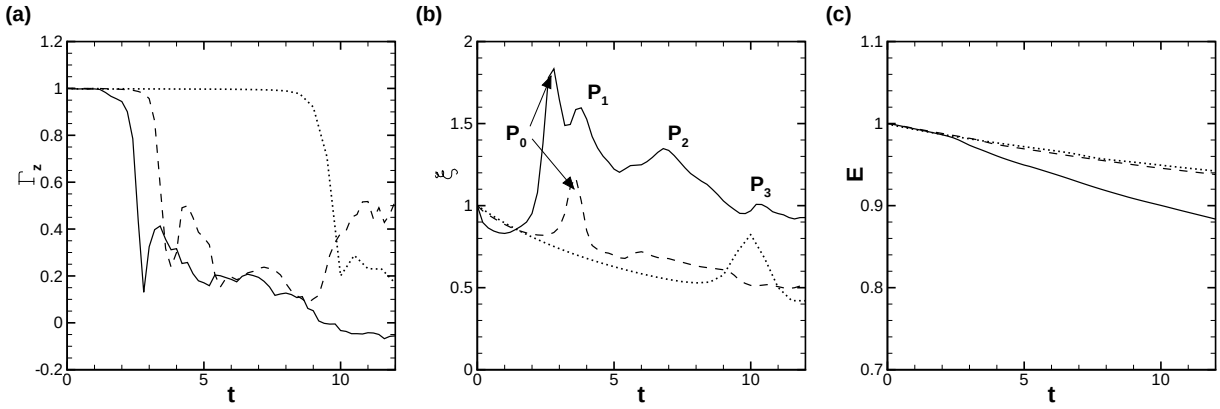

Figure 3.7: (a) Length-averaged axial circulation $\Gamma_z(t)$, (b) enstrophy $\xi(t)$ and (c) total kinetic energy $E(t)$ for $\epsilon = 10^{-2}$ (dashed lines), $\epsilon = 3.10^{-2}$ (full lines) and $\epsilon = 10^{-3}$ (dotted lines) for comparison.

"figure-of-eight" pattern the ring slowly separates into two smaller rings. This case was also described by Dhanak & Bernardinis [24] for rings of axis ratio l/L under 0.2. The axis ratio of the elliptic ring at $t = 7$ in this case is $l/L = 0.195$. The separation of the ring into two smaller rings occurs in a very similar manner to the first connection of the vortices. Such a doubling of the dominant longitudinal wavelength has been observed in previous works [73, for example]. For $\epsilon = 3.10^{-2}$ the periodic behaviour stops soon after the first exchange between γ_z and γ_x. This occurs after the first growth of Γ_z at $t = 3$ in figure 3.7 (a). Γ_z then slowly drops to around zero at $t \approx 9$ and eventually becomes negative, implying that the periodic ring state is halted and a completely different state is in progress. In fact, analysis of figure 3.4 shows that once the first elliptic ring shape is reached (at $t = 7$) the deformation of the ring is stopped and it slowly loses coherence and breaks up under the effect of the many small-scale structures that have developed around the ring over time.

Initially, the enstrophy in both simulations decreases. As before, considerable growth (see mark P_0 in figure 3.7 (b)) occurs at times coinciding with the collision of the vortices, which involves massive vorticity stretching on the centerplane separating the two cores. Subsequently for $\epsilon = 10^{-2}$ the enstrophy decreases much more slowly and finally reaches the reference state $\epsilon = 10^{-3}$, meaning that no spectacular

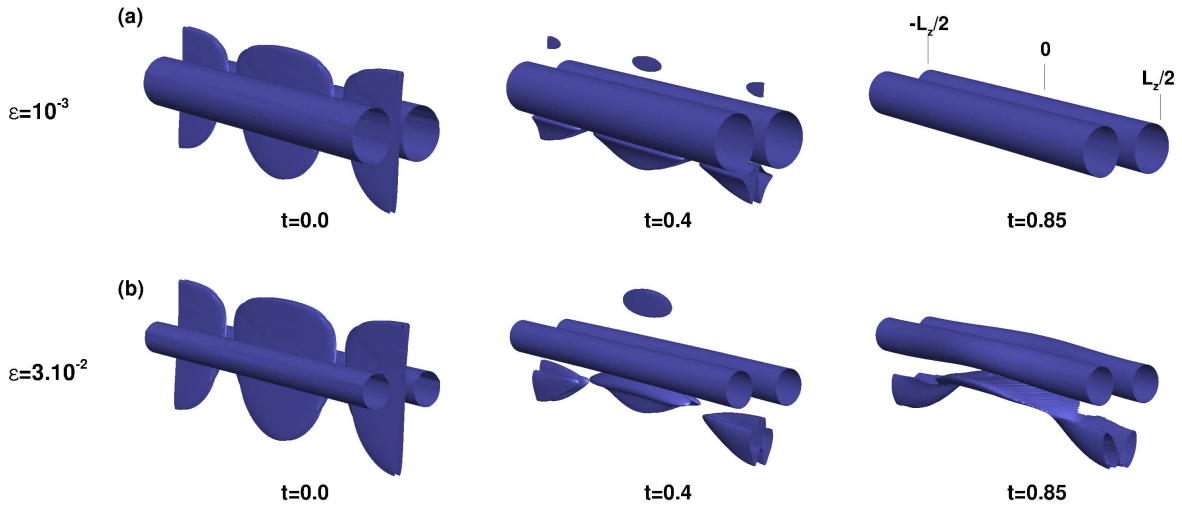

Figure 3.8: Initial vorticity contour evolution for (a) $\epsilon = 10^{-3}$ at 0.2% $|\omega_{max}\,(t=0)\,|$ (§ 3.3) and (b) $\epsilon = 3.10^{-2}$ at 10% $|\omega_{max}\,(t=0)\,|$

event occurs. However for $\epsilon = 3.10^{-2}$ several peaks in enstrophy (P_0 to P_3) occur after linking. Moreover the final mean level of enstrophy remains much higher. This can be related to the persistence of small scales in the flow. The first peak (P_1), at $t \approx 3.8$ corresponds to the stretching of vorticity in the later stages of the linking phase, notably within the bridges and induced by the bridges on the remaining threads. This strongly nonlinear amplification has been observed by Melander & Hussain [70], Marshall et al. [68] and Hussain & Duraisamy [45]. Two other bumps (P_2 and P_3) occur at $t \approx 6.7$ and $t \approx 10$ which were absent in the low ϵ cases and which correspond to the encounter of opposite parts of the ring. Figure 3.7 (c) gives the evolution of the kinetic energy of the flow. Up to $t \approx 2$ both cases see the kinetic energy decreasing at the same rate, which is about that of the linear perturbation $\epsilon = 10^{-3}$. However linking in the case $\epsilon = 3.10^{-2}$ promotes an increased decay which is not observed in the case $\epsilon = 10^{-2}$. This increased dissipation stems from the larger production of smaller scales.

3.5 Accelerated decay

The results presented in § 3.4 have demonstrated that for initial amplitudes greater than ϵ_c, the evolution of the flow is significantly changed compared with the reference evolution described in § 3.3. Most importantly the flow rapidly loses most of its coherence. The underlying physical mechanisms are described in the following paragraphs. Note that the formation of a pair of vortex rings from the initially single elliptic ring observed in the case $\epsilon = 10^{-2}$ and the subsequent evolution which, from our simulation results, remains strongly coherent, is not discussed in the present study.

According to figure 3.5 the evolution over the first characteristic time is linear, regardless of the perturbation amplitude. This is confirmed by comparing the development of the vorticity contours of figure 3.8 in the linear (a) and nonlinear (b) cases up to $t \approx 0.4$. Note that the contour level is chosen to be much lower for the $\epsilon = 10^{-3}$ case so that the perturbation can be seen. The perturbation sheets are amplified at the leading hyperbolic point and stretched horizontally beneath the cores, leading to the beginning of the vortex displacement. Details of this process are given by Brion et al. [15]. At $t = 0.85$ in the $\epsilon = 10^{-3}$ case (§ 3.3), the perturbation rapidly disappears whereas for $\epsilon = 3.10^{-2}$ the initial perturbation energy is sufficient to resist viscous dissipation and becomes further involved in the vortex pair dynamics.

By definition, the perturbation is modulated at the Crow wavelength and therefore the vorticity

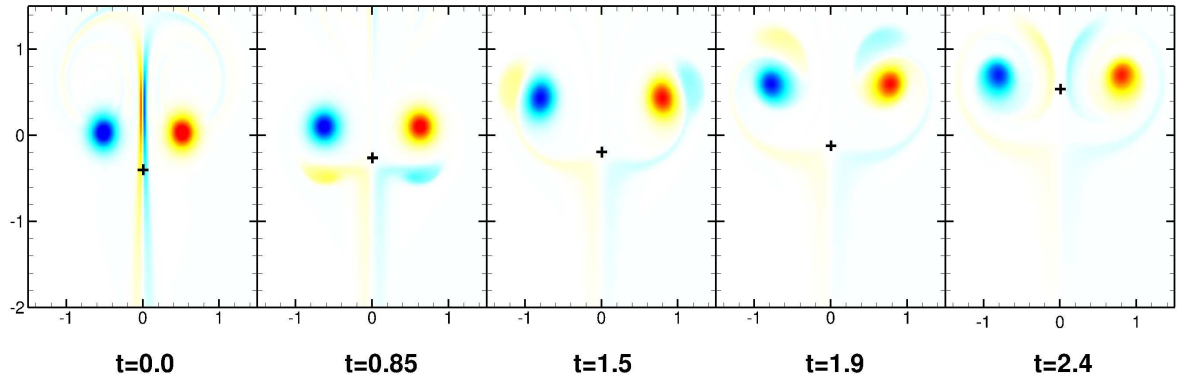

Figure 3.9: (x, y)-plane slice of the axial vorticity at $z = 0$ at times $t = 0$; $t = 0.85$; $t = 1.5$; $t = 1.9$; $t = 2.4$. + gives the position of the leading hyperbolic point.

sheets change sign every half-wavelength. The subsequent progression can be split into two domains: one in which the perturbation vorticity is of the same sign as the vortex in the corresponding half-domain ($x > 0$ or $x < 0$), and one in which the signs are opposite. When stretched at the leading hyperbolic point, the sheets become more compact and form vortex-like structures (see figure 3.8, $t = 0.85$) below the primary vortices. From this point, the flow can be viewed locally as a four-vortex type configuration, counter-rotating in $z \in [-L_z/4; L_z/4]$ and co-rotating in $z \in [-L_z/2; -L_z/4[\cup]L_z/4; L_z/2]$.

Figure 3.9 shows how axial vorticity evolves with time in a transverse (x, y)-plane at $z = 0$, the centre of the counter-rotating section. The secondary vortices are advected along the lower oval streamline and eventually tear away from the sheets. They are then drawn closer to the original vortices by 3D self-induction due to their horseshoe shape as shown in figure 3.10 at $t = 1.5$. The proximity between each original vortex and its opposite signed secondary vortex encourages local dynamics on each side, that are added to the interaction between the original vortices. Mutual-induction between the newly formed dipoles pulls the original vortices upwards and outwards, exaggerating the sinusoidal deformation of the vortex cores as can be seen at $t = 1.5$. When the secondary vortices reach the top of the dipole, they are dragged into the downwash between the cores, and recommence their advection around the vortices ($t = 2.4$). Let Γ_2 and b_2 be the circulation and separation of the secondary vortices and Γ_1 and b_1 those of the primary vortices at $z = 0$. The ratio Γ_2/Γ_1 remains approximately constant in time such that $\Gamma_2/\Gamma_1 \approx -0.3$, and the distance ratio $b_2/b_1 \approx 1$. This matches the observation of Fabre et al. [33] for a counter-rotating vortex pair: the system is periodic, the vortices orbit around the vorticity centroids.

As can be observed in figure 3.10, at $t = 3.4$ the vortex cores present visible short-wave deformations. Those in the centre of the domain ($z/\lambda_z \in [-0.2, 0.2]$) result from the induction caused by the nearby secondary structures. To evaluate the scale of these deformations the axial evolution of the dispersion radius $\delta a\,(z) = (a\,(z) - \bar{a})\,/\bar{a}$ in this central region has been evaluated on each (x, y)-plane $S(z)$, with $a(z)$ calculated by

$$a\,(z) = \frac{\int_{S(z)} r\omega_z dxdy}{\int_{S(z)} \omega_z dxdy} \tag{3.18}$$

with $r = \left((x - x_c)^2 + (y - y_c)^2\right)^{1/2}$ and x_c and y_c the coordinates of the vortex core centre given by:

$$x_c(z) = \frac{\int_{S(z)} x\omega_z dxdy}{\int_{S(z)} \omega_z dxdy} \tag{3.19}$$

$$y_c(z) = \frac{\int_{S(z)} y\omega_z dxdy}{\int_{S(z)} \omega_z dxdy} \tag{3.20}$$

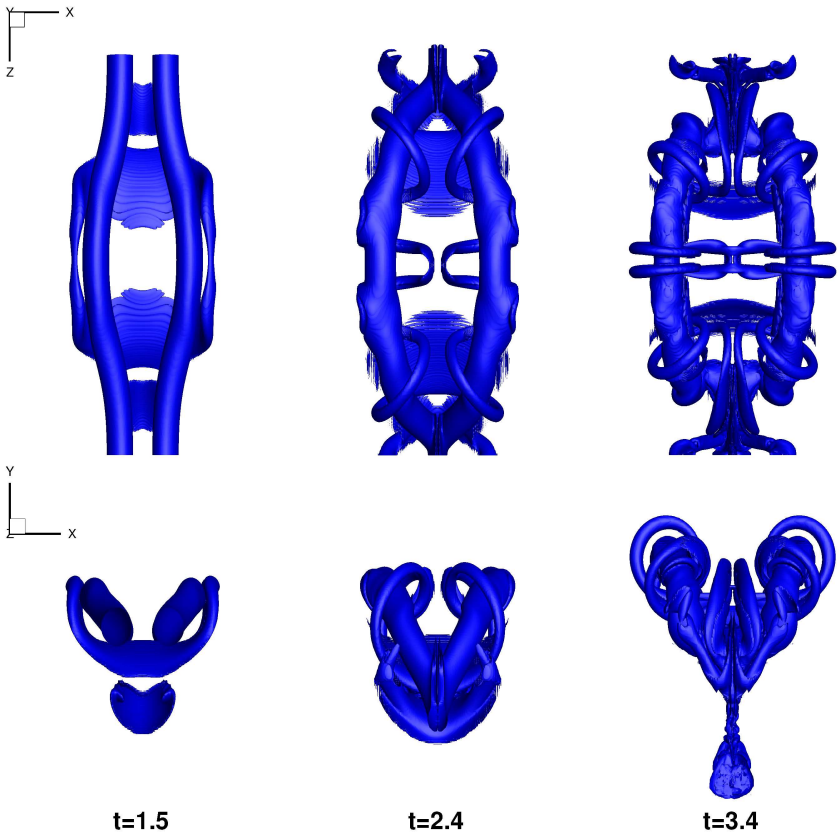

Figure 3.10: Vorticity isocontours at a value of $20\%|\omega_{max}\,(t=0)\,|$ at $t = 1.5$, $t = 2.4$ and $t = 3.4$ for $\epsilon = 3.10^{-2}$.

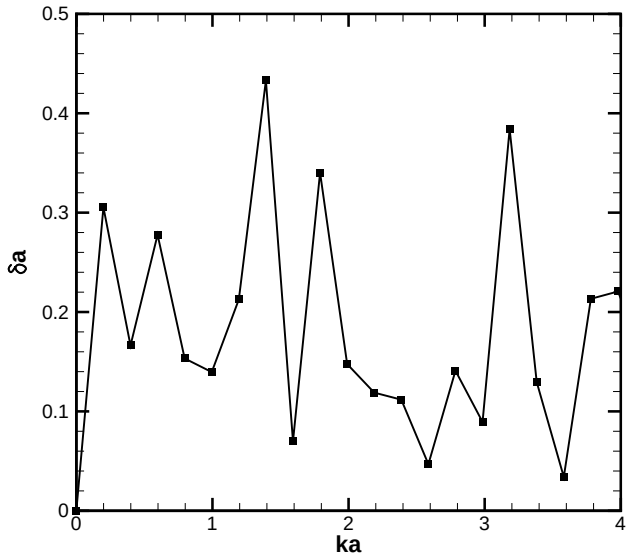

Figure 3.11: Dispersion radius δa as a function of non-dimensional axial wavenumber ka at $t = 3.4$.

$\bar{a}$ is the average dispersion radius over the section studied:

$$\bar{a} = \frac{\int_{-0.2}^{0.2} a(z)dz}{\int_{-0.2}^{0.2} dz} \tag{3.21}$$

External noise is filtered out by imposing a minimum vorticity of 10% of the maximum vorticity in each section $S(z)$ in the calculations. Figure 3.11 gives the variation of dispersion radius δa as a function of the non dimensional wavenumber ka. Several spikes can be seen, in particular for $ka \approx 1.3$ which lies in the range of the optimal perturbation of an isolated vortex [2]. This suggests that the accelerated decay is additionally promoted by an optimal perturbation of the vortex cores.

Figure 3.12 gives the axial vorticity contours in the $z = L_z/2$-plane, the centre of the co-rotating section, which corresponds with the foreground plane of figure 3.10. The secondary vortices form a second counter-rotating dipole which moves downwards under the combined effects of the velocity field imposed by the primary vortices and of the self-advection between the perturbation vorticity. The separation distance ratio is $b_2/b_1 \ll 1$ and the behaviour is divergent which concurs with the aforementioned study of Fabre et al. [33] except that here the perturbation vorticity diffuses before escaping the primary vortices. In return the secondary vortices induce a displacement of the primary structures towards one another, especially at instigation. This results in an increased 3-D deformation of the vortices: the part of the vortices at $z = \pm L_z/2$ is drawn to the symmetry plane and downwards whilst, as stated earlier, the part at $z = 0$ is pulled away from the symmetry plane and upwards. This, in addition to the natural deformation of the vortices under the $m = 1$ Kelvin mode at the Crow wavelength, provokes the accelerated linking of the vortices. At $z = L_z/2$ the original cores are then pressed tightly together in a head-tail shape, ready for the connection of the vortices into rings at $t = 2.4$. The evolution of the location of the leading hyperbolic point, shown in figure 3.9 and 3.12, also shows that the entire oval surrounding the recirculating flow around the vortices is modified in this process.

In addition to this analysis of the axial vorticity in two sectional planes, the map of vorticity contours in figure 3.10 demonstrates the appearance of smaller-scale variations in the flow in the long term. They are the remnants of the initial perturbation which were not present for lower values of ϵ. Observation of figures 3.10 and 3.4 shows that this added noise deteriorates into smaller scales through tilting and

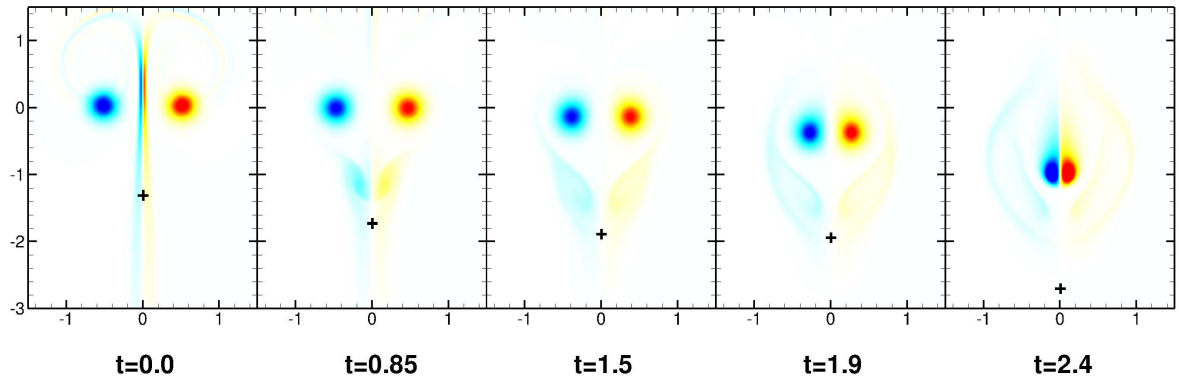

Figure 3.12: (x, y)-plane slice of the axial vorticity at $z = L_z/2$ at times $t = 0$; $t = 0.85$; $t = 1.5$; $t = 1.9$; $t = 2.4$. + gives the position of the leading hyperbolic point.

stretching, continuously forcing the primary vorticity, until the vortex ring finally breaks, at $t = 12$.

3.6 Conclusion

This paper reports on the long-term evolution of the Crow instability in a homogeneous and turbulence-free environment. A pair of Gaussian vortices is perturbed by the most amplified perturbation of the Crow instability, the adjoint mode, introduced with various initial amplitudes. When subjected to an infinitesimal initial perturbation, the vortices undergo a series of transformations: the linear Crow stage, linking and the formation of vortex rings. The ensuing stage of evolution is found to be a periodically evolving ring state. While such a phenomenon was known to occur in elliptic vortex rings, it is the first time that its manifestation in the evolution of wake vortices has been demonstrated. This result was obtained by pursuing the flow computation for an unusually long time. From an application point of view this demonstrates that aircraft wake vortices may last a great deal longer than would have been expected. For instance Spalart [92] determined that the typical lifespan of an aicraft wake is around 5 to 6 characteristic times. Such data is acquired usually from Lidar measurements of wake vortices conducted from the ground. The disparity between that and the lifespan obtained in this present analysis may lie in the possible inability of Lidars to measure vortex rings due to the complexity of such flows and the constraints of Lidar measurement (namely volume integration and projection of the flow velocity along the laser beam). The relatively low Reynolds number and large initial aspect ratio of the vortices in the present study are thought not to reduce the scope for application, as observation of actual aircraft wakes show practically identical initial dynamics.

In this study the adjoint mode of the Crow instability is evaluated as a solution to prevent the periodic ring state. While the adjoint is the initial perturbation that triggers the largest Crow instability growth, its potential to disrupt the flow in the stages following the linking of the vortices was previously unknown. Also, were it possible to disrupt the flow using the adjoint, the cost required to do this effectively needed to be identified. Varying the initial perturbation amplitude from that used for the reference state described in § 3.3 to larger, yet still low values, showed the existence of a threshold distinguishing two behaviours. This threshold corresponds to a perturbation of about 3% in relative amplitude compared with the background flow. When subjected to a perturbation of amplitude higher than the threshold, the development of the periodic ring state is stopped at the beginning of the first period. The once coherent vortical structures transform into small incoherent vortices that, had the simulation been pursued longer, would certainly have initiated the turbulent cascade. The physics of this process was analysed in detail, showing that the flow dynamics split into two regions per wavelength in the longitudinal direction, depending on

the interaction of vorticity sign between the primary vorticity and the perturbation. Each zone could be likened locally to a four-vortex type configuration, that promotes local induction phenomena and increases the initial deformation of the vortices, resulting in an accelerated linking. In addition, it is suggested that the remnants of the adjoint mode perturbation, that wrap around the vortices, trigger a single-vortex type optimal perturbation in each individual vortex. Overall these additional dynamics lead to a considerable reduction of the vortices' lifespan, since they are seen to disintegrate after only 13 characteristic times.

It is evident that the dynamics of a vortex pair is particularly resilient to initial forcing, however the present analysis also shows that large structural variations can take place. The varying parameter here was the initial perturbation amplitude ϵ. By increasing ϵ from 10^{-3} to 10^{-2} the flow evolved eventually into a sequence of two vortex rings per Crow wavelength, thus doubling the initial spatial periodicity of the wake. These differences compare well with documented vortex ring dynamics. Such disparity in the evolution of the flow raises new questions concerning the sensitivity of wake vortices to external parameters and should act as strong motivation for further analysis.

Chapter 4

An optimal nonlinear optimisation approach to the two-dimensional dynamics of an isolated Gaussian vortex

This chapter is devoted to the description and characterisation of the two-dimensional nonlinear optimal perturbations of an isolated vortex. The contents form a self-contained article under preparation for submission.

4.1 Introduction

The first mathematical description of vortex dynamics dates back to the time of Lord Kelvin [52] who looked into vortex neutral waves. An analytical description of these Kelvin waves is simple to retrieve when considering a vortex model of constant core vorticity known as the Rankine vortex (see Saffman [85] and Rossi [83]). The range of possible vortex core deformations is generally characterised by the azimuthal periodicity m of the perturbation. $m = 0$ modes are called 'sausaging' modes and produce longitudinal variations of the vortex radius. $m = 1$ modes are known as bending or helical modes and deform the vortex into a helical shape, either rotating faster than the vortex (co-grade modes) or against it (counter-grade and retrograde modes). Finally $m = 2$ perturbations are called double-helix modes (Fabre et al. [34]).

The sharp vorticity distribution of the Rankine vortex, although perfect for analytical studies, is very different from the vorticity distribution observed in experiments or applications which is usually close to a Gaussian profile [59, 56]. The Gaussian Lamb-Oseen (LO) vortex model has accordingly been the subject of many studies. A first analysis of its discrete vortex wave spectrum was given by Sipp et al. [90] and an exhaustive listing was later provided by Fabre et al. [34]. The most notable result of the LO spectrum analysis is the presence of singular modes that do not exist for the Rankine vortex. The first family is composed of viscous centre modes and lies in the long-wavelength limit ($k < O(Re^{1/4})$). The second family comprises critical layer modes which exhibit a single peripheral vorticity distribution made of tightly wrapped spirals, generally involving a Kelvin wave in the vortex core. These linear singular modes are known to be strongly affected by viscosity and are accordingly considerably more damped than regular Kelvin waves.

A critical layer arises when the phase speed of the wave is equal to the rotation rate of the unperturbed vortex at a critical radius r_c: $\gamma(r_c) = m\Omega(r_c) - \omega = 0$. Such a condition cannot be met in the Rankine constant rotation flow but is permitted by the continuously evolving radial distribution of Ω present in the LO vortex. The critical layer condition generates a singularity in the inviscid linearised Navier-Stokes equations that can be resolved either by introducing viscosity or nonlinearities, depending on the value of the Haberman parameter $h = 1/(Re\epsilon^{3/2})$ where ϵ is the amplitude of perturbation (see Le Dizès [57]). In the linear domain ($\epsilon << 1$), $h >> 1$ so the viscous correction applies. This leads to the viscous damping of the singular critical layer waves. For strong enough perturbations (ϵ finite), and depending on the Reynolds number, it is possible that $h << 1$, in which case a nonlinear critical layer appears, characterised by neutral oscillations essentially related to the absence of phase change across the layer (Caillol & Maslowe [18]). This was confirmed by Le Dizès [57] who related the occurrence of the nonlinear critical layer in the $m = 2$ case to the switch of an axisymmetric vortex to a tripolar quasi-steady state. Interestingly this cast new light on the results previously obtained by Rossi et al. [82] which demonstrated that an initial axisymmetric vortex can turn into a quasi-steady tripole when an $m = 2$ perturbation of sufficient initial amplitude is applied. Furthermore, Le Dizès showed that such quasi-modes exist for all vortex profiles, even for larger m if the vorticity profile is steep enough. In these analyses, the term 'quasi-steady' means that the vortex deformation is maintained in an appropriate reference frame on a $O(Re)$ time scale. Currently only steady-state solutions of the monopole, dipole and tripole types are known for vortical flows. The $O(Re)$ decrease contrasts with the dynamics observed below the nonlinear threshold in which any deformation is seen to decrease on a $O(Re^{1/3})$ time scale due to the shear diffusion mechanism imposed by the vortex. The shear diffusion mechanism was analysed by Bernoff & Lingevitch [12] and constitutes the main mechanism behind the axisymmetry of most vortices. In this process the differential advection by the vortex winds perturbations into increasingly thin spirals (see Lundgren [62]). Owing to the large gradients between the thinning spiral arms, viscous diffusion acts more efficiently. Rossi et al. [82] show that only perturbations of sufficient amplitude are able to escape this axisymmetrisation by creating closed streamlines inside the vortex using vorticity of opposite-sign compared with the original vortex.

It is clear that critical layers play an important role in the dynamics of vortices with continuous vorticity profiles. Their implication in the potential, almost perpetual deformation of a once axisymmetric vortex is a fundamental feature of two-dimensional vortex dynamics that deserves further analysis. In particular, until now only $m = 2$ and higher azimuthal wavenumber structures have been found and one can legitimately wonder for instance whether an $m = 1$ structure could also emerge. In addition it is noteworthy that the critical layer structure closely resembles the optimal perturbations of isolated vortices found for instance by Antkowiak & Brancher [2] and Pradeep & Hussain [80]. Furthermore, Antkowiak & Brancher demonstrated how these optimal perturbations, in the 3D $m = 1$ case, could use filaments of vorticity located at a finite radius of the vortex to resonate with Kelvin wave modes in the vortex core and thus optimise transient energy growth. The question that arises here is whether such optimal structures, being located in regions known to sustain critical layers, could use the nonlinear critical layer described by Le Dizès to promote energy growth and encourage the flow to adopt a new quasi-steady vortex state with higher kinetic energy levels.

In this analysis a nonlinear perturbation optimisation is carried out in order to investigate these potential connections and further explore the 2D dynamics of isolated vortices, taking the LO vortex as an example.

Despite the numerous results available regarding the dynamics of such vortices, it is surprising to find that several important questions remain unanswered, some of which the present analysis is intended to resolve. One point concerns two-dimensional vortex stability which does not appear to have been adressed specifically. All studies have focused on the three-dimensional dynamics, and have obtained

results in two-dimensions by considering the $k \to 0$ limit. The purely two-dimensional case however is quite specific because of the mandatory conservation of linear and angular momentum. For instance the $(k, |m|) = (0, 0)$ expansion mode is not physically possible since it requires a change in angular momentum. Similarly the $(k, |m|) = (0, 1)$ displacement mode requires a change in linear momentum. The validity of the $(k, |m|) = (0, 1)$ critical layer modes described by Sipp & Jacquin [90] and Fabre et al. [34] regarding these constraints is not discussed but certainly follows the same restrictions. On the contrary $k = 0$ with $|m| > 1$ modes are physically possible (some of them also exhibit critical layers) but they have received little attention until now. Another question relates to the description of the continuous spectrum of the LO vortex which has never been investigated despite the fact that it is known to be the basic ingredient of transient growth. Mao & Sherwin [65] demonstrated how the non-normality of the continuous spectrum alone determines the optimal transient amplification in a Batchelor q-vortex. Fabre et al. [34] conjectured that the continuous spectrum is composed of modes with frequency positioned on the real axis $\omega_i < -k^2/Re$. Mao & Sherwin [64] recently investigated the continuous spectrum of the Batchelor vortex and showed the existence of a free stream and potential spectra. They also confirmed the hypothesis of Fabre et al. [34] about the location of the continuous spectrum in the complex plane, with the clarification that this location is only that of the free-stream spectrum (the potential spectrum has a wider distribution not restricted to the real axis). Mao & Sherwin [64, 65] did not consider the LO limit of the Batchelor vortex (when the swirl $q = 0$) since they focused on the range $q \in [2; 3]$ (with an additional value $q = 0.761$ for validation purposes). Interestingly they considered the $k = 0$ case in this range of q values and showed that in two-dimensions the linear optimal perturbation causes the vibration of the vortex core and that nonlinearities obtained by conducting a full Direct Numerical Simulation of the linear optimal superimposed on the base flow lead to lower growth rates and saturation. They linked this dynamics to the frequently observed vortex meandering phenomenon.

Compared with normal mode analysis the optimal perturbation approach is not constrained by the conservation principles and thus enables access to a wider set of dynamics. Moreover, by using optimal perturbation on stable flows, perturbation growth mechanisms could be found that may explain state transition in two-dimensional flows.

Optimal perturbations of an isolated 3D LO vortex have been investigated in the linear framework by Antkowiak & Brancher [2, 3] and Pradeep & Hussain [80] but never in the 2D framework, apart from the PhD work of Bisanti [13] which we describe fully in § 5.2.2. In particular Antkowiak & Brancher [2] and [3] determined the linear optimal perturbations of a LO vortex for azimuthal wavenumbers $m = 1$ and $m = 0$ respectively, while [80] carried out the study on all azimuthal wavenumbers up to $m = 4$ and described the linear 2D and 3D transient growth mechanisms. They demonstrated that linear optimal perturbation growth occurs through vortex strain by a process which is equivalent to the Orr mechanism in plane shear flows [37] and that growth is stalled by the core rotation. Very little work has been undertaken using nonlinear optimisation on vortices (again besides the PhD work of Bisanti [13]) despite the potential benefit of including the nonlinear terms. Indeed when applied to other flows such as the pipe flow [81] or the boundary layer of a flat plate [20], nonlinear optimisation has produced remarkably interesting results. In these cases, the nonlinear optimal perturbation not only induces greater perturbation growth but also triggers transition to turbulence from a much lower initial perturbation amplitude. Furthermore, the nonlinear optimal perturbation tends to be more spatially localised, leading to the belief that it is more physically relevant than the linear optimal.

The present work is a first step that has allowed the development of the optimisation tool before extending the analysis to three dimensions. However the 3D problem involves highly demanding computations and deserves a fully separate study.

The paper is organised as follows. First the numerical methods used to carry out the Direct Numerical Simulations and the optimisation process are detailed (§ 4.2). Then the nonlinear optimal perturbations

of a LO vortex are characterised and compared with the linear optimals, and the nonlinear growth mechanisms are highlighted (§ 4.3). Finally the effect of the nonlinear optimals on the vortex and subsequent flow dynamics are described (§ 4.4). Conclusions are drawn in § 4.5.

4.2 Problem formulation

4.2.1 Governing equations

The flow is governed by the incompressible Navier-Stokes equations:

$$\nabla \cdot \boldsymbol{u} = 0 \tag{4.1}$$

$$\partial_t \boldsymbol{u} + (\boldsymbol{u} \cdot \nabla)\, \boldsymbol{u} = -\frac{1}{\rho}\nabla p + \nu \nabla^2 \boldsymbol{u} \tag{4.2}$$

with ν the kinematic viscosity and ρ the density. The optimisation analysis is performed using a perturbation framework. The velocity is decomposed as $\boldsymbol{u} = \boldsymbol{U} + \boldsymbol{u}'$ where $\boldsymbol{U}$ is the base flow and $\boldsymbol{u}'$ is the perturbation. This decomposition is more convenient than a full DNS: as the perturbation flow is calculated separately, complex post-processing to separate the perturbation field from the base flow is avoided. Once the optimal perturbation is determined, regular DNS is carried out to ensure the validity of the results.

The Navier-Stokes equations are solved using the open-source solver Nek5000 [38] which is based on the spectral elements method. The computational domain is a disc of radius $R = 15a$, with a the dispersion radius of the vortex. The domain is divided into N_{el} elements, each further discretised by $N_{GLL} = 8$ Gauss-Lobatto-Legendre (GLL) points. The central part of the mesh is a square of size $[-L_x/2; L_x/2] \times [-L_y/2; L_y/2]$ with $L_x = L_y = 8$, which is divided into $N_x = N_y = 16$ elements. This square is surrounded by curved-edge elements with a certain degree of flare to progressively transition to the circular geometry in the external region, up to the radius R. The total number of elements is $N_{el} = 512$. The central square contains most of the significant dynamics of the flow (that is the vorticity). The largest divisions in each direction within the central square are $\Delta x_{max}/a = \Delta y_{max}/a \approx 0.1$ determined using the formula $\Delta x, y_{max} = \pi L_{x,y}/\left(2\left(N_{GLL} - 1\right) N_{x,y}\right)$. The dimension and resolution of the mesh has been appraised in a preliminary validation phase detailed in § 4.2.3.

The effect of the boundary at $r = R$ appeared to be quite problematic in the first stage of the analysis. The mesh was initially taken as a simple square with periodic boundary conditions. However the optimal perturbation algorithm would systematically find an initial perturbation located at these boundaries. This is consistent with the findings of Sipp & Jacquin [89] and Gau & Hattori [42] who both found perturbations on the symmetry lines of the Taylor-Green periodic flow, which is very similar to our square with periodicity situation. In order to prevent this effect and isolate the vortex from the borders, a buffer zone has been implemented on the external part of a circular domain from $r = 12a$ to $r = R$. In this region viscosity varies radially in a continuous manner from $\nu = Re^{-1}$ to 10^{-1}. Zero-velocity Dirichlet conditions are applied at the external boundary $r = R$.

4.2.2 Base flow

The base flow is an isolated Lamb-Oseen vortex of circulation Γ and dispersion radius a. Results are rendered non-dimensional using a and Γ. Consequently the Reynolds number is $Re = \Gamma/(2\pi\nu)$. The azimuthal velocity profile of the LO model is $V = \Gamma/(2\pi r)\left(1 - e^{-r^2/a^2}\right)$ (see figure 4.5 for velocity profile). The reference time τ is the rotation time of the vortex $\tau = 4\pi^2 a^2/\Gamma$. Throughout the study, the base flow is considered to be 'frozen', meaning that the vortex is not subjected to viscous diffusion. This

approximation is valid when the evolution time of the flow, related to its constitutive perturbation time scale τ, is small compared with the viscous time scale here given by τ_ν. The viscous diffusion time scale of a vortex is $\tau_\nu = 2\pi a^2/\nu$. The ratio of the two time scales τ_ν/τ is equal to the Reynolds number and is therefore sufficiently large. A rigorous validation of the frozen base flow approach is carried out in appendix A by calculating the optimal perturbations with a diffusing base flow and comparing with the results detailed hereafter.

4.2.3 Nonlinear optimisation

The aim is to determine the optimal perturbation of an isolated vortex, that is the perturbation that induces the largest disturbance growth over a given time T. Here the perturbation kinetic energy E is chosen as a measure of this optimal growth. Given a perturbation $\boldsymbol{q} = (\boldsymbol{u}', p')^T$ with $\boldsymbol{u}' = (u', v')^T$, the perturbation kinetic energy E is given by

$$E(t) = \int_D \left(u'(t)^2 + v'(t)^2\right) dS \tag{4.3}$$

with D the spatial domain. The objective is to find the initial perturbation $\boldsymbol{u}_0 = \boldsymbol{u}(t=0)$ of imposed initial energy E_0 that generates the largest energy gain $G(T, \boldsymbol{u}_0) = E_T/E_0$ where $E_T = E(t=T)$. The initial energy E_0 is defined as a fraction of V_0^2 where $V_0 = \Gamma/(2\pi a)$ is the characteristic velocity of the base flow. A Lagrange multiplier technique is applied with constraints corresponding to the incompressible Navier-Stokes equations and the boundary conditions. The Lagrangian functional $\mathcal{L}$ is defined:

$$\mathcal{L}\left(\boldsymbol{q}, \boldsymbol{q}^+, \boldsymbol{q}_0, T\right) = G(T, \boldsymbol{q}_0) - \left(\boldsymbol{q}^+, \mathbf{F}(\boldsymbol{q})\right) \tag{4.4}$$

where $\boldsymbol{q}^+ = (u^+, v^+, w^+, p^+)^T$ are the Lagrange multipliers or adjoint variables and $\mathbf{F}(\boldsymbol{q}) = 0$ represents the Navier-Stokes equation in perturbation mode:

$$\nabla \cdot \boldsymbol{u}' = 0 \tag{4.5}$$

$$\frac{\partial \boldsymbol{u}'}{\partial t} + (\boldsymbol{U}\cdot\nabla)\boldsymbol{u}' + (\boldsymbol{u}'\cdot\nabla)\boldsymbol{U} + (\boldsymbol{u}'\cdot\nabla)\boldsymbol{u}' = -\nabla p' + \frac{1}{Re}\nabla^2\boldsymbol{u}' \tag{4.6}$$

Note that in 4.4 the following scalar product is used

$$(\boldsymbol{a}, \boldsymbol{b}) = \int_T <\boldsymbol{a}, \boldsymbol{b}> dt \tag{4.7}$$

with $<\boldsymbol{a}, \boldsymbol{b}> = \int_D \boldsymbol{a}^T \boldsymbol{b} dV$.

The gradient of the functional $\mathcal{L}$ with respect to the perturbation variables $\boldsymbol{q}'$ leads to the adjoint equations $\boldsymbol{F}^+(\boldsymbol{q}^+) = 0$ given by

$$\nabla \cdot \boldsymbol{u}^+ = 0 \tag{4.8}$$

$$\frac{\partial \boldsymbol{u}^+}{\partial t} - (\boldsymbol{U}\cdot\nabla)\boldsymbol{u}^+ - (\boldsymbol{u}'\cdot\nabla)\boldsymbol{u}^+ = -\boldsymbol{u}^+\cdot(\nabla\boldsymbol{U})^T + \boldsymbol{u}'\cdot\left(\nabla\boldsymbol{u}^+\right)^T \tag{4.9}$$

$$+ \nabla p^+ + \frac{1}{Re}\nabla^2\boldsymbol{u}^+ \tag{4.10}$$

and the compatibility equations:

$$\boldsymbol{u}^+ = \frac{2}{E_0}\boldsymbol{u}'(T) \tag{4.11}$$

Boundary conditions for the adjoint field are the same as for the direct field. Finally the derivative of $\mathcal{L}$

	Re	T	$G(T)$	Present results
Antkowiak & Brancher [2]	1000	40	770	764
Pradeep & Hussain [80]	796	9.88	62	63

Table 4.1: Gain reached with the $m = 1$ linear optimal perturbation at Reynolds number Re and horizon time T - comparison with other works.

with respect to the initial condition $\boldsymbol{u}_0$ yields the gradient used to optimise $\boldsymbol{u}_0$:

$$\frac{\partial \mathcal{L}}{\partial \boldsymbol{u}_0} = -2\frac{E_T}{E_0^2}\boldsymbol{u}\left(0\right) + \boldsymbol{u}^+\left(0\right) \tag{4.12}$$

The optimisation is carried out following an iterative approach (see Zuccher et al. [97], Pringle & Kerswell [81], and Cherubini et al. [20]) involving the integration of the Navier-Stokes equations forward in time and the adjoint equations backwards in time. The initial perturbation energy constraint is not imposed within the functional but using a geometric update technique described by Douglas et al. [26] and applied successfully in a similar problem by Foures et al. [40]. It is best to initialise the optimisation algorithm using a white noise rather than the linear optimal, as shown in a study detailed in § 4.3.2.

An important question is whether there is a limit of E_0 over which no optimal perturbation can be found. Were the flow to reach a turbulent state over the optimisation time period (between $t = 0$ and $t = T$) then the sensitivity of the initial conditions $\boldsymbol{q}_0$ to the final state $\boldsymbol{q}_T$ would inhibit convergence to the optimal perturbation. This was noted in particular by Pringle & Kerswell [81]. In the present analysis no limit could be found, and it was decided to limit E_0 to 10^{-1} at the largest. However the two-dimensional case may be quite specific as one does not expect turbulent events to occur, limitations on E_0 may more likely exist for three-dimensional flows.

4.3 Optimal perturbations of a Lamb-Oseen vortex

In this paragraph, previous results concerning the optimal perturbation of a LO vortex are recalled and new results are presented. These results are compared with previous studies in the linear and nonlinear cases in order to validate the optimisation code.

4.3.1 Linear optimal perturbation

As a consequence of the axisymmetric base flow, perturbations can be decomposed as: $\boldsymbol{u'} = \tilde{\boldsymbol{u}}\left(r,t\right) exp\left(m\theta\right)$ with m the azimuthal wavenumber. Modes of different m are independent in the linear framework and the analysis can be carried out separately for each mode. The case of axisymmetric perturbations $m = 0$ is excluded from the study as these modes do not contribute to growth. The linear optimal results of other studies are retrieved with reasonable accuracy as shown in table 4.1 for the $m = 1$ mode as an example.

Figure 4.1 provides the linear optimal gains for varying horizon time for $m = 1, 2, 3$ as determined by Bisanti [13]. The gain values found for each m using the optimisation tool are identical to Bisanti's. As noted by Antkowiak & Brancher [2] the growth of the $m = 1$ displacement mode increases linearly with the horizon time at large T. This linear behaviour is preceded by a stage where modes of higher azimuthal wavenumber $m = 2$ and $m = 3$ prevail. Perturbations of azimuthal wavenumber $m \geq 2$ and $m = 1$, with the exception of the core displacement mode, are damped by shear-diffusion on a $O(Re^{1/3})$ time scale [12]. This time scale has been checked using the results displayed in figure 4.2(a) which gives the evolution of the gain for the $m = 2$ linear optimal for $T = 4.8$. Figure 4.2(b-d) illustrates the reversal of the initial

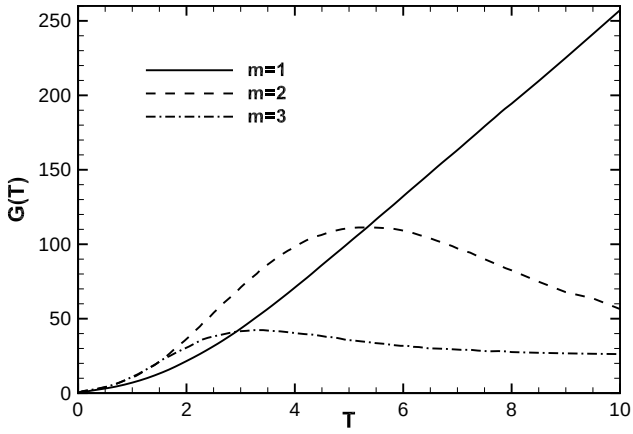

Figure 4.1: Linear optimal gain as a function of the horizon time T for $m = 1, 2, 3$ at $Re = 5000$, see [13].

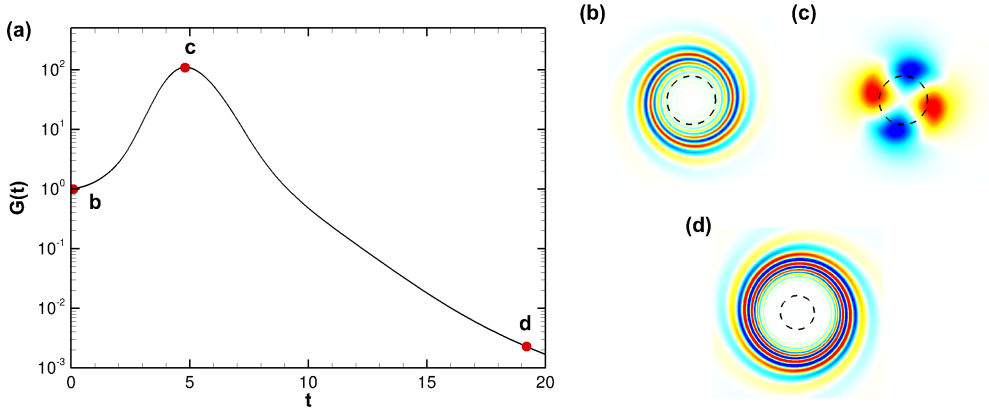

Figure 4.2: (a) Perturbation energy growth over time for the linear optimal perturbation of a LO vortex with $m = 2$ at horizon time $T = 4.8$ and $Re = 5000$; corresponding axial vorticity ω contours at times (b) $t = 0$, (c) $t = T$, (d) $t = 4T$. The dotted line indicates the vortex dispersion radius.

spiral arms by the rotation imposed by the vortex and the late-time spiral pattern before diffusion by viscosity. This last step in the evolution corresponds to the shear-diffusion mechanism, which is shown in greater detail in figure 4.3 through three different instants. The $m = 1$ case is illustrated in figure 4.4. In this case, while the outside vorticity field is weakened by the same shear-diffusion mechanism, the $m = 1$ displacement mode remains in the core long-term, and evolves on a slow time scale found to be $O(Re^{0.6})$.

The linear growth mechanism was described in detail by Antkowiak & Brancher [2] and Pradeep & Hussain [80]. In 2D it comprises two mechanisms. The first is directly apparent upon writing the perturbation kinetic energy equation integrated over the domain:

$$\frac{dE}{dt} = -\int_D u'v' r \frac{\partial}{\partial r}\left(\frac{V}{r}\right) dV \tag{4.13}$$

As the strain $S = r\frac{\partial}{\partial r}\left(\frac{V}{r}\right)$ of a LO vortex is negative (see figure 4.5), kinetic energy production occurs when $u'v'$ is positive, that is for positive Reynolds stress. As such the linear optimal perturbation of an isolated vortex takes the form of 'positive-tilt' or 'leading' spirals in order to generate transient growth. This inviscid growth mechanism is the equivalent of the Orr mechanism in plane shear flows [37]; readers are referred to Pradeep & Hussain [80] for further details. The growth is eventually halted by the

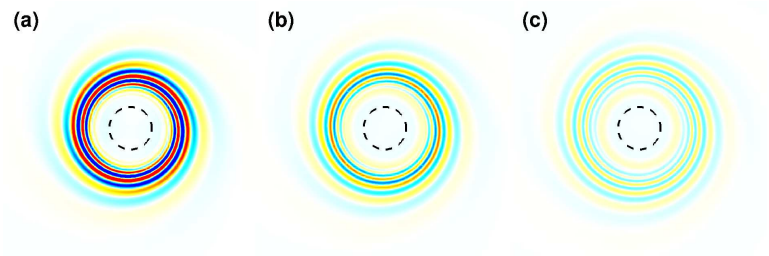

Figure 4.3: Shear-diffusion mechanism corresponding to frame (d) of figure 4.2, (a) $t = 3T$, (b) $t = 4T$, (c) $t = 5T$.

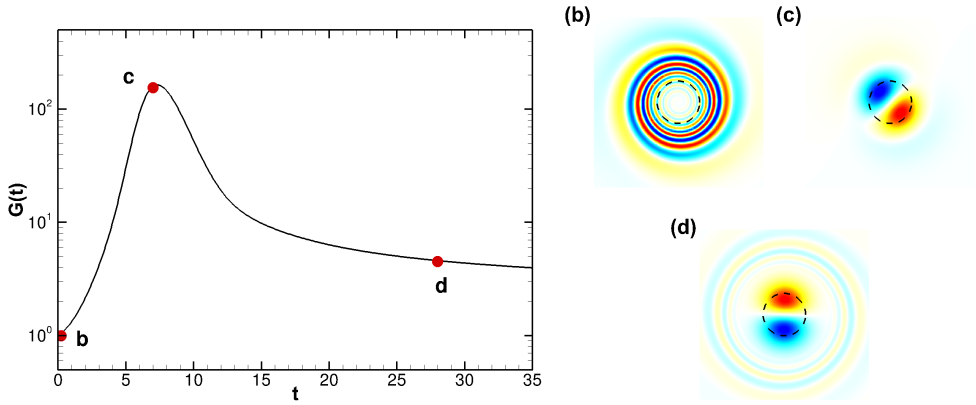

Figure 4.4: (a) Perturbation energy growth over time for the linear optimal perturbation of a LO vortex with $m = 1$ at horizon time $T = 7$ and $Re = 5000$; corresponding axial vorticity ω contours at times (b) $t = 0$, (c) $t = T$, (d) $t = 4T$. The dotted line indicates the vortex dispersion radius.

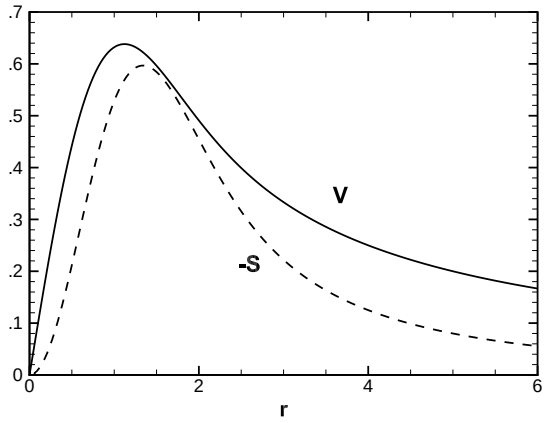

Figure 4.5: Azimuthal velocity V and strain S of a Lamb-Oseen vortex.

differential rotation of the base flow, which causes the perturbations at lower radii to rotate faster than those located further away from the core, and leads to an unravelling of the spirals and their inversion to 'negative-tilt' or 'trailing' spirals, generating negative Reynolds stress. An example of this perturbation growth and decay is given in figure 4.2 for a $m = 2$ perturbation with horizon time $T = 4.8$ at $Re = 5000$. The gain $G(T) = 109$ and perturbation vorticity contours are identical to those previously obtained by [13]. The vorticity contours (b) to (d) show the initial perturbation composed of positive-tilt spirals with $m = 2$ symmetry, the perturbation at the horizon time, and the subsequent winding of the spirals in the opposite direction as a consequence of differential advection.

The second mechanism is based on a resonance phenomenon between the peripheral perturbation and the core dynamics which is prone to Kelvin-waves. Optimal perturbations were shown by Antkowiak [1] and Pradeep & Hussain [80] to select predominantly a radial location for the initial perturbation that would rotate at the frequency of the least stable mode of the vortex spectrum. In this situation the peripheral perturbation is able to progressively induce a core mode in the vortex through resonance. This can be appreciated best by observing the linearised Helmholtz equation for the perturbation axial vorticity ω':

$$\frac{\partial \omega'}{\partial t} + \frac{V}{r}\frac{\partial \omega'}{\partial \theta} + u'\frac{d\Omega}{dr} = \nu \Delta \omega' \tag{4.14}$$

with Ω the base flow axial vorticity. The advection of the perturbation vorticity by the base flow generates radial velocity u' within the vortex core according to the Biot-Savart law. Through the third term in the left-hand-side, the perturbation draws on the base flow vorticity in the core to generate the dominant eigenmode. In 2D, the core dynamics is dominated by its $m = 1$ displacement mode, which is stationary [85]. Antkowiak showed how the large time $m = 1$ optimal generates infinite growth by being located infinitely far from the vortex and thus making an ideal resonance with the stationary displacement mode of the vortex.

In the short term the optimal perturbation is expected to rely on the Orr mechanism which is immediately accessible. On the contrary, the resonance mechanism is expected to require some time to become established because a preliminary unravelling of the initial vorticity spirals must occur for induction to be possible, therefore this mechanism acts at longer time scales. As a consequence the short term growth will be driven primarily by the Orr mechanism and larger horizon times will additionally benefit from the induction mechanism. This combination of the Orr and resonance mechanisms explains the selection between the $m = 1, 2, 3$ modes shown in figure 4.1. It is speculated that increasing m dominates short-term because the Orr mechanism works more efficiently with numerous spirals. However long-term

the induction mechanism plays a dominant role and it appears that this it is more appropriate for the $m = 1$ symmetry, most likely because the displacement mode that is selected in this way is less prone to viscous diffusion than modes of higher m. An example of a combination of the two mechanisms is given in figure 4.4 for a time where the $m = 1$ mode is optimal, namely $T = 7$ at $Re = 5000$. The initial spirals (figure 4.4(b)) unravel and a displacement mode is induced simultaneously within the core. Long-term the perturbation decay is much slower ($O(Re^{0.6})$ as noted previously) than for the previous example as the displacement mode is only extinguished through viscous diffusion. The external perturbation undergoes the shear-diffusion process in the form of negative-tilt spirals while the core mode prevails (figure 4.4(d)).

4.3.2 Nonlinear optimal perturbations

In this section the nonlinear optimal perturbations of a Lamb-Oseen vortex are described and analysed. First, it is necessary to validate the optimisation tool in the nonlinear domain.

Validation of the nonlinear optimisation tool

The only nonlinear optimisation results on a LO vortex with which to validate our method is the PhD work of Bisanti [13]. The work in question is briefly summarised here.

Bisanti determined the $m = 2$ two-dimensional linear and nonlinear optimal perturbations of a Lamb-Oseen vortex using a very similar gradient-based optimisation method as the one used for the present investigation. The choice of azimuthal wavenumber $m = 2$ was based on a conjectured potential for an unstable scenario triggered by the nonlinear terms as the elliptical deformation induced temporarily by the $m = 2$ closely resembles the case of a vortex in an external strain field. It has been shown [8, 63, 95] that a vortex submitted to an external strain field of sufficient amplitude can induce transition to a quasi-steady tripolar state. In order to investigate specifically the $m = 2$ problem, Bisanti chose a time horizon where the linear $m = 2$ mode is dominant, namely $T = 4.8$ at $Re = 5000$. To avoid the emergence of other azimuthal modes due to nonlinear interactions, the results were filtered by imposing $m = 2$ symmetry at the end of each adjoint integration. No such filter is used to reproduce Bisanti's results, as it is found that using the linear optimal perturbation to initialise the nonlinear optimisation leads to a preliminary convergence towards the desired result.

The nonlinear optimisation method is in fact highly dependent on the initial guess. The quality of the initial guess has a strong impact on the number of iterations to convergence which can be of the order of several hundreds for nonlinear optimisations. In the interest of hastening the process, it would seem practical to use the linear optimal perturbation as an initial guess. For small initial energies we expect to retrieve a similar optimal perturbation so starting from the linear optimal leads to rapid convergence. To illustrate we show the convergence graphs for the LO vortex optimisation ($T = 4.8$, $Re = 5000$) in figure 4.6(a). The optimisations were initialised with the linear optimal. Convergence is considered to be reached when the variation of the gain defined as $J = \left(G(T)^i - G(T)^{i-1}\right)/G(T)^i$ (with the notation i referring to the iteration number) attains values inferior to 10^{-6} (see figure 4.6(b)).

The nonlinear optimisations with small initial energy $\left(E_0 \leq 10^{-3}\right)$ converge within ten iterations, as is the case in the linear framework. However the case $E_0 = 10^{-2}$ appears to converge after 30 iterations (point **A**) and then experiences considerable growth to reach a much higher value after more than 200 iterations (point **B**). The first convergence plateau corresponds exactly to the $m = 2$ nonlinear perturbation described by Bisanti as the optimal. This suboptimal perturbation acts as an attractor for the optimisation process. Figure 4.7 shows the perturbation energy growth (solid line) and the corresponding vorticity contours of the $m = 2$ suboptimal. The gain at the horizon time $G(T) = 89$ is lower than the linear optimal gain (the linear evolution is recalled here as a dashed line). At later times the energy does not decay as in the linear case but undergoes a subcritical bypass and reaches a quasi-

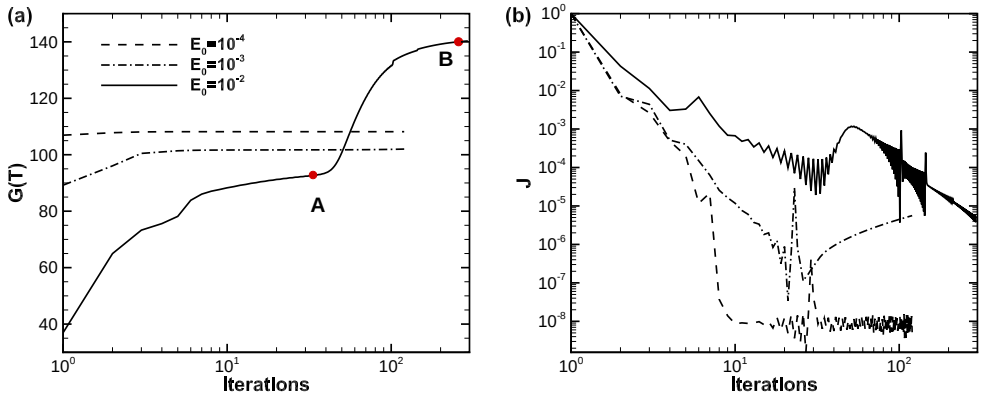

Figure 4.6: (a) Evolution of the nonlinear perturbation energy gain $G(T)$ for $T = 4.8$ throughout the optimisation process for initial energy E_0 when the initial guess is the linear optimal perturbation; (b) corresponding gain variation J. Label **A** is the suboptimal solution and label **B** is the true optimal.

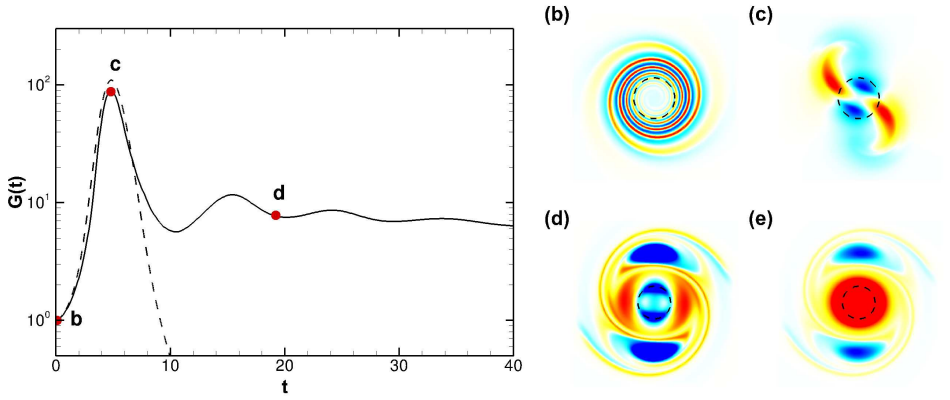

Figure 4.7: Nonlinear perturbation with initial energy $E_0 = 10^{-2}$ obtained in a transitory convergence plateau when the optimisation process is initialised by the linear optimal perturbation. (a) Perturbation energy gain over time (solid line) compared with the linear optimal (dashed line); vorticity contours of the optimal perturbation at times (b) $t = 0$, (c) $t = T$, (d) $t = 4T$. (e) Total vorticity field (base flow and perturbation) at $t = 4T$. The dotted line indicates the vortex dispersion radius.

stable state at around $G = 10$. The perturbation vorticity contours at times $t = 0$, $t = T$, and $t = 4T$ are given in figures 4.7(b)-(d). The suboptimal perturbation at $E_0 = 10^{-2}$ presents much the same shape at $t = 0$ as the linear optimal. The outer extremities are spread slightly further from the core. At $t = T$ the symmetry between positive and negative vorticity is completely broken and this leads to the ejection of two negative satellites outside of the core at $t = 4T$ (see figure 4.7(d). As anticipated by Bisanti, when added to the base flow the perturbation induces a quasi-stable rotating tripole at late times (pictured in figure 4.7(e)). The retrieval of Bisanti's result validates the present optimisation routine in the nonlinear domain, although the perturbation found is evidently not the global optimal for this horizon time.

Nonlinear optimals

In order to avoid attraction to a suboptimal disturbance by the linear optimal and in doing so test the robustness of the optimisation tool, the optimisations were subsequently initialised using a random value velocity field. Figure 4.8 gives the nonlinear optimal gains $G(T)$ attained after complete convergence (see point **B** of figure 4.6) when initialising either from the linear optimal (hollow squares) or the random field

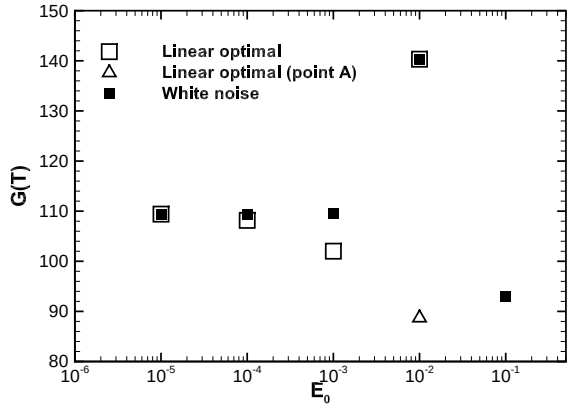

Figure 4.8: Converged nonlinear gains $G(T)$ at $T = 4.8$ for initial energy E_0 initialising the optimisation with the linear optimal or a random velocity field.

E_0	10^{-4}	10^{-3}	10^{-2}
$G(T)$	109	110	140

Table 4.2: Nonlinear optimal gain for varying initial energy E_0 for $T = 4.8$ and $Re = 5000$.

(filled squares). For very small initial energy E_0 the results are the same regardless of the initial guess. However as E_0 grows, the gap between the obtained gains grows. It appears that the linear optimal does in fact form an attractor towards a suboptimal perturbation and only when the initial energy is high enough $\left(E_0 = 10^{-2}\right)$ does the optimisation manage to escape the attractor (represented by a triangle for this initial energy). As a result of this study, all subsequent nonlinear optimisations were initialised using white noise.

Table 4.2 summarizes the nonlinear optimal gains obtained for varying initial energy E_0. A striking result is that contrary to the findings of Bisanti, the nonlinear optimal perturbation can induce considerably greater growth than the linear optimal for $E_0 = 10^{-2}$: $G(T) = 140$ compared with $G(T) = 109$ for the linear case. An approximate optimal initial amplitude is found, which is $E0 = 10^{-2}$ since the larger initial energies tested lead to a lower gain. The nonlinear optimal growth, decay and vorticity contours are given in figure 4.9.

The initial energy at which divergence from the linear optimal gain occurs corresponds to the energy at which the nonlinear terms become active. This threshold has been recognised and analysed for other flows, the boundary layer transition scenario described by Cherubini et al. [20] for example, and named the 'nonlinearity threshold' E_{0th}. For the LO vortex at $Re = 5000$ and $T = 4.8$, the nonlinearity threshold is $E_{0th} \approx 10^{-3}$. As the nonlinearity threshold is crossed, the optimal perturbation undergoes progressive evolution to a very different structure.

Unlike the linear optimal visible in figure 4.2(b), the nonlinear optimal at $E_0 = 10^{-2}$ (see figure 4.9(b)) features two positive spirals and one stronger negative spiral instead of the linear pure $m = 2$ symmetry. When the nonlinear terms are activated, the perturbation spirals not only undergo advection by the base flow, but they also interact with each other through mutual induction. As such, their initial positioning to achieve maximal amplification at time T is impacted. Furthermore the nonlinear optimal modifies the radial profile of the vortex by creating an inflexion point in the circulation and vorticity profiles. In doing so the optimal perturbation makes the vortex unstable to the azimuthal shear instability and, were the vortex 3D, to the centrifugal instability (see Chapter 1 and Gallaire & Chomaz [41]) for further details).

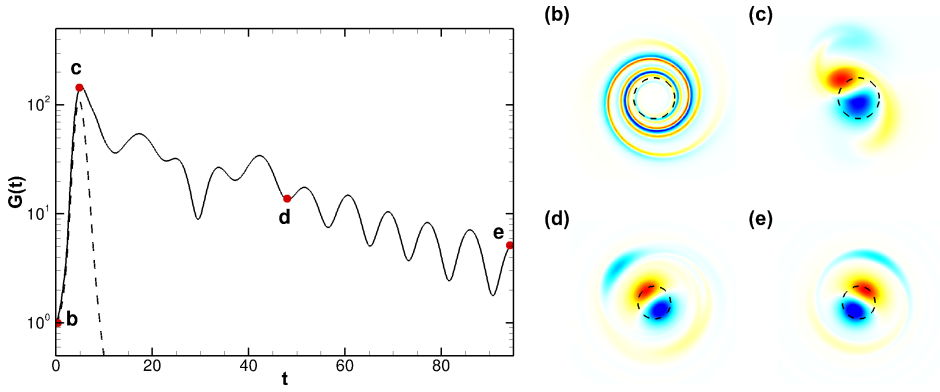

Figure 4.9: (a) Perturbation energy growth (solid line) for the nonlinear optimal perturbation of a LO vortex with initial energy $E_0 = 10^{-2}$ and horizon time $T = 4.8$ at $Re = 5000$ compared with the linear growth (dashed line); corresponding axial vorticity ω contours at times (b) $t = 0$, (c) $t = T$, (d) $t = 10T$ and (e) $t = 20T$. The dotted line indicates the vortex dispersion radius.

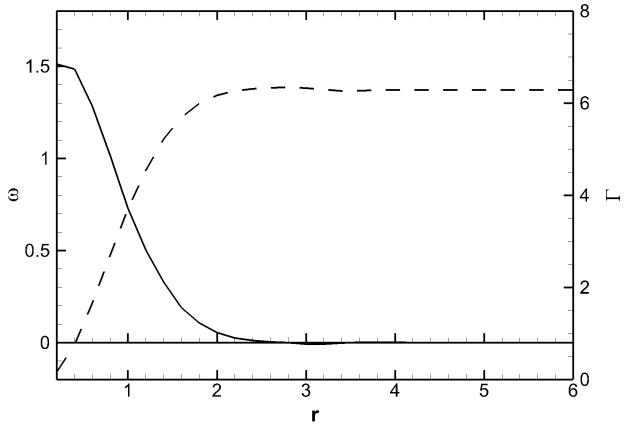

Figure 4.10: Modification of the initial radial distribution of circulation $\Gamma(r)$ and vorticity $\omega(r)$ due to the nonlinear $E_0 = 10^{-2}$ optimal perturbation of a LO vortex at $T = 4.8$ and $Re = 5000$.

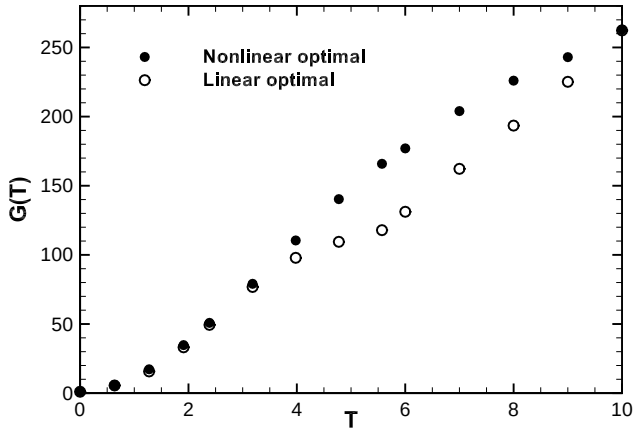

Figure 4.11: Linear and nonlinear $E_0 = 10^{-2}$ optimal gains with varying horizon time T for a LO vortex with $Re = 5000$.

The evolution of the nonlinear optimal is composed of several stages apparent in figure 4.9(a). Between the time stamps **c** and **d**, it appears that the various azimuthal components composing the initial disturbance compete against each other as the spirals unravel. After **d** $m = 1$ modes finally dominate the dynamics, with a displacement mode emerging within the core. During the competition period, a negative vorticity satellite is ejected (see 4.9(d)) which creates a quasi-stable, oscillatory state after the time stamp **d**. The quasi-periodic oscillations in kinetic energy observed after **d** correspond to the coupled rotation of the satellite and displacement mode at a frequency $f \approx 0.1\tau^{-1}$. The energy does not decrease sharply but remains in a high energy oscillatory state which lasts for over 180 rotation times (see § 4.4).

General examination of the nonlinear optimal perturbations

The nonlinear optimal of the LO vortex generates greater growth than the linear optimal for the horizon time $T = 4.8$. The nonlinear optimal gains for perturbations of initial energy $E_0 = 10^{-2}$ have been determined for horizon times up to 10 rotation periods and are given in figure 4.11. The linear optimal gain curve corresponds to the envelope of the individual linear gains of figure 4.1. At small horizon times the nonlinear optimal induces approximately the same gain as the linear optimal. The nonlinear optimal perturbations are generally a mixture of $m = 2$ and $m = 3$ modes as these are the dominant, almost undistinguishable, linear modes at short times. However when $T \in [3 - 5.4]$, although the linear optimal mode is $m = 2$, the nonlinear $E_0 = 10^{-2}$ optimal perturbation is composed of a combination of several azimuthal modes and eventually induces a displacement mode $m = 1$ within the vortex core. It is also from this time ($T = 3$) that the nonlinear gain becomes greater than the linear gain. This remains the case up to $T = 9.5$ and the maximum gap between linear and nonlinear gain is of 40.6% of the linear gain and occurs at $T = 5.6$.

An interesting observation concerning this result is that while the linear perturbation is optimal at short times, which can be anticipated as the linear dynamics gives the immediate evolution of the flow dynamics, it is overwhelmed by the nonlinear optimal at intermediate time indicating that linear optimals are not always dominant.

As an analysis of the cause for the greater growth induced by nonlinearities in the time range $T \in [3 - 9.5]$, at first it must be noted that energy growth in the nonlinear framework still relies on relation 4.13. In this respect the spirals of the nonlinear optimal much resemble that of the linear optimal and are expected to generate similar gain through the Orr mechanism. The largest difference comes

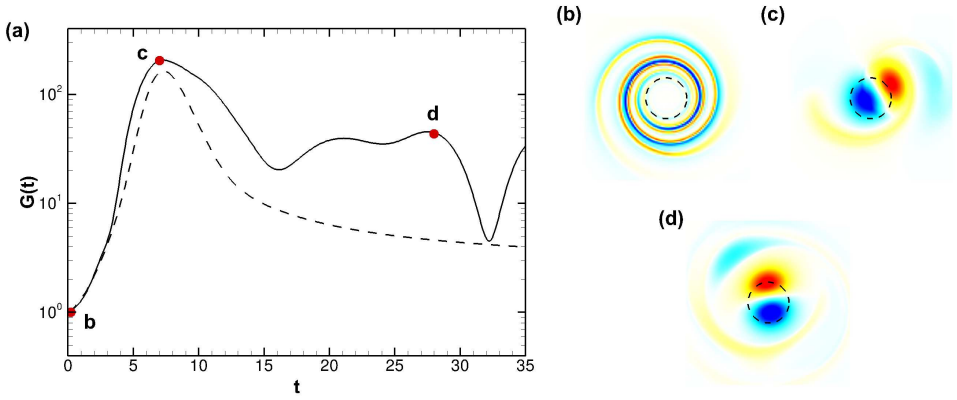

Figure 4.12: (a) Perturbation energy growth (solid line) for the nonlinear optimal perturbation of a LO vortex with initial energy $E_0 = 10^{-2}$ and horizon time $T = 7$ at $Re = 5000$ compared with the linear growth (dashed line); corresponding axial vorticity ω contours at times (b) $t = 0$, (c) $t = T$, (d) $t = 4T$. The dotted line indicates the vortex dispersion radius.

	$u_v^2(T)/u_v^2(0)$
Linear optimal	25.4
Nonlinear optimal	86.9

Table 4.3: Contribution of the vortex displacement to the energy gain for the linear and nonlinear $E_0 = 10^{-2}$ optimal perturbations at $T = 7$ and $Re = 5000$.

from the initial organisation of the perturbation. The nonlinear optimal (see figure 4.9(b)) has asymmetric spirals (as opposed to symmetric spirals) which favour a precipitated boost of the linear $m = 1$ mode through the induction term of the linearised Helmholtz equation 4.14. In fact it can be observed that the nonlinear $E_0 = 10^{-2}$ optimal favours an earlier appearance of the displacement mode in the vortex core. As such the nonlinear optimal generates increased vortex displacement compared with the linear flow.

Returning to the nonlinear and linear gains as functions of T (figure 4.11) a final comment is that the linear gain becomes dominant over the nonlinear gain after approximately $T = 10$.

4.4 Evolution of the optimal perturbation after the horizon time, quasi-steady state

To appreciate the effect of the nonlinear optimal perturbation on the LO vortex, the evolution of the total flow (vortex and optimal perturbation) for the optimal at $T = 4.8$ and $Re = 5000$ up to $t = 4T$ is observed. Axial vorticity contours of the perturbed vortex evolving in time are given in figure 4.13. Initially the vortex is surrounded by positive-tilt vorticity spirals as shown in 4.13(a). As described previously the spirals unravel and thicken under the effect of the differential rotation of the vortex. The positive spirals merge with the primary vortex core to form an elliptical vortex with negative-tilt arms, whereas the negative spiral rolls into an elliptical vorticity patch which is ejected from the vortex (see 4.13(c)). At later times, the negative-tilt positive vorticity spirals continue to wrap around the primary vortex and grow thinner and weaken through viscous diffusion. The negative satellite remains intact and orbits the primary vortex which is displaced around its steady state position by the displacement mode (d) – (f).

It is found that the satellite rotates at $\omega \simeq 0.1$ and that for its radial location r_s the rotational speed of the base flow is $\Omega(r_s) \simeq 0.1$. It can be inferred that the satellite vorticity is formed within a critical

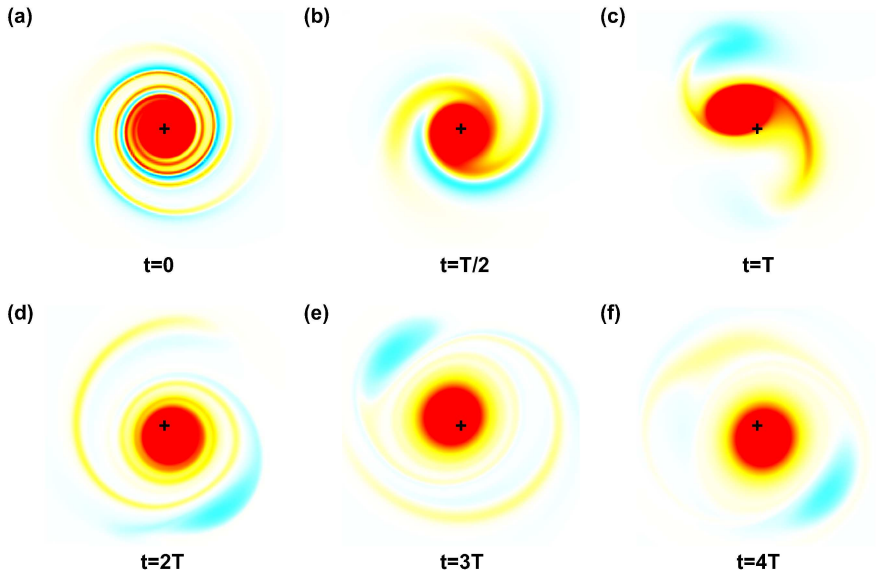

Figure 4.13: Axial vorticity contours depicting the DNS of the complete flow: LO vortex and corresponding nonlinear optimal perturbation $E_0 = 10^{-2}$ for $T = 4.8$. The cross indicates the initial position of the primary vortex $(0, 0)$.

layer. Given the amplitude of the perturbation, we speculate that this is a nonlinear critical layer such as those described by Le Dizès [57], which could explain why it can maintain itself without deterioration on a much longer time scale than its viscous and linear counterpart. This qualitative analysis suggests that the activation of a critical layer allows a permanent displacement of the vortex core by induction resulting in a quasi-steady non-axisymmetric state.

To illustrate the substantial movement of the vortex core, the trajectories of the primary vortex and the satellite are mapped in figure 4.14(a). The positions of the satellite and the primary vortex centroids are taken to be the barycentre of the negative (resp. positive) vorticity. A cut-off at 10% of the maximum (resp. minimum) vorticity value allows us to distinguish between the primary and secondary vortex and to neglect the filamentation. The ejection of the satellite from the primary vortex can be visualised clearly in figure 4.14(a). The evolution of the satellite radial position R_2 is given in figure 4.14(b). The ejection is relatively fast: the centroid reaches its average position $R_2 \approx 3$ after approximately 6 rotation periods (time stamp **b**). From $t \geq 50$ the satellite radial position oscillates at the same frequency as the perturbation energy oscillations in figure 4.9(a). However the distance separating the satellite and the primary vortex d does not present these oscillations, so it is the position of the whole structure that oscillates and not just the satellite.

Eventually after more than 200 vortex rotation times (not shown), the perturbations become sufficiently weak to be cancelled out by viscosity and the primary vortex returns to its original position. The eventual return of the primary vortex to an axisymmetric steady state appears to be inevitable, even for optimal perturbations of still higher initial perturbation energy. The dynamics of a vortex disturbed by the $E_0 = 10^{-1}$ nonlinear optimal is shown in figure 4.15. Three satellites are generated, two negative and one positive, to create a pair of vortex dipoles interacting and generating considerable motion. The primary vortex appears ultimately to return to its steady state position and the satellites diffuse. Although weakened by the interaction, the primary vortex retrieves a Gaussian profile of maximum vorticity $\Omega_0\,(t = 5T) = 0.92\Omega_0(t = 0)$ and circulation $\Gamma\,(t = 5T) = 0.78\Gamma(t = 0)$ which are both surprisingly high given the strong deformations sustained during the previous evolution.

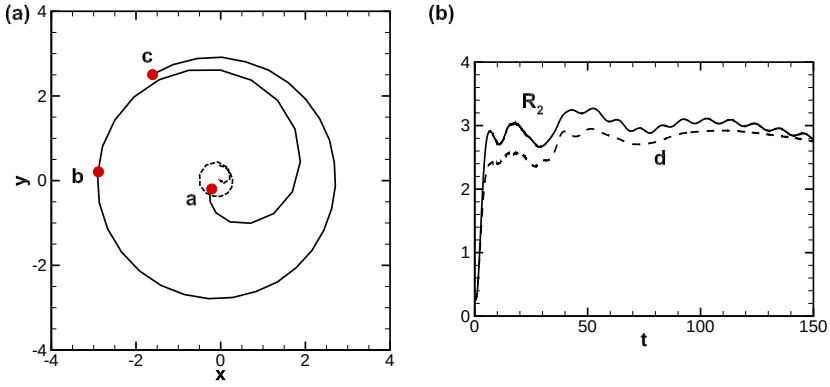

Figure 4.14: (a) Spatial tracking of the centres of the primary vortex (dashed line) and the satellite (solid line) during the ejection phase; (b) Long-term evolution of the radial position R_2 of the satellite and the distance between the satellite and primary vortex centroids d.

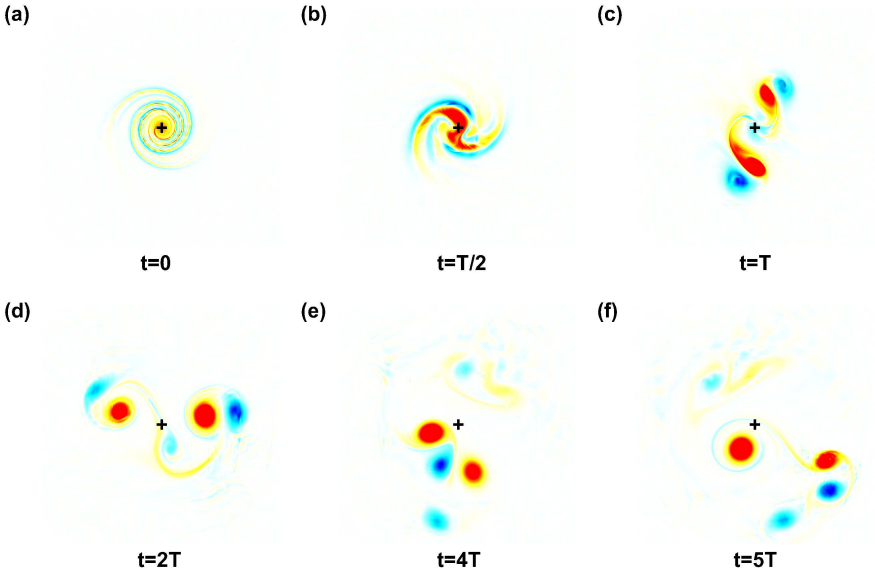

Figure 4.15: Axial vorticity contours depicting the DNS of the complete flow: LO vortex and corresponding nonlinear $E_0 = 10^{-1}$ optimal perturbation. The cross indicates the initial position of the primary vortex $(0, 0)$.

	Frozen base flow	Diffusing base flow
Linear	109.43	109.41
Nonlinear $E_0 = 10^{-2}$	140.32	139.78

Table 4.4: Linear and nonlinear $E_0 = 10^{-2}$ optimal gains $G(T)$ obtained for a LO vortex at $Re = 5000$, with $T = 4.8$ using a frozen base flow and a diffusing base flow.

4.5 Conclusion

The long-term linear optimal perturbation is the $m = 1$ displacement mode which temporarily generates a displacement mode in the vortex core. Linear optimal growth is achieved through the Orr mechanism, but growth is limited by the natural arrest caused by differential rotation by the base flow. The effect of the nonlinear optimal is to accelerate the intervention of the $m = 1$ mode in the vortex core, thanks to a suspected nonlinear critical layer dynamics. The resulting growth is considerably greater and the vortex transitions to a rotating quasi-stable state surrounded by one or several secondary vortices depending on the initial perturbation energy.

The displacement of the vortex by the nonlinear optimal perturbation is reminiscent of vortex meandering, a low frequency motion observed in aircraft trailing vortices. Recent studies have shown that this phenomenon is likely to be the effect of an instability of the vortex [30]. Applying the nonlinear optimisation technique to a three-dimensional vortex may well throw more light on this problem. Moreover, the perturbation can create a circulation overshoot outside the vortex core. Although in 2D this has no effect on the subsequent dynamics of the flow, in 3D these conditions would lead to a centrifugal instability. Both of these observations are great motivation for applying the optimisation technique to 3D vortices and even multi-vortex systems.

A. Validation of the frozen base flow approach

In this paragraph, we intend to demonstrate the validity of the frozen base flow approach within the linear and nonlinear optimisation process. The case of the LO vortex with $Re = 5000$ and $T = 4.8$ is used as an illustration. The optimal gain $G(T)$ obtained for the linear and nonlinear $E_0 = 10^{-2}$ cases are compared in table 4.4 for a frozen and a diffusing base flow. It is clear that the approach is valid as there is less than 0.5% difference between the values. The optimal perturbation vorticity contours, although not shown here, are indistinguishable.

The fact that the gain achieved using a diffusing base flow is slightly lower than that obtained using a frozen base flow can be expected as the effect of viscosity is to weaken the vortex strength and therefore diminish the azimuthal velocity. As perturbation growth is directly dependent on the azimuthal velocity, its value is also impacted.

Chapter 5

Effect of the vortex structure on the optimal perturbation

It is well known that all vortices with an axisymmetric smooth vorticity profile will eventually relax through viscous diffusion to a Gaussian profile such as the Lamb-Oseen (LO) vortex model used throughout the thesis. However as the diffusion process acts on the viscous timescale $O(Re)$ it is legitimate to investigate the dynamics of short-term perturbations on vortices with smooth but sharper profiles than the LO vortex. Moreover, Pradeep & Hussain [80] established that the linear perturbation growth mechanism through strain (the Orr-type mechanism) depends directly on the balance between solid-body rotation and shear stress. By varying the vortex vorticity profile, this balance can be greatly modified so the structure of the vortex core could have a considerable impact on the form and efficiency of the linear and nonlinear optimal perturbations. In addition, Le Dizès [57] showed that the vorticity profile can strongly influence the survival of non-axisymmetry in isolated vortices owing to variations of the nonlinear critical layer. This may further encourage the appearance of persistant non-axisymmetric states such as those reached by the nonlinear optimal perturbation of the LO vortex. In this chapter we propose to apply the linear and nonlinear optimisation methods presented in Chapter 2 to sharper two-dimensional vorticity profiles and compare the results with those obtained for the LO vortex in Chapter 4.

5.1 Definition of the base flow

The base flow is still an isolated vortex of circulation Γ and dispersion radius a. Results are rendered non-dimensional using $a = 1$ and $\Gamma = 2\pi$. The Reynolds number remains $Re = \Gamma/(2\pi\nu) = 5000$. We generate a family of smooth vortices with a sharper velocity profile by diffusing a Rankine vortex (see Chapter 1 for a description of the Rankine vortex model) over limited periods of time. The longer the diffusion period, the closer the profile will get to the LO model. Two profiles in particular are retained by letting a Rankine vortex diffuse at $Re = 5000$ over 8 rotation times ($\tau = 4\pi^2 a^2/\Gamma = 2\pi$) and 40 rotation times respectively. We designate these profiles 'R+8' and 'R+40' to clarify the discussion. Note that in his study of the influence of vorticity profiles on vortex dynamics, Le Dizès [57] considered a family of vorticity profiles parametrised by the following:

$$\begin{cases} \Omega(r) = 1 & r < a \\ \Omega(r) = exp\left(-\frac{(r-a)^2}{(1-a)^2}\right) & r \geq a \end{cases} \tag{5.1}$$

with Ω the base flow axial vorticity.

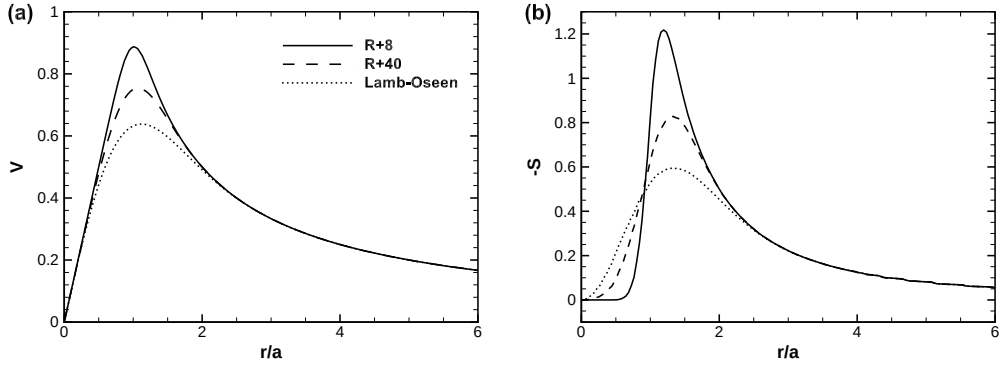

Figure 5.1: (a) Azimuthal velocity profile of three vortices : a Rankine vortex diffused over 8 rotation times and 40 rotation times, and a LO vortex; (b) radial strain profile for the three vortices.

The original Rankine vortex profile is not used for the optimisation to avoid the complication posed by the discontinuous vorticity and strain profiles. The azimuthal velocity profiles used for this study are shown in figure 5.1(a), giving three vortices of decreasing solid-body rotation core size, having the same circulation Γ. The velocity profile of the LO model is $V = \Gamma/(2\pi r)\left(1 - e^{-r^2/a^2}\right)$. The perturbation kinetic energy growth is directly related to the base flow strain as shown by Pradeep & Hussain [80]:

$$\frac{dE}{dt} = -\int_V uvr\partial_r\left(V/r\right)dV \tag{5.2}$$

The strain $S = r\partial_r\left(V/r\right)$ of each vortex is shown in figure 5.1(b). As expected, the vortex structure clearly has a strong effect on the strain distribution and amplitude. When the profile is sharpest, the radial extent of the solid-body rotation is larger and therefore the zone of minimum strain within the core is wider. Also the sharper the profile, the greater the maximum value of strain: the maximum strain for the $R+8$ profile is more than twice the maximum strain of the LO profile.

Once again the simulations are carried out using Nek5000 [38]. The computational domain and mesh are the same as those described in Chapter 4 and elements of validation are given in Chapter 2.

5.2 Optimal perturbations for varying vortex structure

To compare these results effectively with those of the LO vortex of Chapter 4, the analysis is carried out at $Re = 5000$ and for the time horizon $T = 4.8$. Note that in this situation, the linear optimal of the LO vortex is an $m = 2$ azimuthal perturbation.

5.2.1 Linear optimal perturbations

Figure 5.2 displays the radial distribution of axial vorticity ω at $\theta = 0$ for (a) the linear optimal perturbation and (b) the resulting mode at $t = T$ for each vortex. The optimal perturbation is composed of vorticity spirals situated on the outskirts of the vortex core.

It is clear from figure 5.2(a) that as the base flow velocity profile becomes sharper, not only does the optimal perturbation move closer to the vortex core but also it is concentrated on a much thinner radial interval. This is confirmed by calculating the average radial position $\bar{r}$ and extent $\bar{dr}$ of the perturbation

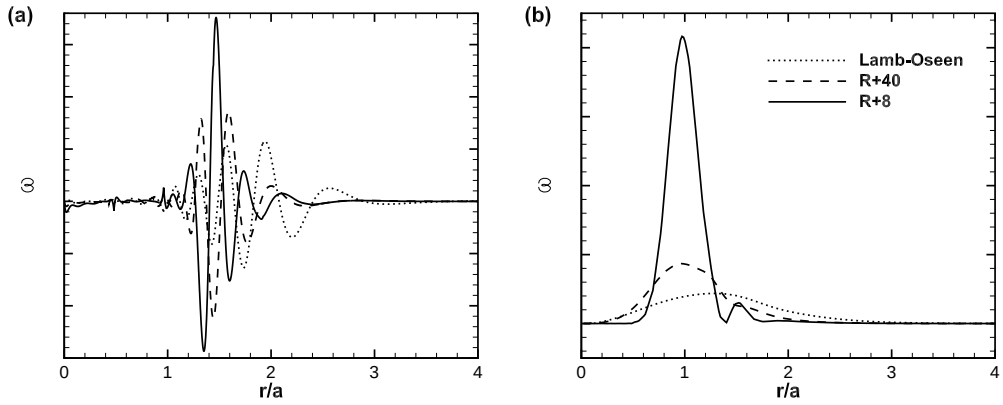

Figure 5.2: Radial distribution of axial vorticity ω of (a) the linear optimal perturbation, corresponding to an $m = 2$ perturbation and (b) the resulting mode at the horizon time $t = T = 4.8$ for the three vortices, $Re = 5000$. The scale for ω is identical for all cases.

	LO	$R+40$	$R+8$
$\bar{r}$	1.85	1.54	1.46
$\bar{dr}$	0.40	0.24	0.21

Table 5.1: Average radial position $\bar{r}$ and extent $\bar{dr}$ of the perturbation vorticity of the linear optimal perturbation of the $R+8$, $R+40$ and LO vortices for $T = 4.8$ and $Re = 5000$.

vorticity for each vortex using

$$\bar{r} = \frac{\int r|\omega|dr}{\int |\omega|dr} \tag{5.3}$$

$$\bar{dr} = \frac{\int |\omega||r-\bar{r}|dr}{\int |\omega|dr} \tag{5.4}$$

The results given in table 5.1 show a reduction by half of the extent of the initial perturbation between the LO and the R+8 vortices, and a 20% increase in core proximity. These differences in the shape and position of the optimal perturbation are directly related to the radial strain profiles of figure 5.1(b). To maximise growth the optimal perturbation is positioned in the area of maximum strain. As the strain peak narrows for sharper profiles, the optimal perturbation is concentrated on a slimmer radial extent. With diffusion the region of solid body-rotating core narrows, and the strain reaches further into the vortex core. This explains the presence of perturbation vorticity inside the core for the LO and $R+40$ cases whereas it is located at the edge in the $R+8$ case (see figure 5.2(b)).

A result of the perturbation being concentrated on a slimmer radial extent for sharper profiles is that the initial perturbation amplitude is far greater. This directly impacts the optimal gain attained at the horizon time $t = T$. Whereas the linear optimal gain at $T = 4.8$ of the LO vortex is equal to $G(T) = 109$, that of the $R+40$ is greater: $G(T) = 199$ and that of the $R+8$ vortex even more: $G(T) = 640$. Sharper vortices promote larger transient growth which may be of interest for practical considerations. Concerning the wake vortex application, in order to diminish the roll effect of trailing vortices on oncoming aircraft it has been assumed that the vorticity should be spread over as wide a radial extent as possible. These results suggest that contrary to the above reasoning, sharpening the trailing vortices would amplify perturbation growth and therefore hasten vortex breakdown.

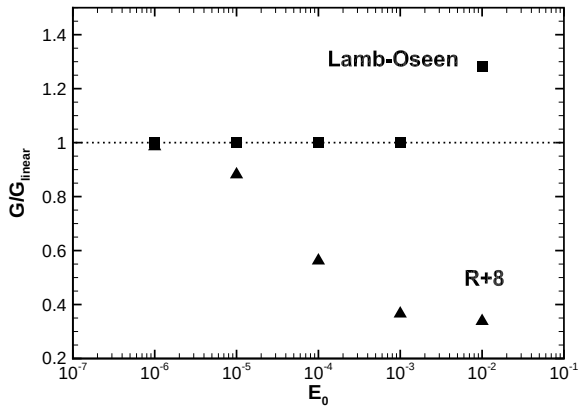

Figure 5.3: Nonlinear optimal gain with respect to the linear gain of the LO and $R+8$ vortices at $T = 4.8$ and $Re = 5000$ for varying initial energy E_0.

	$T = 3.2$	$T = 6.4$
Linear	482	578
$E_0 = 10^{-2}$	205	308

Table 5.2: Linear and nonlinear $E_0 = 10^{-2}$ optimal gain $G(T)$ for the $R + 8$ vortex at $Re = 5000$ at different horizon times T.

5.2.2 Nonlinear optimal perturbations

Having observed the strong dependence of the linear optimal perturbation on the vortex shape, nonlinear optimisation is carried out on the $R + 8$ profile. Figure 5.3 shows the nonlinear optimal gains obtained with varying initial energy E_0 for the $R + 8$ and the LO vortices. For very small E_0 (10^{-4}) the linear gain is retrieved and as E_0 grows the gain diverges from the linear value for both vortices. The initial energy at which divergence occurs corresponds to the energy at which the nonlinear terms reach an amplitude sufficient to modify the flow. This threshold has been recognised and analysed for other flows, the boundary layer transition scenario described by Cherubini et al. [20] for example, and named the 'nonlinearity threshold' E_{0th}. In the case of the isolated vortex, it is clear from figure 5.3 that the value of the nonlinearity threshold varies greatly for different vortex structures. The threshold is much lower for the $R + 8$ vortex ($E_{0th} = O\left(10^{-6}\right)$) than in the LO case ($E_{0th} = O\left(10^{-4}\right)$). The lower threshold observed for the sharper vorticity profiles is related to the associated higher radial concentration of the initial perturbation, which generates more intense levels of perturbation for a given level of initial energy. Nonlinear effects are therefore precipitated for these profiles compared with profiles having perturbations over a larger extent.

The most remarkable result is that whereas the LO nonlinear gain becomes greater than the linear gain (40% higher for $E_0 = 10^{-2}$), this is not the case for the $R + 8$ vortex. The nonlinear $R + 8$ gain drops rapidly with growing E_0 until seemingly reaching a constant value of approximately 35% of the linear gain at $E_0 = 10^{-2}$. The nonlinear optimal perturbation of the $R + 8$ profile at this particular horizon time is therefore less effective than the linear optimal. To confirm that this property is general and not just restricted to this particular horizon time, linear and nonlinear gains for the $R + 8$ vortex at different horizon times are given in table 5.2. In all cases, the nonlinear gain is considerably lower than the linear. In vortices with weaker strain, linear growth is overtaken by nonlinear growth whilst with a stronger strain nonlinear effects do not appear to be as significant.

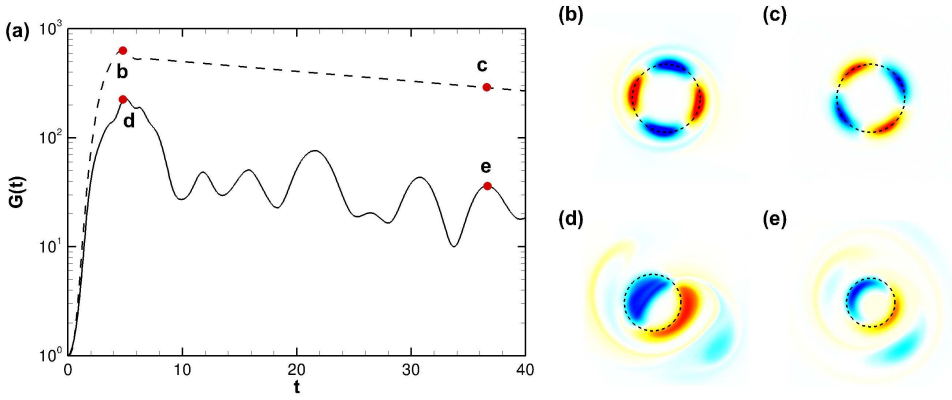

Figure 5.4: Perturbation energy growth over time for the linear and nonlinear $E_0 = 10^{-2}$ optimal perturbation of the $R + 8$ vortex with horizon time $T = 4.8$ at $Re = 5000$; corresponding axial vorticity ω contours at times (b) $t = T$ and (c) $t = 7.6T$ (linear), (d) $t = T$ and (e) $t = 7.6T$ (nonlinear). The dotted line indicates the vortex dispersion radius.

5.2.3 Evolution of the optimal perturbation

Figure 5.4(a) displays the perturbation energy gain evolution induced by the linear and nonlinear $E_0 = 10^{-2}$ optimal perturbations of the $R + 8$ vortex for $Re = 5000$ and $T = 4.8$. As stated previously, the substantially higher strain at the edge of the core leads to much stronger perturbation growth and therefore a much higher gain at $t = T$ than in the LO case. Once the quadripole on the vortex edge is established at $t = T$ (see 5.4(b)) it reaches a quasi-stable state, deforming the perturbed vortex elliptically. As the perturbation vorticity is aligned on a thin radial extent, the differential advection by the base flow is negligible and the perturbation remains unaltered for a considerable time. Very few negative-tilt spirals are formed and diffused, and the rotating perturbation dissipates very slowly through viscous diffusion (see timestamp $\boldsymbol{c}$). This dynamics has a striking resemblance to the persistance of two-dimensional nonaxisymmetric sharp vortices in the inviscid limit described by Dritschel [29]. The possibility for an isolated vortex to sustain an asymmetric state without an external strain has been shown by Le Dizès [57] and results from the presence of a nonlinear critical layer, assuming the perturbation amplitude is sufficient. This behaviour is characterised by the Haberman parameter $h = 1/(Re\epsilon^{3/2})$, with ϵ the perturbation amplitude. Perturbations persist when $h \ll 1$ which is possible for strong enough E_0 and large Reynolds number. One imagines that at higher Reynolds numbers the elliptical perturbation observed here would indeed be maintained indefinitely, as suggested by Le Dizès's theoretical work.

A certain parallel emerges between the nonlinear optimal perturbations of the LO and $R+8$ profiles. After the initial growth up to $t = T$, energy oscillations similar to those of the nonlinear optimal of the LO vortex can be observed. As noted in § 5.2.2 the nonlinear optimal gain reached at $t = T$ is inferior to the linear gain. The $E_0 = 10^{-2}$ optimal perturbation eventually leads to the development of an $m = 1$ mode on the edge of the vortex and the creation of a negative satellite (figures 5.4(d) and (e)). Unlike the LO vortex, no perturbation exists within the vortex core long-term, which suggests the core perturbation is prevented by the well-established solid-body rotation present in the $R + 8$ vortex.

5.3 Conclusion

The vortex structure has been shown to have a considerable effect not only on the shape of the optimal perturbations and the gain they induce, but also on the value of the nonlinearity threshold, that is the initial energy at which nonlinear effects start to influence the flow. For sharper profiles the dominant

perturbation growth mechanism is the Orr mechanism as the base flow strain is stronger than for the Gaussian vortex. The more dominant solid-body rotation prevents perturbations affecting the vortex core. As the vortex approaches a Gaussian profile, the strain is spread over a wider radial extent and perturbations are able to reach into the core. In addition, it is apparent that the sharper the profile, the more likely it is that the perturbed vortex will resist the long-term natural axisymmetrisation process.

Chapter 6

3D Nonlinear optimal perturbations of an isolated vortex

In this chapter the investigation of vortex optimal perturbations is generalised to three-dimensions. The linear optimal perturbations of a Lamb-Oseen vortex have been described previously by Antkowiak & Brancher [2, 3] and Pradeep & Hussain [80] for azimuthal wavenumbers $m = 1$, $m = 0$ and m from 0 to 4 respectively. To our knowledge no 3D nonlinear optimisation work has been carried out on isolated vortices. The 2D nonlinear optimal results of Chapter 4 constituted the first step of our investigation. It should be noted that the extension to the three-dimensional domain presented here is preliminary as neither the computational resources nor the time necessary to carry out this study in depth were available at the time the work was undertaken.

6.1 Numerical method

The base flow is a Lamb-Oseen vortex of azimuthal velocity $V = \Gamma/(2\pi r)(1 - exp(-r^2/a^2))$ with $a = 1$ the vortex dispersion radius and $\Gamma = 2\pi$ the circulation. The Reynolds number is $Re = \Gamma/(2\pi\nu) = 5000$ unless explicitly stated otherwise. The characteristic timescale of the dynamics is the vortex turnover time $\tau = 4\pi^2 a^2/\Gamma = 2\pi$. As is the case throughout this thesis, the base flow is considered to be frozen. A validation of this approach is given in the appendix of Chapter 4.

The incompressible Navier-Stokes equations are solved using Nek5000 [38]. The three-dimensional mesh is cylindrical of maximum radius $R = 15a$ and length $L_z = 2\pi/k$ with ka the non-dimensional axial wavenumber of the perturbation. The transverse mesh details are provided in Chapter 4. In the axial direction the domain is divided into $N_z = 10$ elements, each further discretised by $N_{GLL} = 8$ Gauss-Lobatto-Legendre points. The largest division is $\Delta z_{max}/a \approx 0.1$ with $\Delta z_{max} = \pi L_z/(2(N_{GLL} - 1)N_z$. As in the two-dimensional case, a buffer zone is implemented on the external part of the domain where the kinematic viscosity varies from $\nu = Re^{-1}$ at $r = 12a$ to $\nu = 0.1$ at $r = R$. Zero-velocity Dirichlet conditions are applied at the external boundary $r = R$ and periodic conditions are imposed in the axial direction.

The nonlinear optimisation technique applied to the flow is the same as that used for the two-dimensional study, see Chapter 2 for further details on the method.

6.2 Linear optimal perturbations

In this paragraph the linear optimisation results of Antkowiak & Brancher and Pradeep & Hussain are reproduced in order to have a basis with which the nonlinear optimal perturbations can be compared.

6.2.1 3D linear optimal gains

The finite element linear optimisation tool described in Chapter 2 is applied to obtain a general sweep of the different parameters of the problem: the axial wavenumber k, the azimuthal wavenumber m, the horizon time T and the Reynolds number Re. The linear gains for Reynolds number $Re = 1000$ and $Re = 5000$ and azimuthal wavenumbers $m = 0, 1, 2, 3$ are provided in figures 6.1, 6.2, 6.3 and 6.4 respectively.

First, it is important to note that in the $k = 0$, $m = 0$ case perturbation growth is impossible. Second, for all azimuthal wavenumbers m, as the Reynolds number increases the growth for a given horizon time and axial wavenumber k increases as the linear growth mechanisms (see § 6.2.2 for a brief description) are inviscid.

In the case of axisymmetric perturbations, the gain map appears to contain only one maximum and, as the Reynolds number increases, this maximum shifts to higher wavenumbers and horizon times. At $Re = 1000$ the gain peak occurs at approximately $ka = 0.8$ whereas at $Re = 5000$ the peak is closer to $ka = 1.5$. Reducing the viscous diffusion allows smaller-scale perturbations to contribute to the transient growth. Although at $k = 0$ no transient growth is possible, high gains are reached in the $k \longrightarrow 0$ limit. The horizon time at which these high gains are achieved diverges as $k \longrightarrow 0$. Therefore the perturbation growth rates tend towards zero but as the horizon times are increasingly large, considerable finite amplification can be attained. To summarise, axisymmetric modes can produce significant transient growth but the growth is slow and consequently, in the short term, is often overtaken by the growth of other modes [80].

Regarding perturbations of azimuthal wavenumber $m = 1$, peaks of growth are observed for both $ka = 1.35$ and $k \longrightarrow 0$, independently of the Reynolds number. This was established by Antkowiak & Brancher [2] and corresponds to a resonance phenomenon. Resonance can occur if the external forcing by the perturbation rotates at the same frequency as that associated with a core wave of the vortex. In the linear regime, the perturbations are advected solely by the base flow and therefore frequencies that are most likely to be excited by resonance have values close to the vortex angular velocity. These frequencies coincide mainly with $|m| = 1$ bending modes hence the peaks observed in figure 6.2. The modes contributing to the peak at $ka = 1.35$ correspond to critical layer modes whereas in the $k \longrightarrow 0$ limit a displacement mode is excited (see Antkowiak [1] for further details). For our preliminary 3D investigation, the axial wavenumber $ka = 1.35$ was chosen in order to potentially exploit the resonance mechanism in the nonlinear domain. It will be necessary to explore other axial wavenumbers to complete the analysis.

For $m = 2$ and $m = 3$ perturbations, maximum gain is achieved for short horizon times. As the azimuthal wavenumber grows, the perturbation scales are smaller and are therefore more susceptible to viscous diffusion than modes with $m = 0$ and $m = 1$. This is in accord with the findings of Pradeep & Hussain [80].

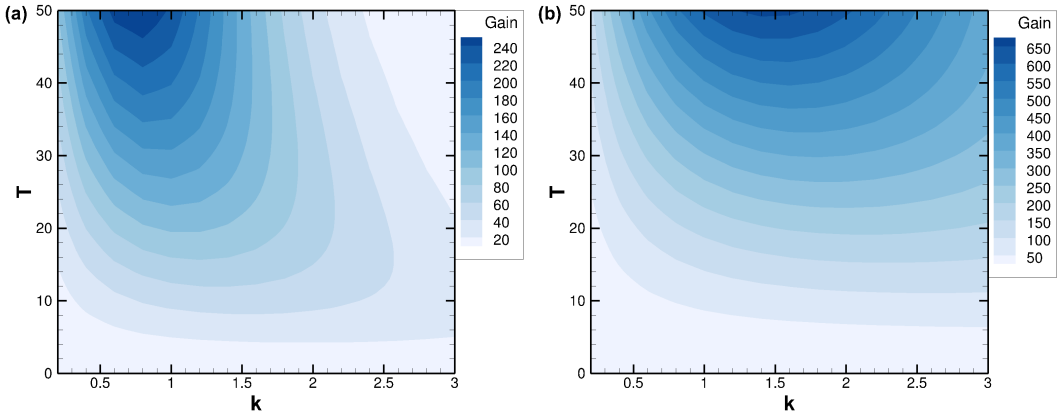

Figure 6.1: Linear optimal gain $G(T)$ for axisymmetric ($m = 0$) perturbations at (a) $Re = 1000$ and (b) $Re = 5000$.

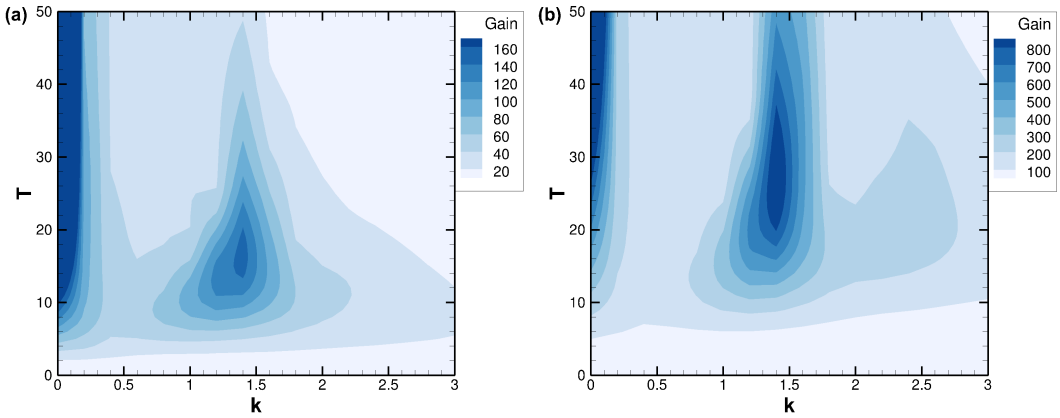

Figure 6.2: Linear optimal gain $G(T)$ for $m = 1$ perturbations at (a) $Re = 1000$ and (b) $Re = 5000$.

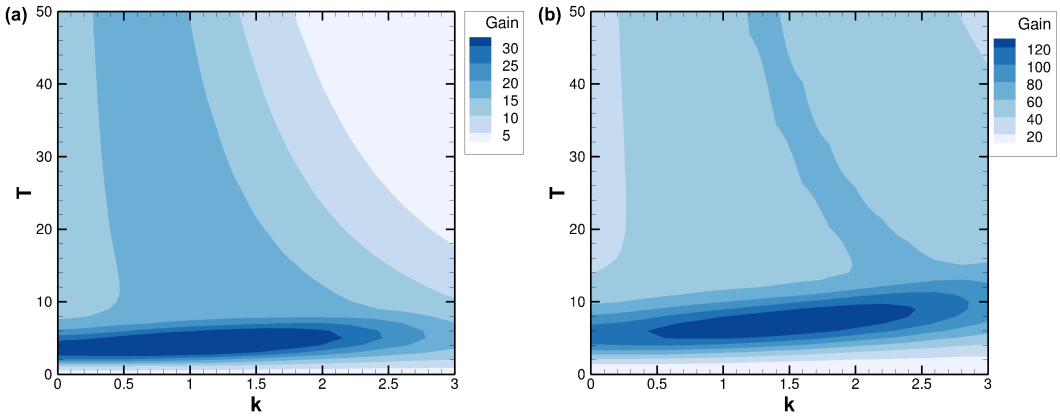

Figure 6.3: Linear optimal gain $G(T)$ for $m = 2$ perturbations at (a) $Re = 1000$ and (b) $Re = 5000$.

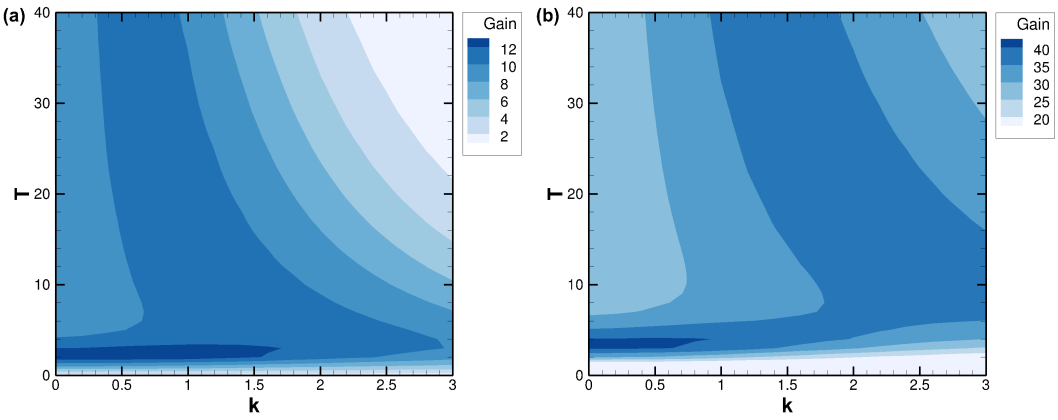

Figure 6.4: Linear optimal gain $G(T)$ for $m = 3$ perturbations at (a) $Re = 1000$ and (b) $Re = 5000$.

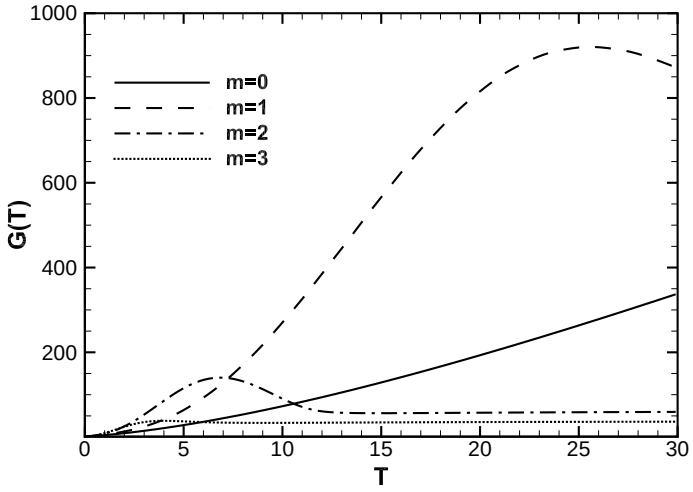

Figure 6.5: Linear optimal gains for $k = 1.35$ and $Re = 5000$.

With axial wavenumber $k = 1.35$ and Reynolds number $Re = 5000$ chosen for this analysis, the linear gains as functions of the horizon time T can be observed for all azimuthal wavenumbers in figure 6.5. In the short term up to $T = 7$, $m = 3$ and $m = 2$ modes dominate the transient growth. Above $T = 7$ the $m = 1$ modes become dominant and generate increasingly greater amplification until approximately $T = 25$ when it starts to decrease. It is clear that although the axisymmetric modes induce weak growth at first, at some large horizon time the $m = 0$ mode will take over from $m = 1$ as the dominant mode.

Figure 6.6 compares the linear 2D and linear 3D $k = 1.35$ optimal gain envelopes. The linear 2D optimal gain envelope was established in Chapter 4. It is interesting to note that at this particular wavelength the 3D gains are very close to the 2D gains, at least for horizon times up to $T = 10$ and at small horizon times 2D modes dominate. For the nonlinear optimisations, in order to ensure the optimal perturbations calculated are purely 3D, the 2D ($k = 0$) component of the flow is therefore removed after each iteration of the optimisation process.

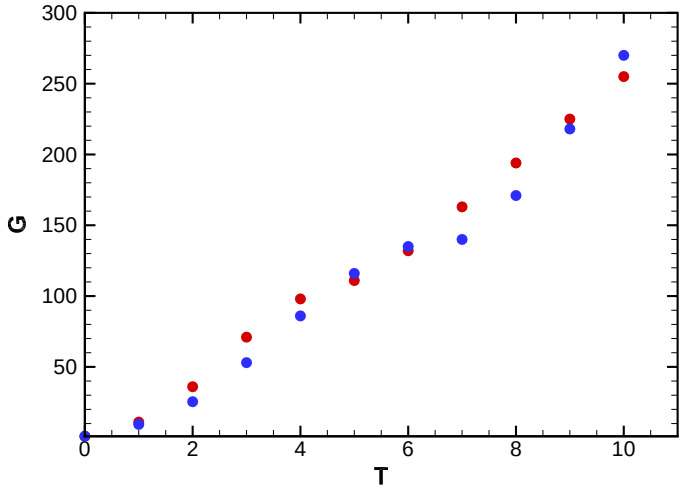

Figure 6.6: 2D (red points) and 3D $k = 1.35$ (blue points) linear optimal gains for increasing horizon time T at $Re = 5000$.

6.2.2 3D linear growth mechanisms

In addition to the 2D linear growth mechanisms described in Chapter 4, that is the Orr-type shear mechanism and the resonance mechanism, a three-dimensional mechanism comes into play. Radial vorticity is tilted and stretched in the azimuthal direction by the vortex strain, generating azimuthal vorticity. Vortex filaments are therefore wrapped azimuthally around the core creating positive Reynolds stress $u'v' > 0$ necessary for perturbation growth. A complete description and analysis of the process is given by Pradeep & Hussain [80].

6.3 Nonlinear optimal perturbations

Owing to the considerable costs in time of nonlinear 3D optimisations there is only limited data available for analysis. The 3D nonlinear optimal perturbations are determined with $ka = 1.35$ for three horizon times $T = 2,\ 4.8,$ and 7. The Reynolds number is $Re = 5000$. At these horizon times the linear optimal perturbation is of azimuthal wavenumber $m = 2$. The nonlinear optimals presented correspond to an initial perturbation amplitude of $E_0 = 10^{-2}$. The choice of initial energy E_0 is based on the extremely interesting results obtained for the two-dimensional case at this energy in Chapter 4.

Figure 6.7 presents the linear and nonlinear energy gain evolutions for all three horizon times. It is clear that for large horizon times, the nonlinear gain at $t = T$ is lower than the linear gain. For $T = 2$ the linear and nonlinear gains are very close. To clarify, the ratio of nonlinear gain over linear gain as a function of the horizon time is given in figure 6.8. A similarity can be observed between these results and those obtained for the 2D case: for short horizon times the linear and nonlinear gains are extremely similar and they diverge for greater horizon times.

For the linear cases after the transient growth period the perturbation energy decreases rapidly through the shear diffusion mechanism (see figure 6.7) returning the vortex to its initial steady state. The long-term behaviour is different for the nonlinear optimal energy growth: quasi-steady states of slowly diminishing perturbation energy take over after the transient growth. For the $T = 2$ optimal the perturbation energy decays to around 1% of its original value E_0, whereas the $T = 4.8$ and $T = 7$ optimals lead to

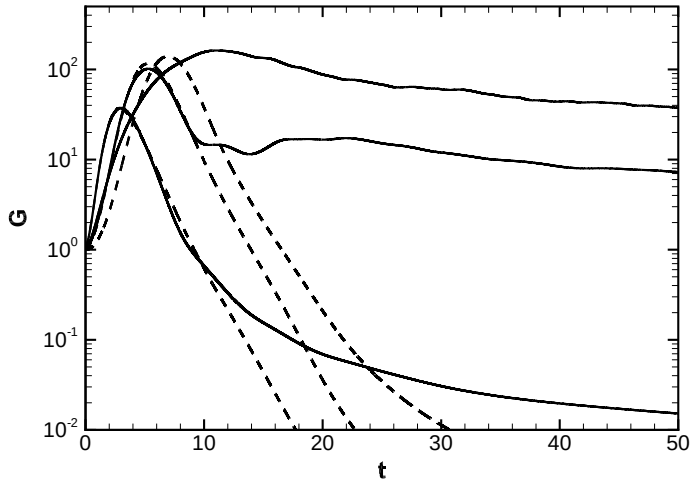

Figure 6.7: Perturbation energy gain evolution induced by the 3D linear (dashed lines) and nonlinear $E_0 = 10^{-2}$ (solid lines) optimals for horizon times $T = 2$, $T = 4.8$, and $T = 7$. $ka = 1.35$ and $Re = 5000$.

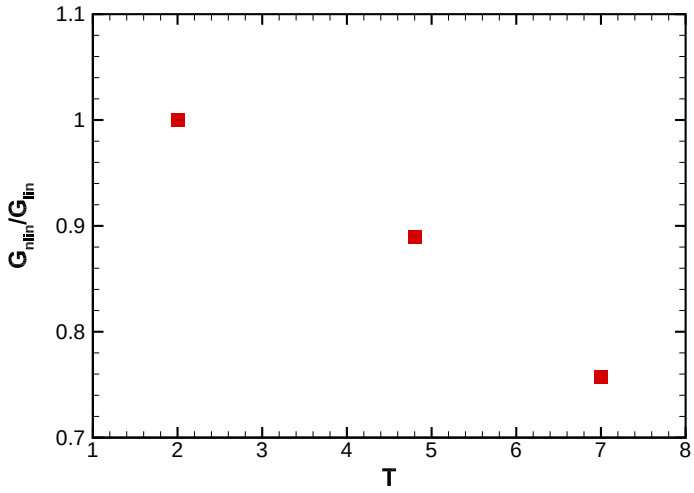

Figure 6.8: Ratio of nonlinear gain over the linear gain

perturbed states with quasi-constant energy levels of approximately 10 and 60 respectively lasting at least 50 rotation times.

The linear and nonlinear optimal perturbations corresponding to $T = 2$ have a very similar shape as is evident in figure 6.9. The initial perturbations present an $m = 2$ symmetry composed of positive-tilt spirals wrapped around the vortex core. As the spirals unravel, an $m = 2$ mode appears at time $t = T$. The similarity between the perturbation shapes is reflected in the coincidence of the linear and nonlinear gains.

Observing the nonlinear optimal perturbation for $T = 4.8$ (figure 6.10(b)) compared with its linear counterpart (figure 6.10(a)), initially it is clear that the nonlinear calculation is not sufficiently resolved

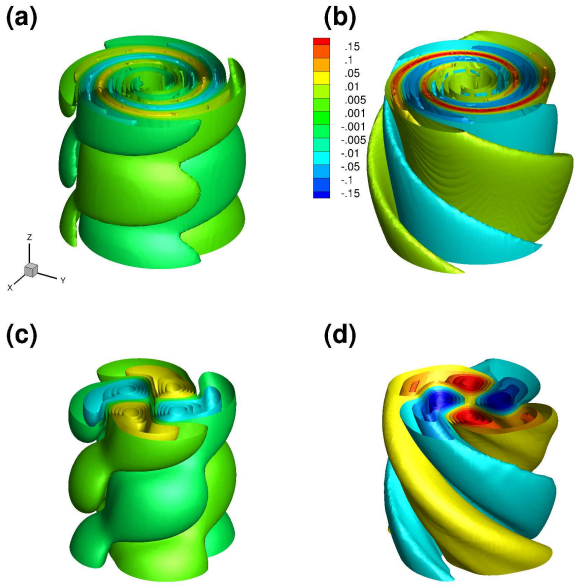

Figure 6.9: Axial vorticity contours of the linear $(a)-(c)$ and nonlinear $(b)-(d)$ optimal perturbations $(a)-(b)$ and the resulting perturbation fields at $t=T$ $((c)-(d)$ with $T=2$, $ka=1.35$ and $Re=5000$. The same contour levels are used for all four perturbation fields.

and therefore they are difficult to compare. Despite this the resulting perturbation at time T (figure $6.10(c)-(d)$) is clearly different in the nonlinear case as there is a noticeable loss of symmetry between the positive and negative perturbation vorticity. This recalls the loss of symmetry observed in the two-dimensional case of Bisanti [13]. It is believed that the veritable optimal perturbation may not have been reached, despite the fact that the convergence error $J=\left(G\left(T\right)^{i}-G\left(T\right)^{i-1}\right)/G\left(T\right)^{i}$ is of the order of 10^{-6}, that was established as a sufficient condition of convergence for the 2D case (see Chapter 4). It is anticipated that pursuing this optimisation will lead to a better-resolved optimal perturbation and possibly therefore a higher optimal gain.

The observations made regarding the convergence of the $T=4.8$ nonlinear optimal calculation can also be applied in the $T=7$ case, as once again the optimal perturbation is poorly resolved (see figure $6.11(b)$). However, it is extremely promising that although the linear optimal at $T=7$ has $m=2$ symmetry, an $m=1$ mode has developed within the core by $t=T$ in the nonlinear case (this can be observed clearly in the axial vorticity contours of figure $6.11(c)$ and (d)). As for the 2D case, the 3D nonlinear optimal involves $m=1$ modes prematurely. Nonetheless, the nonlinear gain reached at $T=7$ is only 75% of that reached through the linear optimal, as established in figure 6.8. Therefore it appears that the nonlinear optimal is less efficient than the linear optimal. Once again however, if the optimisation process is not yet fully converged, it is possible the optimal gain could be greater than that predicted in the present results. Consequently in these cases the optimisation process should be pursued.

Finally, the effect of the $T=7$ nonlinear optimal perturbation on the vortex is presented in figure 6.12. This example is chosen particularly because of the presence of the $m=1$ mode within the vortex core which induces displacement of the core centroid about its steady state position, causing the vortex to bend. As predicted by the gain curves of figure 6.7, the perturbation induces considerable deformation of the vortex for over $10T$ which corresponds to 70 rotation times.

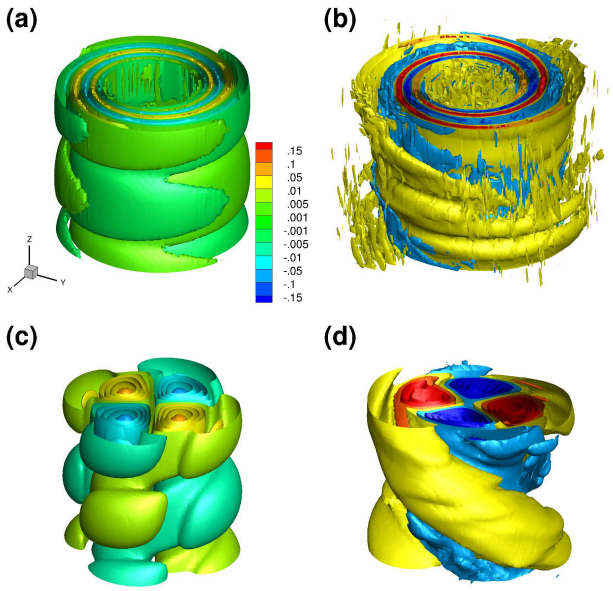

Figure 6.10: Axial vorticity contours of the linear $(a)-(c)$ and nonlinear $(b)-(d)$ optimal perturbations $(a)-(b)$ and the resulting perturbation fields at $t=T$ $((c)-(d)$ with $T=4.8$, $ka=1.35$ and $Re=5000$. The same contour levels are used for all four perturbation fields.

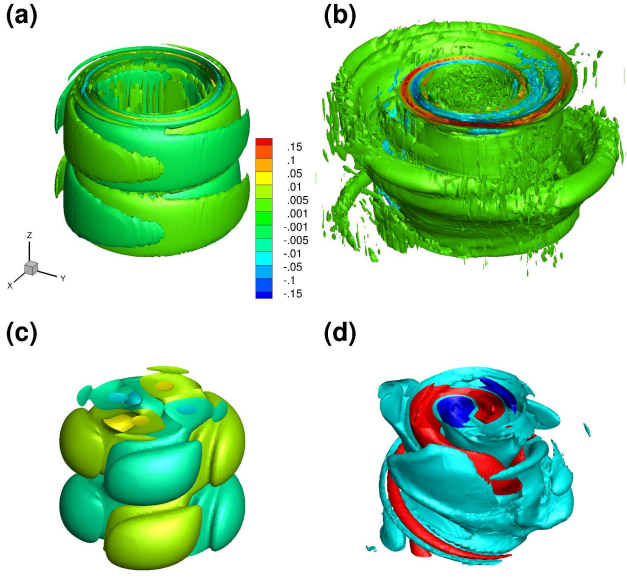

Figure 6.11: Axial vorticity contours of the linear $(a)-(c)$ and nonlinear $(b)-(d)$ optimal perturbations $(a)-(b)$ and the resulting perturbation fields at $t=T$ $((c)-(d)$ with $T=7$, $ka=1.35$ and $Re=5000$. The same contour levels are used for all four perturbation fields.

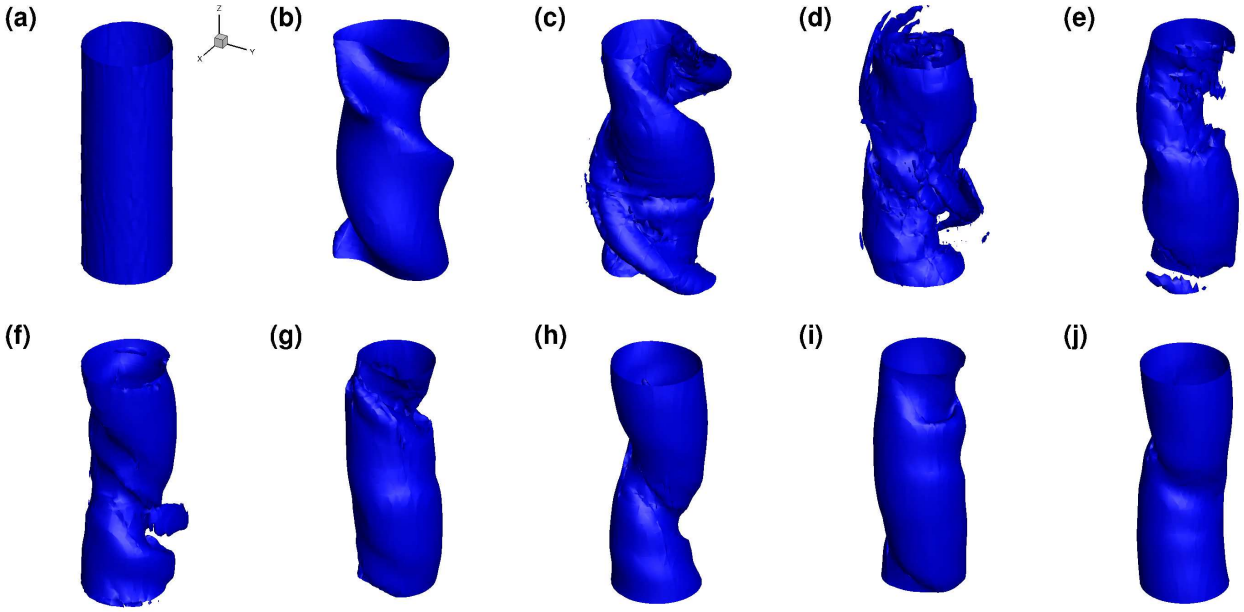

Figure 6.12: Effect of the $T = 7$ nonlinear optimal on a vortex. The axial vorticity contour $\omega_z = .55\omega_z(r = 0, t = 0)$ is followed through time: (a) $t = 0$, (b) $t = T$, (c) $t = 2T$, (d) $t = 3T$, (e) $t = 4T$, (f) $t = 5T$, (g) $t = 6T$, (h) $t = 7T$, (i) $t = 8T$, (j) $t = 10T$. $Re = 5000$, $ka = 1.35$.

6.4 Conclusion

In conclusion, this preliminary study suggests that the 3D nonlinear optimal perturbations induce less perturbation amplification than the 3D linear optimals and, by extension, the 2D nonlinear optimals. However the nonlinear perturbations do retain considerable strength for an extended period of time, preventing the vortex from returning to its steady state.

Analysis of these preliminary results leads to doubts as to the level of convergence of these optimisations and also the quality of the mesh used. As observed in the 2D nonlinear case, the optimisation process could have reached an intermediate convergence plateau and it is possible growth could resume if the calculations were pursued.

Owing to computational and time constraints, this work was restricted to only one axial wavenumber, one Reynolds number and limited horizon times. Investigation of other values of these parameters would shed more light on the nonlinear optimal dynamics.

Chapter 7

Conclusion

Summary and discussion of the main results of this thesis

(a) In calm atmospheric conditions, wake vortices can persist for a remarkably long time in the form of highly stable elliptic vortex rings which undergo periodic oscillations with almost no decrease of the total circulation. Although it is usually overlooked, the danger posed by these rings therefore remains high and, to improve the estimation of the duration of the wake vortex hazard, should be better assessed. Currently this duration is assumed to be equal to the time needed for the disappearance of the fully longitudinal vortex structures that are the only structures that can be measured using Lidar. This period is equal to approximately 5 to 6 characteristic times of the wake (see Spalart [91]). Our findings were obtained by using low Reynolds number simulations but are consistent with higher Reynolds number simulations which indicates a relatively small influence of the Reynolds number. The only limitation to this work is the hypothesis of a homogeneous non-turbulent atmosphere. This restricts the application of our findings essentially to cruising conditions where atmospheric conditions are calm. Aircraft whether landing or at take-off usually encounter high levels of turbulence due to the air motion present in the atmospheric boundary layer and possibly stratification (stratification is also present at higher altitude). This additional disturbance may hasten the destabilisation process, potentially through the optimal mechanism of the Crow instability of which the nonlinear evolution has been described extensively.

(b) The linear optimal perturbation of a counter-rotating vortex pair can halve the vortex lifespan in calm atmospheric conditions if applied with sufficient amplitude (3% of the vortex pair energy). The perturbation generates secondary vorticity around the primary structures that increases the initial deformation of the vortices through induction and accelerates the linking process and subsequent decay of the primary vortices. The amplitude necessary to achieve anticipated decay is very moderate so the use of this perturbation in alleviation strategies is quantitatively conceivable, however the region to disturb between the vortices is so difficult to reach that its use currently is not feasible.

(c) The two-dimensional nonlinear optimal perturbations of an isolated vortex can induce larger transient growth than the linear optimals in the medium term. The nonlinear optimal accelerates the intervention of the $m = 1$ displacement mode to increase kinetic energy by displacing the vortex around its steady state position. For sufficient initial amplitude, the nonlinear optimal induces a bypass transition to a new quasi-steady non-axisymmetric state that decays on the viscous diffusion timescale. This suggests that optimal perturbation could be used to find persistant non-axisymmetric vortex states, as was achieved for example by Le Dizès [57] using critical layer theory, Rossi et al. [82] using an $m = 2$ perturbation to the vortex, Koumoutsakos [53] using an elliptic vortex of increasingly

steep vorticity profile or Turner & Gilbert [95] using an external strain field.

(d) The vorticity profile of a vortex has a strong effect on the shape of the linear and nonlinear optimal perturbations, as well as on the transient growth that can be attained. Whereas the nonlinear optimal of a Gaussian vortex can generate greater transient growth than the linear optimal, it is not the case for sharper profiles. Furthermore, the sharper profiles are shown to resist the axisymmetrisation process more effectively which is in accord with the work of other authors such as Koumoutsakos [53] and Dritschel [29].

(e) Preliminary 3D optimal perturbation results were obtained for the isolated vortex using the nonlinear optimisation tool. The 3D nonlinear optimals appear to generate less perturbation growth than their linear counterparts, but in the long-term lead to persistent high energy states.

Future work

An initial continuation of this work would be a complete description of the 3D nonlinear optimal perturbations, which has only been initiated in this thesis in the case of an isolated Gaussian vortex. While it represents a substantial computational challenge, the large computing facilities currently available should allow some progress in this direction. The next step would be to calculate the nonlinear optimal perturbation of a vortex pair: a configuration fully representative of an aircraft wake in the far-field. Particularly, as observed in the analysis of the nonlinear evolution of the linear optimal Crow perturbation, the amplification process at the hyperbolic points and the nonlinear development of the perturbation around the core should have a considerable part to play. Optimal perturbation results should help to shed light on the potential of these features to hasten turbulence in the flow.

The present study was carried out assuming a homogeneous calm atmosphere. However vortices shed behind aircraft often evolve in a stratified environment which modifies the vortex flow through the exertion of buoyancy forces dependent on the stratification parameter $\bar{N} = N2\pi b^2/\Gamma$ (where N is the Brunt-Vaisala frequency). Although linear perturbation growth in vortex pairs was shown not to be significantly modified when $\bar{N} < 1$ by Ortiz et al. [77], larger values of $\bar{N}$ can have a profound impact on both the base flow and the perturbations through strong baroclinic effects. In particular this is related to the appearance of a strong secondary wake above the primary vortices. For low stratification, the density field inside the vortex pair is nearly homogeneous and the secondary wake is fairly weak, consequently only slight modifications occur to the known homogeneous flow stability results. For stronger stratification, although the density appears to remain essentially constant in the cores of the pair, the vortices are significantly weakened and the secondary wake develops very fine-scale features which are expected to be more unstable. Certainly, applying the nonlinear optimisation tool to such cases would be worthwhile.

Another important field of study, and of direct interest to Air Traffic Management procedures in airports, is the application of the optimal perturbation tool to vortex pairs in ground proximity. The presence of the ground provides interesting possibilities for the application of a control device.

In addition to the wake vortex safety problem, there is another issue related to aircraft wakes that is the formation of contrails and artificial clouds known to have an impact on the climate (see Lee et al. [58]), though current quantitative estimations of the impact are fairly uncertain. Contrails are formed by condensation of the moisture contained in the jet exhausts when thermodynamic conditions are below critical conditions (see the Appleman criterion [4]). In the early phase of the wake development jet exhaust gets trapped inside the vortex system. Wake vortices then procede to transport the resulting ice cloud. Ice particles act as passive tracers, and as such they will follow the subsequent development of the vortex flow. As the particles evolve with the vorticity field, dilution will occur through the deterioration of the wake, that is downwards motion, progressive loss of momentum by viscous shearing and buoyancy forces,

receptivity to external turbulence, instabilities, and nonlinear effects. Assuming the temperature, pressure and moisture conditions are favourable for the persistence of the contrail, the eventual dissipation of the wake momentum, combined with the additional effect of atmospheric phenomena such as wind shear and background turbulence, will lead to a progressive widening of the contrail. Such a diversity of phenomena impacting the evolution of contrails explains the variety of shapes they adopt in the sky. This strong link between vortex dynamics and contrails suggests that by acting on the former, as has been achieved in this thesis, one could affect contrail development. Following the simple model of Appleman [4], the main parameter governing the formation and persistence of contrails, apart from the imposed atmospheric conditions, is the mixing of the jet exhaust with the surrounding air. Accelerating the mixing process should lead to shorter contrail duration and could lower the impact of civil aviation on the climate. Tools such as the one developed in this study could be applied with the objective of optimising this mixing, in the same way as Foures et al. [40] did for the Poiseuille flow.

The generally complicated characteristics of the optimal perturbation analysis results make their application not only difficult but rarely achievable in practical control strategies. One way to circumvent this issue would be to insert some kind of feasibility condition of the initial perturbation in the optimisation constraints. Using the Lagrange multiplier technique, penalisation could be used to achieve this goal. For example, by applying a spatially weighted cost function for the initial control one could impose that the initial perturbation be located in a particular region of space. Although this method could be rewarding, there remains the restriction that, in the context of wake vortices, only the far-field flow has been considered. Specifically the vortex generator, that is the aircraft, and the wake roll-up phase are not included in the model. Control strategies require the presence of at least one surface on which to install the actuation (be it steady or unsteady, passive or active). Evidently whether an optimal forcing of the flow can be performed at the surface of the wing is an open question. The adaptation of the results obtained in this thesis to a practical application (for instance, with a dedicated experiment using a generation device designed to reproduce at best the optimal perturbation) is likely to reduce markedly the efficiency of the control and may even jeopardise it completely. For this reason, an effort should be made towards including the perturbation generator in the calculation of the optimal perturbation or of the control. Accurate and efficient control strategies will be found by relating the vortex flow generation and the far-field evolution. Experimental configurations that would achieve this do exist, for instance the wind tunnel set-up of Brion et al. [16]. Water tunnel experiments where the spatial development of the flow can be followed over tens of wingspans could also be considered. From theoretical and numerical perspectives, it would be interesting to optimise a control on the wing itself, taking into account a sufficient distance downstream to impact the vortices once they are well formed (typically 10 wingspans). Although at present this represents a considerable challenge, it is one of the only ways to make significant progress in this field.

From a fundamental perspective, the role played by the critical layer in the nonlinear optimal vortex dynamics must be clarified. Our analysis suggests that the 2D $m = 1$ nonlinear optimal relies on the presence of a nonlinear critical layer which promotes a lasting asymmetry of the flow, as was previously described by Le Dizès [57]. The function and behaviour of critical layers in the 3D case is also in question. In particular, could 3D nonlinear optimals lead to larger growth than linear optimals, as is the case in two dimensions? Furthermore, it appears that the optimal nonlinear perturbation algorithm can be used as a tool to explore non-axisymmetric vortex states.

Nonlinear 2D optimal perturbations lead, at intermediate and large time horizons, to the activation of an $m = 1$ displacement mode, which is not particularly effective in promoting turbulence and breaking the vortex since it only displaces it. Therefore it would be worthwhile to search for nonlinear optimals that do not induce a displacement mode but perturbations with greater potential to break up the vortex. For example, a way to achieve this would be to add a penalisation term for displacement mode perturbations

in the final field or to change the objective functional.

Finally, in this thesis the vortices are considered free of axial flow. However axial flow is a constant feature of wake vortices, known to impact potentially and significantly their dynamics (vortex bursting). Concerning wake vortex cooperative instabilities, core axial flow enriches the potential interactions between Kelvin waves and the strain field imposed by the other vortex. In particular axial flow enables the interaction of vortex modes with increased radial structures. Nonlinear mechanisms could take advantage of this fact to activate quicker transition to turbulence.

It is clear that much work remains to be carried out on this challenging subject.

Acknowledgements

Je tiens d'abord à remercier chaleureusement Laurent Jacquin et Vincent Brion d'avoir accepté de diriger ma thèse et de m'avoir fait confiance. C'est en grande partie grâce à leur enthousiasme et leur soutien que ces trois années se sont aussi bien déroulées.

Merci à Claire Planchard et Dominique Grandson pour leur soutien administratif mais surtout pour leur camaraderie. Nous avons passé d'excellents moments ensemble, certes pas très productifs, mais essentiels pour le moral. Merci aussi à Olivier Marquet pour ses bons conseils.

De même je remercie vivement tout les membres du DAFE, qui sont bien trop nombreux pour tous les nommer, pour leur accueil chaleureux et leur joie de vivre. J'ai eu un grand plaisir à les connaître et à les côtoyer.

Un très grand merci à tous les doctorants et stagiaires que j'ai connus au cours de ma thèse. Je remercie particulièrement mes camarades de bureau Juan Guzman-Iñigo et Ye-Bonne Koyama de m'avoir soutenue au quotidien. Enfin, merci infiniment à la fine équipe : Nicolas Bonne, Damien Jallas et Ye-Bonne. Nous avons partagé rires, pleurs et folies... et j'espère que cela continuera.

Finally I would like to thank my family for their relentless, unconditional support and brilliant sense of humour, and Oliver for his patience and for giving me the strength to achieve my goals.

Appendices

Appendix A

Résumé en français

Les tourbillons de sillage sont formés aux extrémités des ailes d'avion en réponse à la portance. Ces tourbillons sont un enjeu majeur pour le trafic aérien en raison du danger qu'ils représentent. En effet, Spalart [92] montre que la plupart des avions n'arriveraient pas à contrer le moment de roulis s'il rencontrait le sillage d'un autre avion. Une bonne connaissance de la dynamique des ces tourbillons et des phénomènes qui l'influencent est ainsi indispensable afin de garantir la sécurité des aéronefs rendue plus délicate par le nombre croissant d'avions présents simultanément dans l'espace aérien, mais également pour réduire les séparations entre avion afin d'augmenter les capacités aéroportuaires aujourd'hui proches de la saturation. Les sillages d'avions posent aussi un problème pour le climat. En effet, les espèces chimiques éjectées des moteurs d'avion sont piégées dans les cœurs tourbillonnaires et, dans les conditions de température et d'humidité favorables, forment des cristaux de glace. Ceci conduit à la formation de nuages artificiels ou 'contrails' qui modifie le bilan radiatif terrestre. L'impact de ce phénomène sur le climat est aujourd'hui très mal quantifié mais les prédictions les plus pessimistes laissent supposer qu'il est important.

Pour tous ces problèmes, il apparaît qu'une solution serait de réduire la durée de vie des tourbillons de sillage. Pour cela le présent projet se propose de déterminer la perturbation optimale de l'écoulement, c'est-à-dire la perturbation qui détruirait les tourbillons de la manière la plus efficace, en incluant les effets non-linéaires. Bien que l'objectif final n'ait pas été atteint, un progrès important dans cette direction a été accomplit. D'abord la réponse non-linéaire de l'écoulement à la perturbation optimale linéaire déterminée par Brion et al. [15] est analysée (§ A.3.1). Ensuite le code d'optimisation non-linéaire basé sur la méthode Lagrangienne développé au cours de la thèse est appliqué à un écoulement simple : un tourbillon isolé bidimensionnel (2D) (§ A.3.2). L'effet du profil de vorticité du tourbillon sur les caractéristiques des perturbations optimales est étudié (§ A.3.3). Enfin les perturbations optimales tridimensionnelles (3D) d'un tourbillon isolé sont décrits (§ A.3.4).

D'abord une revue des travaux existants concernant les perturbations optimales de tourbillons et les méthodes numériques utilisées au cours de l'étude sont décrites.

A.1 Bilan des travaux existants

Le principe de la 'perturbation optimale' est décrite pour la première fois par Farrell [36] lors de son étude de l'écoulement de Poiseuille. Il la définit comme la perturbation qui, au cours d'un temps donné T appelé temps horizon, induit la plus grande amplification de l'énergie cinétique des perturbations. Lorsqu'un écoulement est instable, la perturbation optimale correspond à l'adjoint du mode le plus instable. Soit $\mathcal{A}$ un opérateur, son adjoint $\mathcal{A}^+$ est défini de la façon suivante : $(\mathcal{A}u, v) = (u, \mathcal{A}^+v)$, avec u et v deux vecteurs quelconques.

Concernant le tourbillon isolé, Antkowiak & Brancher [2, 3] et Pradeep & Hussain [80] ont décrit les perturbations optimales linéaires pour des nombres d'ondes azimuthaux m allant de 0 à 4. Ces perturbations optimales exploitent des mécanismes d'amplification 2D et 3D pour atteindre un gain d'énergie de perturbation maximal. En 2D, il existe deux mécanismes d'amplification. Le premier repose sur l'équation de l'énergie cinétique :

$$\frac{dE}{dt} = P - D \qquad \text{with} \quad P = -\int_V uvr\frac{\partial}{\partial r}\left(\frac{V}{r}\right) dV \tag{A.1}$$

Comme le cisaillement $S = r\frac{\partial}{\partial r}\left(\frac{V}{r}\right)$ est négatif pour un tourbillon tournant dans le sens positif, il faut que la contrainte de Reynolds uv soit positive pour que l'énergie cinétique de perturbation augmente. Ainsi les perturbations optimales s'organisent en spirales de manière à avoir $uv > 0$. Cette croissance est stoppée naturellement par l'advection différentielle de la perturbation par le champ de base qui transforme les spirales 'positives' en spirales 'négatives'. L'autre mécanisme d'amplification 2D est un phénomène de résonance observé entre des perturbations en dehors du coeur tourbillonnaire et un mode de coeur. Lorsque la fréquence de rotation de la perturbation coïncide avec la fréquence d'un des modes de coeur les moins stables, ce mode peut être excité par résonance et ainsi contribuer à la croissance d'énergie cinétique de perturbation.

Brion et al. [15] détermine la perturbation optimale linéaire d'une paire de tourbillons contrarotatifs. Cet écoulement est sujet à des instabilités cooperatives de grande et petite longueur d'onde. Dans le contexte des tourbillons de sillage, l'instabilité de grande longueur d'onde, décrite par Crow [21], domine. La perturbation optimale linéaire de Brion et al. est donc l'adjoint du mode de Crow.

Jusqu'à présent très peu de travail a été effectué sur la perturbation optimale non-linéaire de tourbillons (seule la thèse de Bisanti [13] traite ce sujet à notre connaissance). Pourtant des études d'optimisation non-linéaire portées sur d'autres écoulements [81, 19, 35] révèlent des résultats très intéressants. Non seulement les perturbations optimales non-linéaires peuvent induire des croissances de perturbations plus fortes, mais elles sont plus concentrées dans l'espace ce qui amène à croire qu'elles sont physiquement plus pertinentes que leurs homologues linéaires.

A.2 Méthodes numériques

Les équations de Navier-Stokes sont résolues par Simulation Numérique Directe (DNS) avec le solveur incompressible open-source Nek5000 [38]. Le code Nek5000 est basé sur la méthode des éléments spectraux introduite par Patera [78]. Les équations de Navier-Stokes sont résolues en mode perturbation:

$$\nabla \cdot \boldsymbol{u} = 0 \tag{A.2}$$

$$\partial_t \boldsymbol{u} + (\boldsymbol{U}\cdot\nabla)\,\boldsymbol{u} + (\boldsymbol{u}\cdot\nabla)\,\boldsymbol{U} + (\boldsymbol{u}\cdot\nabla)\,\boldsymbol{u} = -\nabla p + \frac{1}{Re}\nabla^2\boldsymbol{u} \tag{A.3}$$

avec $\boldsymbol{U}$ la vitesse du champ de base et $\boldsymbol{u}$ la vitesse de perturbation. Dans toutes les simulations, le champ de base est figé. Cette hypothèse se justifie en comparant les temps caractéristiques de l'écoulement et de la diffusion visqueuse. Par exemple, pour la paire de tourbillons, le temps caractéristique de la dynamique est $\tau = 2\pi b^2/\Gamma$ avec b la distance séparant les deux coeurs et Γ la circulation. Le temps caractéristique de diffusion visqueuse est $t_\nu = 2\pi a^2/\nu$ avec a le rayon d'un tourbillon et ν la viscosité cinématique. Ainsi $t_\nu/\tau = (a/b)^2 Re >> 1$ donc l'hypothèse est valide. Un raisonnement analogue peut être fait pour le cas du tourbillon seul.

A.2.1 Simulations sur la paire de tourbillons

Dans le cas de la paire de tourbillons, le champ de base est composé de deux tourbillons de Lamb-Oseen contrarotatifs de rayon a, de circulation $|\Gamma| = 2\pi$ et séparés d'une distance b et de longueur $7b$ égale à une longueur d'onde de l'instabilité de Crow [21]. Le rapport d'aspect est $a/b = 0.18$. Le maillage est pris suffisamment grand pour éviter les effets de bord. Les conditions aux limites sont périodiques dans la direction de l'axe des tourbillons et symétriques dans la direction transverse. Pour rester dans le référentiel attaché aux tourbillons, un champ de vitesse vertical uniforme égal à la vitesse de déplacement des tourbillons par induction mutuelle est imposé. Ainsi les conditions aux limites dans la direction verticale sont composés d'un flux entrant en bas et sortant en haut. Le temps est normalisé par le temps que met la paire de tourbillons à descendre d'une distance b sous l'effet de l'induction mutuelle $\tau = 2\pi b^2/\Gamma$.

A.2.2 Simulations sur le tourbillon isolé

Pour l'étude du tourbillon isolé, le maillage est circulaire de rayon $R = 15a$. Les conditions aux limites imposées au bord du domaine sont des conditions 'stress-free'. Un tourbillon de Lamb-Oseen de rayon a et de circulation $\Gamma = 2\pi$. Pour l'étude 3D, le maillage est extrudé pour former un cylindre de longueur $L_z = 2\pi/k$ avec k le nombre d'onde azimuthal étudié, avec des conditions de périodicité dans la direction axiale. Le temps est adimensionné par le temps de retournement du tourbillon $\tau = 4\pi^2 a^2/\Gamma$.

A.2.3 Outil d'optimisation non-linéaire

Un outil d'optimisation non-linéaire est développé avec Nek5000 en utilisant une méthode Lagrangienne. La fonctionnelle Lagrangienne est de la forme :

$$\mathcal{L}\left(\boldsymbol{q}, \boldsymbol{q}^{+}, \boldsymbol{u}_0, \boldsymbol{u}_0^{+}\right) = \mathcal{J}\left(\boldsymbol{q}, \boldsymbol{u}_0\right) - \left\langle \boldsymbol{q}^{+}, \mathcal{F}\left(\boldsymbol{q}, \boldsymbol{u}_0, \boldsymbol{u}_0^{+}\right)\right\rangle \tag{A.4}$$

avec $\boldsymbol{q}^T = (u, v, w, p)$ les variables du problème, $\boldsymbol{u}_0$ la condition initiale, $\boldsymbol{q}^+$ et $\boldsymbol{u}_0^+$ les multiplicateurs de Lagrange, et $\langle \cdot, \cdot \rangle$ le produit scalaire spatio-temporel. $\mathcal{J}\left(\boldsymbol{q}, \boldsymbol{u}_0\right)$ est la grandeur à optimiser ou la fonctionnelle objective. L'objectif étant de trouver la perturbation initiale engendrant la plus grande croissance de perturbation, le gain d'énergie cinétique de perturbation $G(T) = E(T)/E(0)$ est choisi comme fonctionnelle objective, avec

$$E(t) = \int_V \boldsymbol{u}^2(t) dV \tag{A.5}$$

Les contraintes du problème $\mathcal{F}\left(\boldsymbol{q}, \boldsymbol{u}_0, \boldsymbol{u}_0^{+}\right)$ sont les équations de Navier-Stokes et les conditions initiales et aux limites. Ainsi la forme complète de la fonctionnelle de Lagrange est :

$$\begin{aligned}
\mathcal{L}\left(\boldsymbol{q}, \boldsymbol{q}^{+}, \boldsymbol{u}_0, \boldsymbol{u}_0^{+}\right) &= \frac{\int_V \boldsymbol{u}(T)^2 dV}{\int_V \boldsymbol{u}_0^2 dV} && \text{(A.6)} \\
&- \int_0^T \int_V \boldsymbol{u}^{+} \cdot \left(\frac{\partial \boldsymbol{u}}{\partial t} + (\boldsymbol{U} \cdot \nabla)\, \boldsymbol{u} + (\boldsymbol{u} \cdot \nabla)\, \boldsymbol{U} + (\boldsymbol{u} \cdot \nabla)\, \boldsymbol{u} + \nabla p - \frac{1}{Re} \Delta \boldsymbol{u} \right) dV dt && \text{(A.7)} \\
&- \int_0^T \int_V p^{+} \nabla \cdot \boldsymbol{u} dV dt - \int_V \boldsymbol{u}_0^{+} \cdot \left(\boldsymbol{u}(0) - \boldsymbol{u}_0\right) dV && \text{(A.8)}
\end{aligned}$$

Les équations de Navier-Stokes adjointes sont obtenues en dérivant la fonctionnelle Lagrangienne par

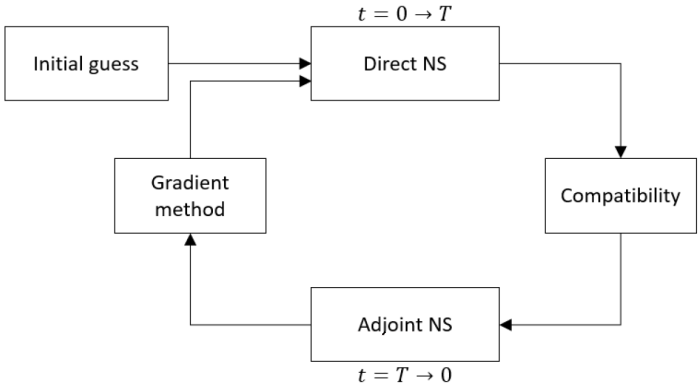

Figure A.1: Schéma de la résolution itérative du problème d'optimisation.

rapport aux variables du problème. On obtient :

$$\nabla \cdot \boldsymbol{u}^+ = 0 \tag{A.9}$$

$$\partial_t \boldsymbol{u}^+ - (\boldsymbol{U} \cdot \nabla)\boldsymbol{u}^+ - (\boldsymbol{u} \cdot \nabla)\boldsymbol{u}^+ = -\boldsymbol{u}^+ \cdot (\nabla \boldsymbol{U})^T + \boldsymbol{u} \cdot (\nabla \boldsymbol{u}^+)^T + \nabla p^+ + \frac{1}{Re}\Delta \boldsymbol{u}^+ \tag{A.10}$$

On remarque que le champ de vitesse direct $\boldsymbol{u}$ intervient dans l'équation de quantité de mouvement adjointe. Il faut donc sauvegarder le champ direct à chaque pas de temps ce qui requiert une grande capacité de stockage par rapport au cas linéaire. La dérivée de la fonctionnelle Lagrangienne par rapport à la condition initiale donne le gradient, c'est-à-dire la direction dans laquelle il faut avancer pour atteindre le gain optimal. On a :

$$\partial_{\boldsymbol{u}_0} \mathcal{L} = -2\frac{E_T}{E_0^2}\boldsymbol{u}\,(0) + \boldsymbol{u}^+\,(0) \tag{A.11}$$

L'optimisation se fait par une approche itérative :

(a) Estimation initiale du champ $\boldsymbol{u}_0$

(b) Intégration des équations directes de $t = 0$ à $t = T$

(c) Calcul du champ final adjoint $\boldsymbol{u}^+(T)$ à partir du champ final direct $\boldsymbol{u}(T)$

(d) Intégration des équations adjointes en remontant le temps de $t = T$ à $t = 0$

(e) Mise à jour du champ initial par le gradient

La procédure complète est schématisée dans la figure A.1.

Dans le cadre d'une optimisation non-linéaire, un facteur important est l'énergie initiale de perturbation. Ainsi pour l'étape de mise à jour des conditions initiales, une méthode géométrique [26] est utilisée pour implémenter la contrainte d'énergie initiale. Seule la composante du gradient orthogonale à la direction précédente et renormalisée par la contrainte E_0, $\boldsymbol{N}^j$, est retenue. La nouvelle condition initiale est obtenue par la formule suivante

$$\boldsymbol{u}\,(0)^{j+1} = \boldsymbol{u}\,(0)^j\, cos\,(\alpha) + \boldsymbol{N}^j sin\,(\alpha) \tag{A.12}$$

avec α la longueur de pas optimale trouvée par une procédure de 'line search'. Le principe est illustré pour un problème 2D dans la figure A.2.

La procédure d'optimisation linéaire est obtenue de la même manière en considérant négligeable le terme d'advection non-linéaire $(\boldsymbol{u} \cdot \nabla)\,\boldsymbol{u}$ dans le bilan de quantité de mouvement. Les équations de

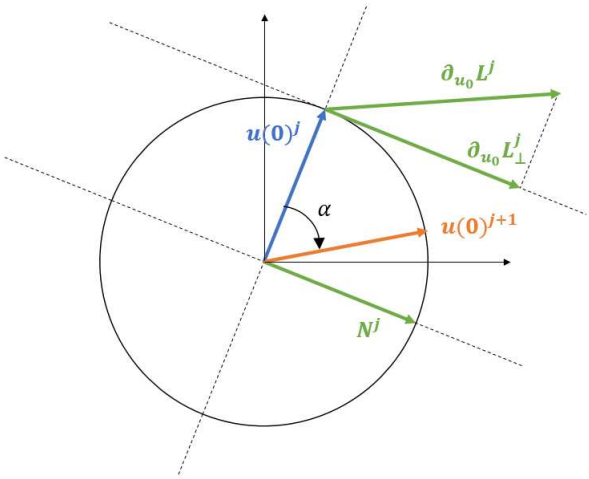

Figure A.2: Illustration de la mise à jour du champ initial par la méthode de rotation pour un problème 2D.

Navier-Stokes adjointes obtenues sont plus simples puisque le champ direct n'y intervient plus. Il n'est donc plus nécessaire de stocker ces données au cours des simulations.

Un deuxième outil d'optimisation non-linéaire, cette fois-ci fait avec un code Éléments Finis, a été développé pour la validation des résultats.

A.3 Principaux résultats de la thèse

Dans les paragraphes suivants sont résumés les résultats les plus importants de la thèse.

A.3.1 Réponse non-linéaire d'une paire de tourbillons à la perturbation optimale linéaire

L'objectif est d'évaluer le potentiel de la perturbation optimale linéaire de la paire de tourbillons [15] pour accélérer la destruction du sillage. La perturbation initiale, dont le champ de vorticité est donné en figure A.3, est superposée au champ de base avec une amplitude initiale ϵ variable $\boldsymbol{u}_{tot} = \boldsymbol{U} + \epsilon \boldsymbol{u}$. Lorsque $\epsilon << 1$, on retrouve un comportement initialement linéaire, classique d'une paire de tourbillons en atmosphère calme. L'instabilité de Crow se développe et induit une déformation sinusoïdale des tourbillons. Quand les parties des tourbillons les plus rapprochées se touchent, le phénomène de reconnection a lieu qui produit des anneaux tourbillonnaires elliptiques. Par la suite, ces anneaux subissent de nombreuses déformations typiques des anneaux elliptiques [6, 25] (voir figure A.4).

Par contre, pour $\epsilon = 0.03$, un autre comportement est observé. La déformation sinusoïdale des tourbillons se fait de manière bien plus accélérée : la reconnection a lieu à $t = 3$ au lieu de $t = 10$ pour le cas $\epsilon = 0.001$. On montre que la perturbation optimale non-linéaire accélère le développement de l'instabilité de Crow et apporte une contribution supplémentaire à la déformation sous forme de structures de vorticité secondaires qui amplifient la distorsion par induction. Une fois l'anneau tourbillonnaire formé, les structures secondaires continuent de s'enrouler autour des tourbillons primaires et génèrent des structures de plus en plus petites. Les tourbillons primaires se décomposent entièrement à $t = 12$ alors que dans le cas $\epsilon = 0.001$ les anneaux sont encore puissants à $t = 26$.

La perturbation optimale linéaire appliquée à une paire de tourbillons peut contribuer de manière significative à la destruction des structures. Lorsqu'elle est initialisée avec une amplitude finie, son action

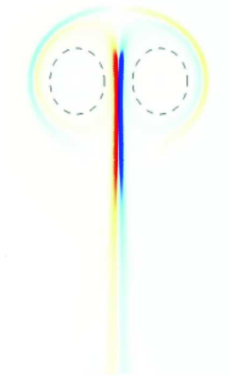

Figure A.3: Contours de vorticité axiale de la perturbation optimale linéaire de l'instabilité de Crow. Les coeurs tourbillonnaires sont indiqués en pointillés.

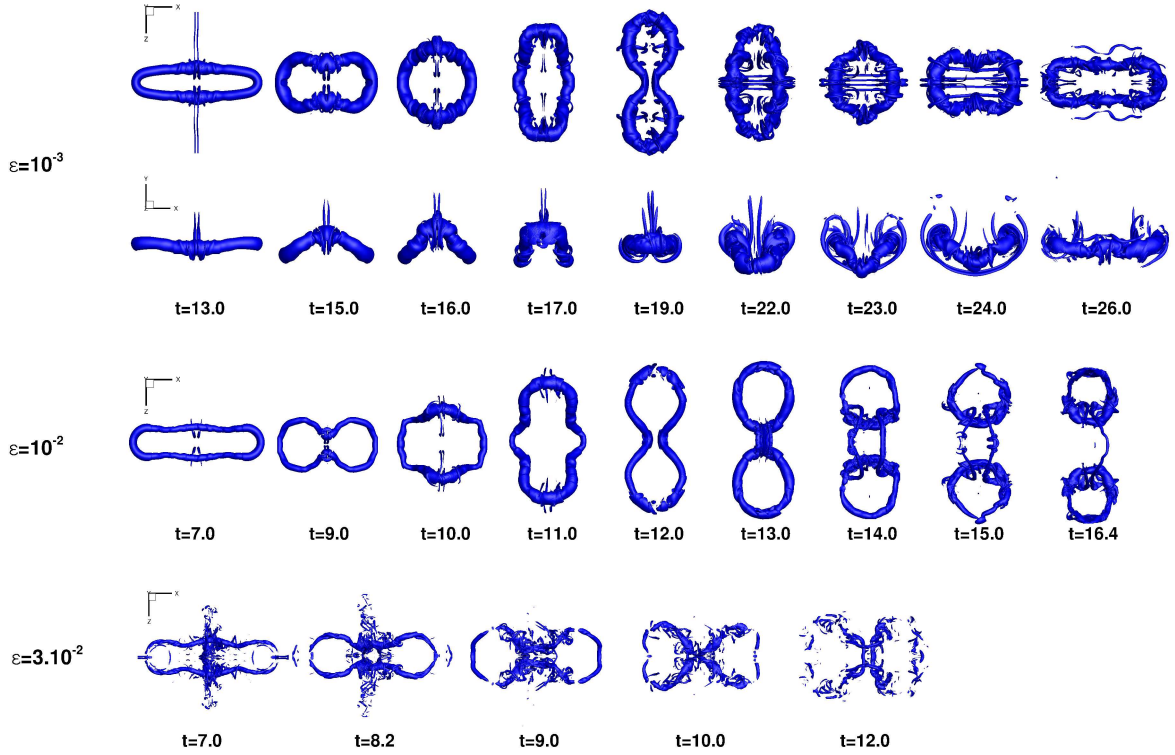

Figure A.4: Isocontours de vorticité à 14% de la norme de vorticité initiale maximale $\omega = 0.14|\omega_{max}(t = 0)|$ pour $\epsilon = 10^{-3}$ et 20% de la norme de vorticité initiale maximale $\omega = 0.14|\omega_{max}(t = 0)|$ pour $\epsilon = 10^{-2}$ et $\epsilon = 3.10^{-2}$. Evolution des anneaux tourbillonnaires durant une première période T. Vue de haut et de côté pour le cas $\epsilon = 10^{-3}$, de haut seulement pour $\epsilon = 10^{-2}$ et $\epsilon = 3.10^{-2}$.

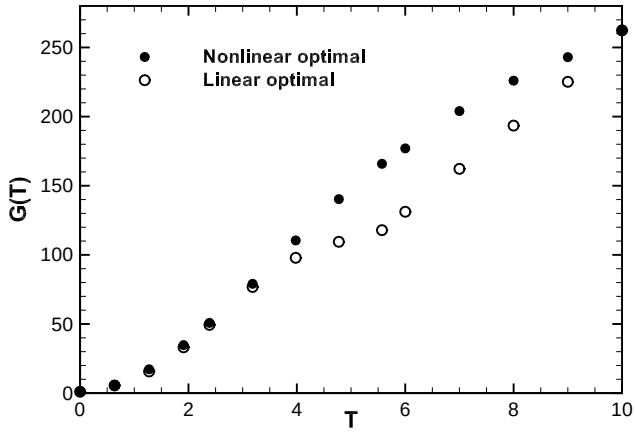

Figure A.5: Gain optimaux linéaires et non-linéaires avec $E_0 = 10^{-2}$ pour différents temps horizons T pour un tourbillon de Lamb-Oseen avec $Re = 5000$.

divise la durée de vie des structures par deux.

A.3.2 Perturbation optimale non-linéaire d'un tourbillon isolé 2D

Nous appliquons l'outil d'optimisation non-linéaire à un tourbillon isolé 2D avec une énergie initiale E_0 variable. Il s'avère que pour certains temps horizons T et énergies E_0 la perturbation optimale non-linéaire génère un gain supérieur à la perturbation optimale linéaire correspondante. Ces résultats sont reportés, pour une énergie initiale de $E_0 = 10^{-2}$, sur la figure A.5. Pour des temps horizon faibles, les perturbations linéaires restent dominantes en terme de gain. Pour $T \in [3; 9.5]$ le gain non-linéaire est bien plus élevé que le gain linéaire, avec une différence maximale de 40.6% atteinte à $T = 5.6$. A $T = 10$ le gain linéaire est au même niveau que le gain non-linéaire ce qui suggère que les mécanismes d'amplification linéaire reprennent le dessus à temps longs.

L'amplification supplémentaire par la perturbation optimale non-linéaire provient d'une excitation accélérée d'un mode de nombre d'onde azimuthal $m = 1$. Le mode $m = 1$ ne devient dominant dans le domaine linéaire qu'à partir de $T \approx 6$. En observant les champs résultants de la perturbation optimale non-linéaire, il est clair qu'un mode $m = 1$ fort apparait dès $T \approx 3$, ce qui correspond au temps horizon pour lequel le gain non-linéaire devient plus fort que le linéaire.

L'exemple de la figure A.6 illustre bien ce phénomène. Nous considérons dans ce cas la perturbation optimale non-linéaire pour un temps horizon $T = 4.8$ et $E_0 = 10^{-2}$. La perturbation initiale (figure A.6(b)) est composée de spirales de vorticité orientées de manière à ce que la contrainte de Reynolds soit positive. En revanche, contrairement à la perturbation optimale linéaire correspondante qui présente une symétrie $m = 2$, il y a deux spirales positives et une seule spirale négative. Sous l'effet de l'advection différentielle par le champ de base, les spirales se déroulent pour générer à $t = T$ un mode $m = 1$ dans le coeur et un satellite négatif en périphérie du tourbillon. La figure A.7 montre l'effet de la perturbation sur le tourbillon : celui-ci est déplacé autour de sa position de repos par le satellite négatif qui est formé à sa périphérie. Par la suite, la perturbation est maintenue dans un état quasi-stationnaire hautement énergétique (voir figure A.6(a)), résistant ainsi au phénomène naturel d'axisymétrisation [12]. Il est probable qu'une couche critique non-linéaire joue un rôle dans l'entretien de ce état non axisymétrique, comme le décrit Le Dizès [57].

En résumé, l'effet de la perturbation optimale non-linéaire consiste à accélérer l'intervention du mode $m = 1$, dominant en linéaire à temps longs, probablement grâce à une dynamique de couche critique non-

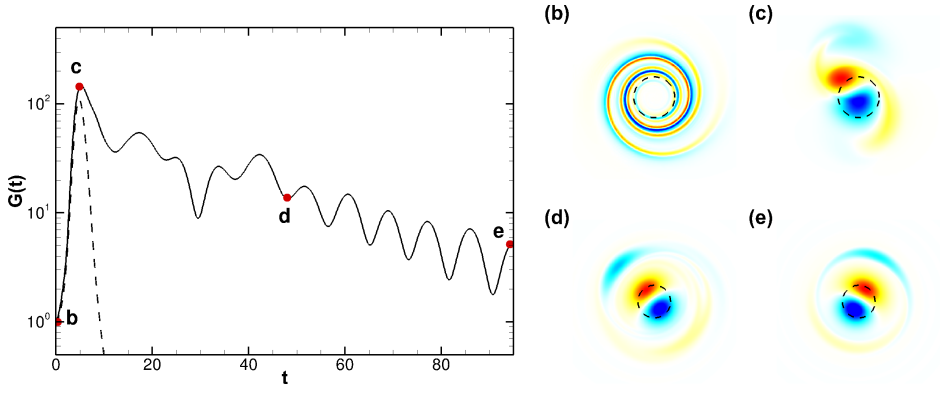

Figure A.6: (a) Gain d'énergie de perturbation pour la perturbation optimale non-linéaire (trait continu) d'un tourbillon de Lamb-Oseen avec $E_0 = 10^{-2}$ comparé à celui de la perturbation optimale linéaire (trait pointillé); contours de vorticité ω à (b) $t = 0$, (c) $t = T$, (d) $t = 10T$ et (e) $t = 20T$. Le coeur tourbillonnaire est indiqué en pointillés.

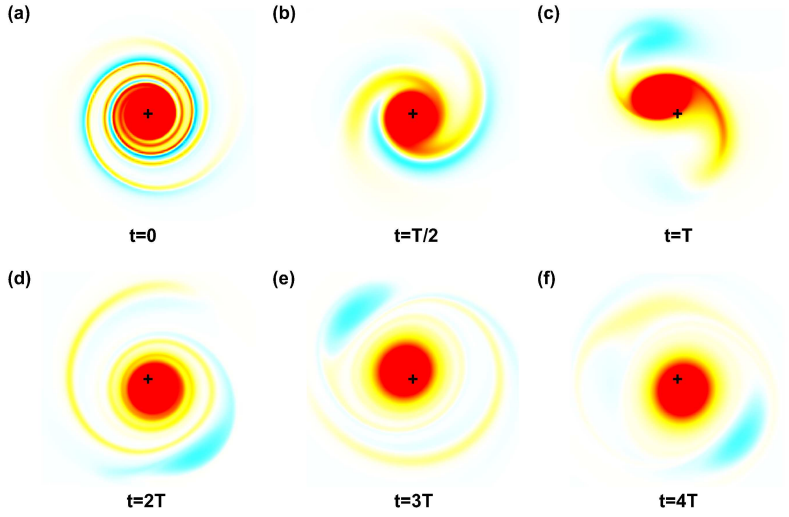

Figure A.7: Contours de vorticité illustrant l'évolution du champ complet : tourbillon et perturbation optimale non-linéaire avec $E_0 = 10^{-2}$ pour $T = 4.8$. La position du centre du tourbillon au repos est indiquée par une croix.

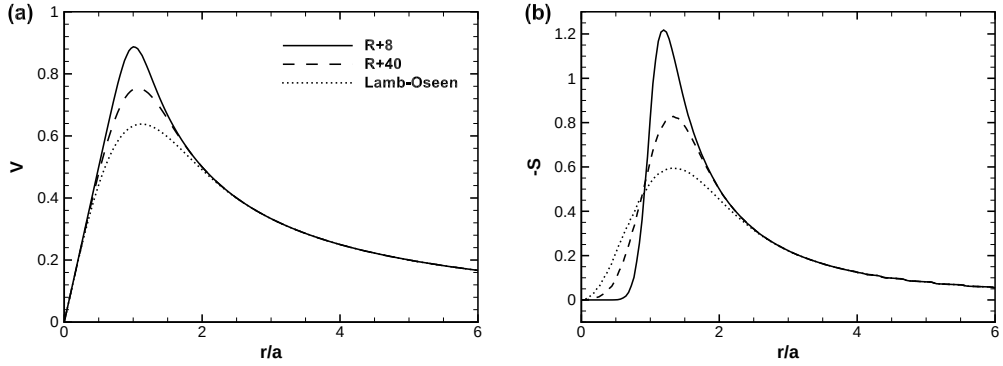

Figure A.8: (a) Profil de vitesse azimuthale de trois tourbillons : un tourbillon de Rankine ayant diffusé pendant 8 temps de rotation et 40 temps de rotation, et un tourbillon de Lamb-Oseen ; (b) Cisaillement pour les trois tourbillons.

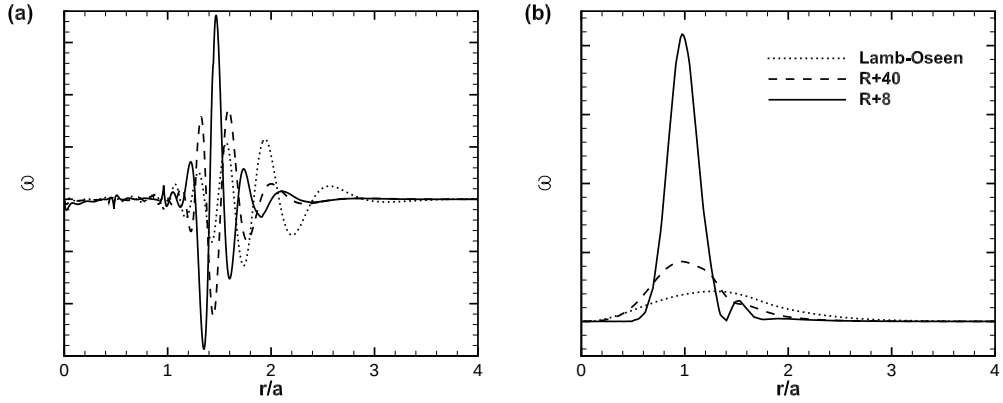

Figure A.9: Distribution radiale de vorticité ω de la perturbation optimale linéaire (a) et du champ résultant à $t = T = 4.8$ (b) pour les trois tourbillons à $Re = 5000$. L'échelle pour ω est identique pour les trois cas.

linéaire. Le tourbillon est déplacé autour de sa position initiale de manière quasi-permanente, générant ainsi un gain d'énergie cinétique de perturbation élevé.

A.3.3 Etude de l'influence du profil de vorticité sur la perturbation optimale

Le mécanisme d'amplification linéaire dépend directement de l'équilibre entre la rotation solide et le cisaillement dans le coeur tourbillonnaire [80]. Ainsi, en modifiant cet équilibre les résultats de perturbations optimales doivent aussi être impactés. Nous étudions trois tourbillons de profils de vitesse azimuthale de plus en plus raide : un tourbillon de Lamb-Oseen et deux profils obtenus en laissant diffuser un tourbillon de Rankine pendant des durées déterminées. Les trois profils retenus sont donnés en figure A.8(a) avec le niveau de cisaillemnt radial correspondant en (b).

Que ce soit pour les perturbations optimales linéaires ou non-linéaires, on remarque que plus le profil de vitesse est raide, plus les perturbations se concentrent sur un espace radial confiné. La distribution radiale de vorticité de perturbation est donnée pour la perturbation optimale linéaire ($t = 0$) et le champ résultant à $t = T$ en figure A.9.

Enfin alors que pour un tourbillon de Lamb-Oseen, le gain induit par la perturbation optimale non-linéaire peut être plus grand que celui de la perturbation optimale linéaire, ce n'est pas le cas pour des

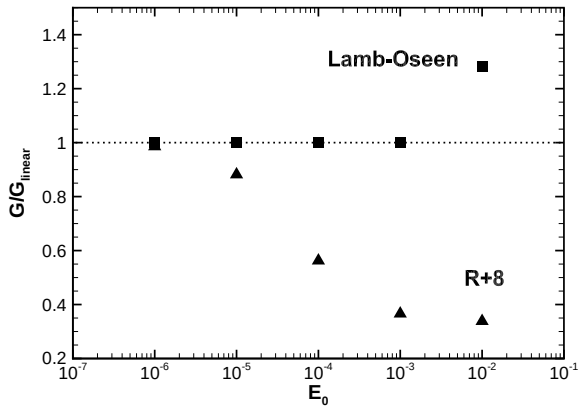

Figure A.10: Gain optimal non-linéaire comparé au gain linéaire pour le tourbillon de Lamb-Oseen et le tourbillon $R+8$ à $T = 4.8$ et $Re = 5000$ pour différentes énergies initiales E_0.

tourbillons de profil plus raide, comme le montre la figure A.10.

Pour des tourbillons ayant un profil de vitesse plus raide, l'étendue relativement plus grande du coeur en rotation solide par rapport à la zone de décroissance potentielle empêche les perturbation de pénétrer dans le coeur. De plus, l'étendue diminuée du cisaillement force les perturbation à se concentrer sur une région plus fine. Enfin, les gains atteints par les perturbations non-linéaires sont bien inférieurs aux gains linéaires.

A.3.4 Perturbation optimale non-linéaire d'un tourbillon 3D

L'étude des perturbations optimales non-linéaires pour un tourbillon isolé est étendu au domaine 3D. A cause de limitations en temps pour cette étude, seuls trois cas sont étudiés : $T = 2$, $T = 4.8$, et $T = 7$ pour $ka = 1.35$ et $Re = 5000$. Le nombre d'onde $ka = 1.35$ est choisi dans l'espoir d'exploiter le phénomène de résonance décrit par Antkowiak & Brancher [2] et Pradeep & Hussain [80] dans le domaine linéaire.

Le gain optimal non-linéaire est inférieur au gain linéaire pour tous les cas (voir figure A.11). Par contre tous les cas mènent à des états énergétiques quasi-permanents.

Les perturbations optimales linéaires et non-linéaires présentent des spirales de vorticité, et pour le cas $t = 4.8$ illustré dans la figure A.12 génèrent des modes $m = 2$ dans le coeur tourbillonnaire. De légères différences sont observables entre les cas linéaire et non-linéaire, mais on n'observe pas de grandes disparités comme pour le cas 2D.

Il est supposé que les véritables perturbations optimales non-linéaires ne sont pas encore atteints dans cette étude, vu le bruitage des contours et les évolutions peu lisses du gain non-linéaire (voir figure A.11). De plus, il est possible que le maillage ne soit pas suffisamment fin pour le nombre de Reynolds utilisé. Ces résultats préliminaires sont prometteurs mais il reste des avancées importantes à faire dans cette étude de perturbations optimales 3D.

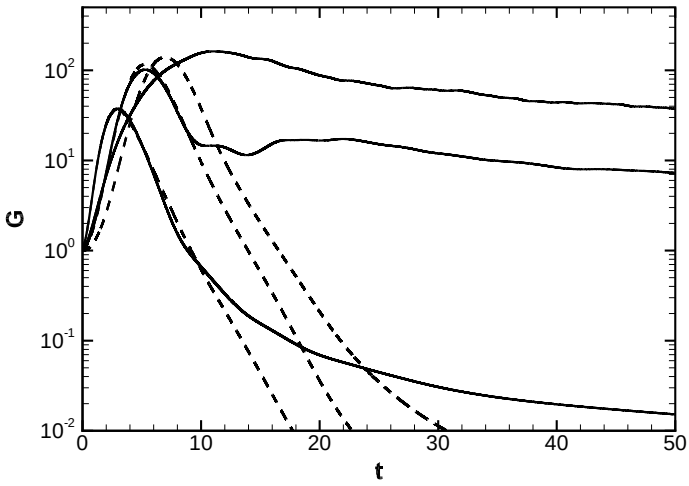

Figure A.11: Evolution du gain d'énergie cinétique de perturbation généré par les perturbations optimales 3D linéaires (trait pointillé) et non-linéaires avec $E_0 = 10^{-2}$(trait continu) pour $T = 2$, $T = 4.8$ et $T = 7$. $ka = 1.35$ et $Re = 5000$.

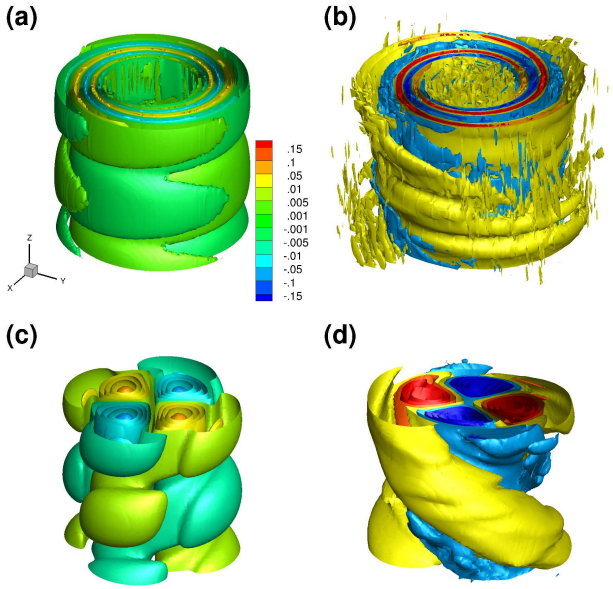

Figure A.12: Contours de vorticité axiale des perturbations optimales linéaires $(a) - (c)$ et non-linéaires $(b) - (d)$ à $t = 0$ $(a) - (b)$ et $t = T$ $((c) - (d)$ avec $T = 4.8$, $ka = 1.35$ et $Re = 5000$. Les mêmes niveaux sont utilisés pour tous les contours.

A.4 Conclusions et perspectives

Les travaux présentés dans cette thèse apportent une contribution à la problématique de contrôle des tourbillons de sillage. En conditions atmosphériques calmes, le sillage d'avion perdure bien plus longtemps que ce qui était supposé, sous la forme d'anneaux tourbillonnaires elliptiques. Néanmoins, l'application de la perturbation optimale linéaire à ces tourbillons avec une amplitude relativement faible, permet de réduire de moitié la durée de vie des tourbillons.

La perturbation optimale non-linéaire d'un tourbillon isolé 2D peut produire un gain d'énergie bien plus important que la perturbation optimale linéaire. Le mécanisme non-linéaire accélère le développement de modes $m = 1$ pour créer un déplacement du tourbillon autour de sa position d'équilibre. L'écoulement résultant est hautement énergétique et quasi-permanent, résistant ainsi le processus de symétrisation.

La forme et l'efficacité des perturbations optimales dépendent fortement de la structure interne du tourbillon. Pour des profils de vitesse azimuthale plus raide, la perturbation optimale non-linéaire est moins efficace que la perturbation optimale linéaire.

Enfin, les résultats préliminaires de l'optimisation non-linéaire 3D indiquent que le gain non-linéaire est moins important que le linéaire. Ce résultat est à confirmer par des études plus poussées. Néanmoins, des états quasi-permanents énergétiques sont atteints à temps longs par la perturbation optimale non-linéaire, comme pour le cas 2D.

La première perspective de cette thèse est de poursuivre et d'approfondir l'étude de perturbation optimale d'un tourbillon isolé 3D. La présente analyse se limite à une seule une longueur d'onde axiale et trois temps horizons. Ensuite, l'idéal serait d'appliquer l'outil d'optimisation non-linéaire à une paire de tourbillons contrarotatifs et comparer l'effet de ces perturbations optimales non-linéaires avec celui de la perturbation optimale linéaire.

Il serait intéressant de prendre en compte d'autres aspects du problème comme la stratification qui peut avoir une grande influence sur la durée de vie des sillages [77]. La prise en compte de l'effet de sol serait aussi intéressant dans le contexte aéroportuaire, notamment puisque la présence du sol permettrait l'application d'une stratégie de contrôle. De plus, les modèles de tourbillons utilisés sont 2D alors que les tourbillons de sillage présentent un écoulement axial. Les mécanismes non-linéaires pourraient exploiter cet écoulement axial pour déstabiliser plus efficacement les tourbillons. Enfin, dans le contexte des contrails, il pourrait être intéressant d'optimiser non pas la croissance de perturbations mais une quantité pertinente pour la réduction de leur durée de vie.

L'écoulement de sillage étudié dans cette thèse correspond à champ lointain, à plus d'une dizaine d'envergures derrière l'avion, lorsque l'enroulement de la nappe de vorticité laissée par l'avion dans son sillage est terminé. Pour envisager la mise en pratique des résultats des optimisations dans une stratégie de contrôle, il serait certainement plus intéressant de prendre en compte l'aile génératrice du sillage dans les simulations. Des calculs de ce type représentent un défi pour les capacités numériques actuelles, mais sont la clé pour la définition d'un système de contrôle des tourbillons intégré à l'aéronef.

Enfin d'un point de vue fondamental, il paraît important d'élucider le rôle de la couche critique non-linéaire dans la dynamique des perturbations optimales non-linéaires.

References

[1] Antkowiak, A. *Short term dynamics of an isolated vortex.* PhD thesis, Université Paul Sabatier, Toulouse, France, 2005.

[2] Antkowiak, A., and Brancher, P. Transient energy growth for the lamb–oseen vortex. *Physics of Fluids (1994-present) 16*, 1 (2004), L1–L4.

[3] Antkowiak, A., and Brancher, P. On vortex rings around vortices: an optimal mechanism. *Journal of Fluid Mechanics 578* (2007), 295–304.

[4] Appleman, H. The formation of exhaust condensation trails by jet aircraft. *Bull. Amer. Meteor. Soc 34*, 1 (1953), 14–20.

[5] Arendt, S., Fritts, D. C., and Andreassen, Ø. The initial value problem for kelvin vortex waves. *Journal of Fluid Mechanics 344* (1997), 181–212.

[6] Arms, R. J., and Hama, F. R. Localized-induction concept on a curved vortex and motion of an elliptic vortex ring. *Physics of Fluids (1958-1988) 8*, 4 (1965), 553–559.

[7] Baker, G. R., Barker, S. J., Bofah, K. K., and Saffman, P. G. Laser anemometer measurements of trailing vortices in water. *Journal of Fluid Mechanics 65*, 02 (1974), 325–336.

[8] Balmforth, N. J., Llewellyn Smith, S. G., and Young, W. R. Disturbing vortices. *Journal of Fluid Mechanics 426* (2001), 95–133.

[9] Bassom, A. P., and Gilbert, A. D. The spiral wind-up of vorticity in an inviscid planar vortex. *Journal of Fluid Mechanics 371* (1998), 109–140.

[10] Batchelor, G. Axial flow in trailing line vortices. *Journal of Fluid Mechanics 20*, 04 (1964), 645–658.

[11] Beninati, M. L., and Marshall, J. S. An experimental study of the effect of free-stream turbulence on a trailing vortex. *Experiments in Fluids 38*, 2 (2005), 244–257.

[12] Bernoff, A. J., and Lingevitch, J. F. Rapid relaxation of an axisymmetric vortex. *Physics of Fluids (1994-present) 6*, 11 (1994), 3717–3723.

[13] Bisanti, L. *Linear and nonlinear optimal perturbation analysis of vortices in incompressible flow.* PhD thesis, Universite de Toulouse, France, 2013.

[14] Brion, V. *Stabilité des paires de tourbillons contra-rotatifs: application au tourbillon de jeu dans les turbomachines.* PhD thesis, Ecole Polytechnique, France, 2009.

[15] Brion, V., Sipp, D., and Jacquin, L. Optimal amplification of the crow instability. *Physics of Fluids (1994-present) 19*, 11 (2007), 111703.

[16] Brion, V., Sipp, D., and Jacquin, L. Linear dynamics of the lamb-chaplygin dipole in the two-dimensional limit. *Physics of Fluids (1994-present) 26*, 6 (2014), 064103.

[17] Butler, K. M., and Farrell, B. F. Three-dimensional optimal perturbations in viscous shear flow. *Physics of Fluids A: Fluid Dynamics (1989-1993) 4*, 8 (1992), 1637–1650.

[18] Caillol, P., and Maslowe, S. The small vorticity nonlinear critical layer for kelvin modes on a vortex. *Studies in Applied Mathematics 118*, 3 (2007), 221–254.

[19] Cherubini, S., and De Palma, P. Nonlinear optimal perturbations in a couette flow: bursting and transition. *Journal of Fluid Mechanics 716* (2013), 251–279.

[20] Cherubini, S., De Palma, P., Robinet, J.-C., and Bottaro, A. The minimal seed of turbulent transition in the boundary layer. *Journal of Fluid Mechanics 689* (2011), 221–253.

[21] Crow, S. C. Stability theory for a pair of trailing vortices. *AIAA journal 8*, 12 (1970), 2172–2179.

[22] Devenport, W. J., Rife, M. C., Liapis, S. I., and Follin, G. J. The structure and development of a wing-tip vortex. *Journal of Fluid Mechanics 312* (1996), 67–106.

[23] Deville, M. O., Fischer, P. F., and Mund, E. H. *High-order methods for incompressible fluid flow*, vol. 9. Cambridge University Press, 2002.

[24] Dhanak, M., and Bernardinis, B. D. The evolution of an elliptic vortex ring. *Journal of Fluid Mechanics 109* (1980).

[25] Dhanak, M. R., and Bernardinis, B. D. The evolution of an elliptic vortex ring. *Journal of Fluid Mechanics 109* (1981), 189–216.

[26] Douglas, S. C., Amari, S.-I., and Kung, S.-Y. On gradient adaptation with unit-norm constraints. *IEEE Transactions on Signal Processing 48*, 6 (2000), 1843–1847.

[27] Drazin, P. G., and Reid, W. H. Hydrodynamic stability, 1981.

[28] Dritschel, D. G. A general theory for two-dimensional vortex interactions. *Journal of Fluid Mechanics 293* (1995), 269–303.

[29] Dritschel, D. G. On the persistence of non-axisymmetric vortices in inviscid two-dimensional flows. *Journal of Fluid Mechanics 371* (1998), 141–155.

[30] Edstrand, A. M., Davis, T. B., Schmid, P. J., Taira, K., and Cattafesta, L. N. On the mechanism of trailing vortex wandering. *Journal of Fluid Mechanics 801* (2016), R1.

[31] Eloy, C., and Le Dizès, S. Three-dimensional instability of burgers and lamb–oseen vortices in a strain field. *Journal of Fluid Mechanics 378* (1999), 145–166.

[32] Fabre, D., and Jacquin, L. Short-wave cooperative instabilities in representative aircraft vortices. *Physics of fluids 16*, 5 (2004), 1366–1378.

[33] Fabre, D., Jacquin, L., and Loof, A. Optimal perturbations in a four-vortex aircraft wake in counter-rotating configuration. *Journal of Fluid Mechanics 451* (2002), 319–328.

[34] Fabre, D., Sipp, D., and Jacquin, L. Kelvin waves and the singular modes of the lamb–oseen vortex. *Journal of Fluid Mechanics 551* (2006), 235–274.

[35] Farano, M., Cherubini, S., Robinet, J.-C., and De Palma, P. Hairpin-like optimal perturbations in plane poiseuille flow. *Journal of Fluid Mechanics 775* (2015), R2.

[36] Farrell, B. F. Optimal excitation of perturbations in viscous shear flow. *Physics of Fluids 31*, 8 (1988), 2093.

[37] Farrell, B. F., and Ioannou, P. J. Optimal excitation of three-dimensional perturbations in viscous constant shear flow. *Physics of Fluids A: Fluid Dynamics (1989-1993) 5*, 6 (1993), 1390–1400.

[38] Fischer, P., Lottes, J., and Kerkemeier, S. nek5000 Web page, 2008. http://nek5000.mcs.anl.gov.

[39] Fontane, J., Brancher, P., and Fabre, D. Stochastic forcing of the lamb–oseen vortex. *Journal of Fluid Mechanics 613* (2008), 233–254.

[40] Foures, D. P. G., Caulfield, C. P., and Schmid, P. J. Localization of flow structures using ∞-norm optimization. *Journal of Fluid Mechanics 729* (2013), 672–701.

[41] Gallaire, F., and Chomaz, J.-M. Three-dimensional instability of isolated vortices. *Physics of Fluids (1994-present) 15*, 8 (2003), 2113–2126.

[42] Gau, T., and Hattori, Y. Modal and non-modal stability of two-dimensional taylor–green vortices. *Fluid Dynamics Research 46*, 3 (2014), 031410.

[43] Hecht, F. New development in freefem++. *J. Numer. Math. 20*, 3-4 (2012), 251–265.

[44] Hopfinger, E. J., Browand, F. K., and Gagne, Y. Turbulence and waves in a rotating tank. *Journal of Fluid Mechanics 125* (1982), 505–534.

[45] Hussain, F., and Duraisamy, K. Mechanics of viscous vortex reconnection. *Physics of Fluids (1994-present) 23*, 2 (2011), 021701.

[46] Hussain, F., Pradeep, D. S., and Stout, E. Nonlinear transient growth in a vortex column. *Journal of Fluid Mechanics 682* (2011), 304–331.

[47] Jacquin, L., Fabre, D., Geffroy, P., and Coustols, E. The properties of a transport aircraft extended near field: an experimental study. In *AIAA conference proceedings* (2001), vol. 1038.

[48] Jacquin, L., and Pantano, C. On the persistence of trailing vortices. *Journal of Fluid Mechanics 471* (2002), 159–168.

[49] Jimenez, J. Stability of a pair of co-rotating vortices. *Physics of Fluids (1958-1988) 18*, 11 (1975), 1580–1581.

[50] Johnson, H. G., Brion, V., and Jacquin, L. Crow instability: nonlinear response to the linear optimal perturbation. *Journal of Fluid Mechanics 795* (2016), 652–670.

[51] Karniadakis, G., and Sherwin, S. *Spectral/hp element methods for computational fluid dynamics*. Oxford University Press, 2005.

[52] Kelvin, L. Vibrations of a columnar vortex. *Phil. Mag 10*, 5 (1880), 155–168.

[53] Koumoutsakos, P. Inviscid axisymmetrization of an elliptical vortex. *Journal of Computational Physics 138*, 2 (1997), 821–857.

[54] Küchemann, D. Report on the iutam symposium on concentrated vortex motions in fluids. *Journal of Fluid Mechanics 21*, 01 (1965), 1–20.

[55] Landahl, M. T. Wave breakdown and turbulence. *SIAM Journal on Applied Mathematics 28*, 4 (1975), 735–756.

[56] Laporte, F., and Corjon, A. Direct numerical simulations of the elliptic instability of a vortex pair. *Physics of Fluids (1994-present) 12*, 5 (2000), 1016–1031.

[57] Le Dizes, S. Non-axisymmetric vortices in two-dimensional flows. *Journal of Fluid Mechanics 406* (2000), 175–198.

[58] Lee, J. J., Lukachko, S. P., Waitz, I. A., Schafer, A., et al. Historical and future trends in aircraft performance, cost, and emissions. *Annual Review of Energy and the Environment 26*, 1 (2001), 167–200.

[59] Leweke, T., and Williamson, C. H. K. Cooperative elliptic instability of a vortex pair. *Journal of fluid mechanics 360* (1998), 85–119.

[60] Leweke, T., and Williamson, C. H. K. Experiments on long-wavelength instability and reconnection of a vortex pair. *Physics of Fluids (1994-present) 23*, 2 (2011), 024101.

[61] Lord, R. On the stability, or instability, of certain fluid motions. *Proc. London Math. Soc 11* (1880), 57–70.

[62] Lundgren, T. S. Strained spiral vortex model for turbulent fine structure. *Physics of Fluids (1958-1988) 25*, 12 (1982), 2193–2203.

[63] Macaskill, C., Bassom, A. P., and Gilbert, A. D. Nonlinear wind-up in a strained planar vortex. *European Journal of Mechanics-B/Fluids 21*, 3 (2002), 293–306.

[64] Mao, X., and Sherwin, S. Continuous spectra of the batchelor vortex. *Journal of Fluid Mechanics 681* (2011), 1–23.

[65] Mao, X., and Sherwin, S. J. Transient growth associated with continuous spectra of the batchelor vortex. *Journal of Fluid Mechanics 697* (2012), 35–59.

[66] Marquet, O., Sipp, D., Chomaz, J.-M., and Jacquin, L. Amplifier and resonator dynamics of a low-reynolds-number recirculation bubble in a global framework. *Journal of Fluid Mechanics 605* (2008), 429–443.

[67] Marshall, J. S., and Beninati, M. L. External turbulence interaction with a columnar vortex. *Journal of Fluid Mechanics 540* (2005), 221.

[68] Marshall, J. S., Brancher, P., and Giovannini, A. Interaction of unequal anti-parallel vortex tubes. *Journal of Fluid Mechanics 446* (2001), 229–252.

[69] Maxworthy, T., Hopfinger, E. J., and Redekopp, L. G. Wave motions on vortex cores. *Journal of Fluid Mechanics 151* (1985), 141–165.

[70] Melander, M. V., and Hussain, F. Cross-linking of two antiparallel vortex tubes. *Physics of Fluids A: Fluid Dynamics (1989-1993) 1*, 4 (1989), 633–636.

[71] Melander, M. V., and Hussain, F. Coupling between a coherent structure and fine-scale turbulence. *Physical Review E 48*, 4 (1993), 2669.

[72] Melander, M. V., McWilliams, J. C., and Zabusky, N. J. Axisymmetrization and vorticity-gradient intensification of an isolated two-dimensional vortex through filamentation. *Journal of Fluid Mechanics 178* (1987), 137–159.

[73] Misaka, T., Holzäpfel, F., Hennemann, I., Gerz, T., Manhart, M., and Schwertfirm, F. Vortex bursting and tracer transport of a counter-rotating vortex pair. *Physics of Fluids (1994-present) 24*, 2 (2012), 025104.

[74] Miyazaki, T., and Hunt, J. C. R. Linear and nonlinear interactions between a columnar vortex and external turbulence. *Journal of Fluid Mechanics 402* (2000), 349–378.

[75] Moriconi, L. Vortex reconnection as the dissipative scattering of dipoles. *Physical Review E 61*, 3 (2000), 2640.

[76] Nocedal, J., and Wright, S. *Numerical optimization*. Springer Science & Business Media, 2006.

[77] Ortiz, S., Donnadieu, C., and Chomaz, J.-M. Three-dimensional instabilities and optimal perturbations of a counter-rotating vortex pair in stratified flows. *Physics of Fluids (1994-present) 27*, 10 (2015), 106603.

[78] Patera, A. T. A spectral element method for fluid dynamics: laminar flow in a channel expansion. *Journal of computational Physics 54*, 3 (1984), 468–488.

[79] Pope, S. *Turbulent flows*. Cambridge University Press, 2000.

[80] Pradeep, D. S., and Hussain, F. Transient growth of perturbations in a vortex column. *Journal of Fluid Mechanics 550* (2006), 251–288.

[81] Pringle, C. C. T., and Kerswell, R. R. Using nonlinear transient growth to construct the minimal seed for shear flow turbulence. *Physical review letters 105*, 15 (2010), 154502.

[82] Rossi, L. F., Lingevitch, J. F., and Bernoff, A. J. Quasi-steady monopole and tripole attractors for relaxing vortices. *Physics of Fluids (1994-present) 9*, 8 (1997), 2329–2338.

[83] Rossi, M. Of vortices and vortical layers: an overview. In *Vortex Structure and dynamics*. Springer, 2000, pp. 40–123.

[84] Saffman, P. G. A model of vortex reconnection. *Journal of Fluid Mechanics 212* (1990), 395–402.

[85] Saffman, P. G. *Vortex dynamics*. Cambridge university press, 1992.

[86] Schaeffer, N., and Le Dizès, S. Nonlinear dynamics of the elliptic instability. *Journal of Fluid Mechanics 646* (2010), 471–480.

[87] Schmid, P. J., and Henningson, D. S. *Stability and Transition in Shear Flows. Number v. 142 in Applied Mathematical Sciences*. Springer-Verlag, 2001.

[88] Sipp, D. *Instabilités dans les écoulements tourbillonnaires*. PhD thesis, Ecole Polytechnique, France, 1999.

[89] Sipp, D., and Jacquin, L. Elliptic instability in two-dimensional flattened taylor–green vortices. *Physics of Fluids (1994-present) 10*, 4 (1998), 839–849.

[90] Sipp, D., and Jacquin, L. Widnall instabilities in vortex pairs. *Physics of Fluids (1994-present) 15*, 7 (2003), 1861–1874.

[91] Spalart, P., and Wray, A. Initiation of the crow instability by atmospheric turbulence. *The characterisation & modification of wakes from lifting vehicles in fluids 584* (1996).

[92] Spalart, P. R. Airplane trailing vortices. *Annual Review of Fluid Mechanics 30*, 1 (1998), 107–138.

[93] Trefethen, L., Trefethen, A., Reddy, S., Driscoll, T., et al. Hydrodynamic stability without eigenvalues. *Science 261*, 5121 (1993), 578–584.

[94] Tsai, C.-Y., and Widnall, S. E. The stability of short waves on a straight vortex filament in a weak externally imposed strain field. *Journal of Fluid Mechanics 73*, 04 (1976), 721–733.

[95] Turner, M. R., and Gilbert, A. D. Linear and nonlinear decay of cat's eyes in two-dimensional vortices, and the link to landau poles. *Journal of Fluid Mechanics 593* (2007), 255–279.

[96] Werlé, H. Flow visualisation techniques for the study of high incidence aerodynamics. *AGARD-VKI Lecture Series 121* (1982).

[97] Zuccher, S., Luchini, P., and Bottaro, A. Algebraic growth in a blasius boundary layer: optimal and robust control by mean suction in the nonlinear regime. *Journal of Fluid Mechanics 513* (2004), 135–160.